Influence of ice jams on ice-induced vibrations of multi-legged sub-structures

Master of science thesis

T. Lelieveld

November 2021

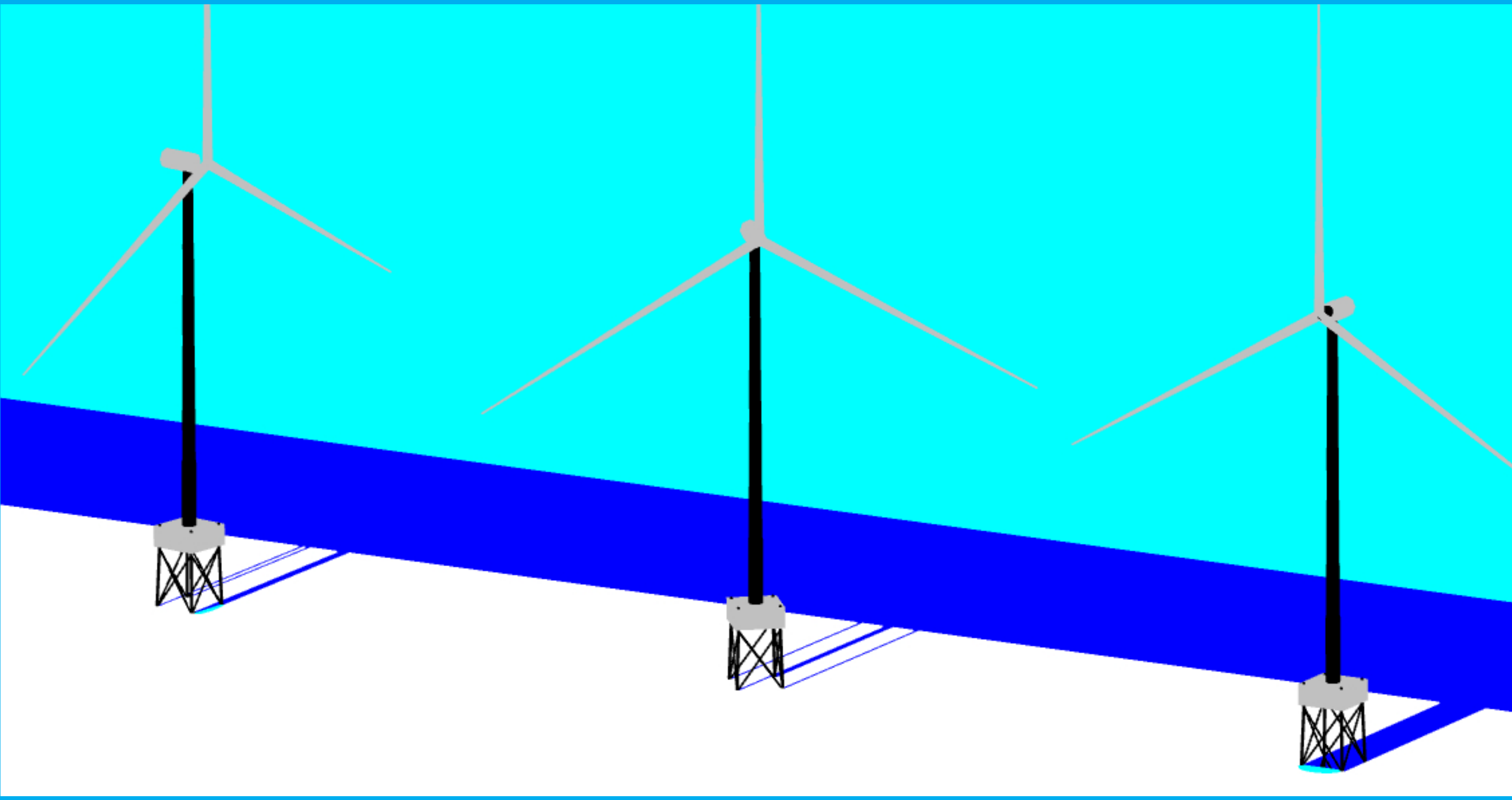

TU Delft

Influence of ice jams on ice-induced vibrations of multi-legged sub-structures

by

T. Lelieveld

A thesis submitted to the Delft University of Technology in partial fulfillment
of the requirements for the degree of

Master of Science in Offshore & Dredging Engineering for the faculty of Mechanical,
Maritime and Materials Engineering.

To be defended publicly on Friday 19 November, 2021 at 3:00-4:30 PM.

Student number:	4453093	
Project duration:	January 1, 2021 – November 19, 2021	
Thesis committee:	Dr. ir. Hayo Hendrikse,	TU Delft, chairman & supervisor
	Ir. Cody Owen,	TU Delft, daily supervisor
	Prof. dr. ir. Andrei Metrikine,	TU Delft

Preface

This report is my final deliverable for the Master of Science degree in Offshore & Dredging Engineering with specialisation in Bottom Founded Structures, Arctic and Wind at the Delft University of Technology. Graduating during COVID-19 times was a long and bumpy ride. I have learned a tremendous amount about myself, my working discipline, and in what situations I can perform best. These last ten months were the most challenging of my academic years at the TU Delft. Thus I am happy and proud to present my final report.

I would like to sincerely thank my supervisors Hayo Hendrikse and Cody Owen, who supported and guided me along the way. They always took the time to listen to me and give valuable feedback. The weekly meetings helped me during all this remote work from home. These sessions were always fun and gave me great insights into the beautiful world of ice action. Thanks for all the critical questions, helping me understand the theory and making my workflow better. At last, I want to thank Andrei Metrikine, the third committee member, for his specific questions and for providing his guidance during the meetings we had together.

I want to thank my friends for their confidence and support during these last ten months. They provided me with much-needed distraction, which provided the energy to continue the work. I want to thank my family for their unconditional support and guidance throughout this rough year.

Enjoy reading!

T. Lelieveld
Stavanger, November 2021

Abstract

The world is transforming its energy production towards more sustainable sources of energy. In Europe, there is currently 25 GW of installed offshore wind power capacity. This is expected to grow with 29 GW over the next five years. Offshore wind farms can be expensive and challenging to build, design and maintain. Understanding the offshore environment will ensure that the to be produced offshore wind turbines are of sufficient quality while reducing costs. Monopiles are currently the most common sub-structure, but jacket sub-structures are becoming more relevant due to increasing water depth or changing soil conditions. Structures in icy waters, such as the Baltic Sea, may be subjected to ice induced vibrations while they encounter sea ice. These vibrations have to be considered in vertically-sided offshore structures' design and are the most critical load case when ice is concerned.

Multi-legged sub-structures, such as jackets, can have a problem that does not exist for monopiles, namely ice jamming, where ice fills the space between the legs of a multi-legged sub-structure. The legs and the jammed ice may then act as a single structural unit. Which leads to the main research question: how does an ice jam influence ice-induced vibrations of a multi-legged sub-structure?

First, a literature study of ice jams and multi-legged sub-structures was performed. This study concluded that different ice jamming situations are possible and have occurred with multi-legged structures, which not all have survived. The ratio between leg spacing and diameter plays a vital role in the ice action on multi-legged structures. Furthermore, the combination of ice-induced vibrations and ice jamming had not been studied yet.

Secondly, a model is made based on a phenomenological ice crushing model using COMSOL Multiphysics and MATLAB to simulate the structural response. The sub-structure is based on the jacket design for the NREL 5-MW reference turbine. Different situations from the literature study are used to make several design scenarios for which the structural response is calculated. In total, there are five situations: a base case, an angled base case, an internal jam, a frontal jam and an angled frontal ice jam. The base case does not have an ice jam, and the angled frontal jam has an increased thickness of the jam to twice the incoming ice. For the other jams, the thickness is equal to the incoming ice.

The different scenarios are simulated for a range of ice drift velocities to capture the different ice-induced vibration regimes and see how the structural response changes due to the presence of an ice jam. First, a baseline was established of the jacket's structural response for the base case. Afterwards, the three different ice jams were simulated. Results show that the base case is excited in all three ice-induced vibration regimes. At lower ice drift speeds, intermittent crushing is observed. Then at around 0.05 ms^{-1}, it transitions into the frequency lock-in regime. Here the structure is excited at its second natural frequency. For higher ice drift velocities (>0.2 ms^{-1}), continuous brittle crushing is seen. For the angled base case, the transition between intermittent crushing and frequency lock-in happens at around 0.1 ms^{-1}, and it stays longer in the frequency lock-in regime. The internal stresses around the contact area between ice and leg for the internal and frontal jam did significantly exceed the ice strength. Thus these jams would have failed on crushing at the contact area. The stresses inside the angled frontal jam exceed the ice strength but by a small margin. With all the assumptions made taken into account, the jam might hold. The structural response shows an increase in period for intermittent crushing and a lower amplitude in structural displacement than the base case.

The main conclusion is that an ice jam that would significantly impact the ice-induced vibrations cannot be sustained. The internal stresses exceed the ice strength which would cause the jam to fail. The ice jam that can be sustained acts as additional stiffness for the system and decreases the structure's displacement amplitude for the intermittent crushing regime. In the frequency lock-in regime the structure's displacement frequency increases a bit. But the amplitude is similar in all scenarios because the maximum velocity of the structure will roughly be the same as the incoming ice floe because that is what excites the structure, and this doesn't change.

Contents

1

Introduction

1.1. Background

In 2015 the Parties to the United Nations Framework Convention on Climate Change met for the United Nations Climate Change Conference (COP 21) in Paris, France. The Parties presented a legally binding international treaty on climate change. Its goal is to limit global warming to below 2°Celsius and pursue efforts to keep it below 1.5°Celsius, compared to pre-industrial levels (Article 2 of the Paris Agreement). This legally binding international treaty on climate change is ratified by 191 Parties and signed by 195 Parties as of the 5th of October 2021. This shows the intent of almost every country in the world to reach a climate neutral world by 2050. The respective countries have submitted their plans for climate action known as Intended Nationally Determined Contributions (INDCs). In their INDCs, the countries communicate actions which they take to reach the goals of the Paris Agreement (UNFCCC, 2015).

An assessment made by an international team of experts and published in Nature estimates that the existing INDCs would lower greenhouse gas emissions. However, it still implies median warming of 2.6-3.1°Celsius by the year 2100. It is stated that substantial over-delivery on the current INDCs is necessary of preventing global warming from exceeding the 2°Celsius (Rogelj et al., 2016). A more recent study by researchers from PBL Netherlands Environmental Assessment Agency and Utrecht University was done to look at the current climate actions and to compare them against the objective of the Paris Agreement. This study re-iterates that the current INDCs are not sufficient to reach the goals of the Paris Agreement (Roelfsema et al., 2020). The United Nations Environmental Programme (2020) produces yearly the Emissions Gap Report, in which they calculate the gap between "where we are likely to be and where we need to be". In the 2020 report, it is stated that the gap has not been narrowed compared to 2019. Although, there is a growing number of countries that are committed to achieving net-zero emissions by 2050.

In 2019 the European Commission (EC) introduced the European Green Deal to become the world's first climate-neutral continent and be consistent with the Paris Agreement temperature goal. The deal aims to achieve net-zero greenhouse gas (GHG) emissions in 2050 (European Commission, 2019). The European Union (EU) (including the United Kingdom (UK)) had an emissions share of 9.3% (percentage of global total) during the 2010-2019 period (United Nations Environmental Programme, 2020). In 2019 the GHG emissions were down by 25% compared with 1990 levels. According to the European Green Deal, the emissions should be down 55% in 2030 compared to 1990, or a 40% reduction in 2030 compared to 2019 levels (European Environmental Agency, 2020). However, in order to achieve the most prestigious goal, keeping global warming under 1.5°Celsius, the emission reduction in 2030 from 2019 should be at least 57% (United Nations Environmental Programme, 2020). The Paris Agreement, the Intended Nationally Determined Contributions, and the European Green Deal are all examples of regulatory actions to make Earth a sustainable place by 2050 with net-zero emissions. However, as stated numerous times, the current policies are not sufficient to reach the goals of the Paris Agreement. That means either policies and/or technology has to advance and innovate to reach it. For now, let us look at the most significant contributor to GHG emissions in Europe.

The production and use of energy across economic sectors account for more than 75% of the EU's GHG emissions. Thus by focusing on energy efficiency and redeveloping the energy sector based upon renewable sources will significantly reduce the GHG emissions (European Commission, 2019). In the EU, the share of renewable energy has more than doubled between 2004 and 2019. This trend and development has been boosted by the European Green Deal and the targets the EU has set for itself. The EU wants to have a 20% and 32% share of its gross final energy consumption from renewable sources by 2020 and 2030, respectively. The contribution of renewable energy sources was 19.7% in 2019. The main drivers behind the renewable energy sources are wind and hydropower, each accounting for 35% of total renewable energy. The fastest growing renewable energy sources are wind and solar power (Eurostat, 2020). For example, the total installed capacity of wind turbines worldwide grew by roughly 10% per year during 2016-2019. Europe contributed roughly one-third of total installed capacity in 2018 and 2019 (World Wind Energy Association, 2020).

Wind energy can be segmented into onshore and offshore wind energy. In December 1980 the first onshore wind farm was installed in southern New Hampshire, U.S (U.S. Department of Energy, 2008). Since then, the development has been fast, and the majority of all the wind turbines have been built onshore. However, in 1991 the first offshore wind farm was built in Vindeby, Denmark (WindEurope, 2019b). During these years much knowledge about the efficiency, production and costs have been gained. Around 2008 the offshore wind energy got a lot more traction and momentum. The growth of onshore wind farms is being held back by the lack of inexpensive land around major populated areas and the visual pollution caused by large wind turbines, causing the focus to change towards offshore wind energy and its advantages. The wind speeds tend to be higher and more consistent (Bilgili et al., 2011). There is a vast ocean available to put large wind turbines. However, it is technologically more difficult, and capital expenditures (CAPEX) are higher (Markard and Petersen, 2009). However, technology is advancing, and the percentage of installed capacity offshore is rapidly increasing. In 2008, 2.3% of installed capacity was installed offshore in Europe (Global Wind Energy Council, 2009). In the last year, 2020, the installed capacity offshore was 11%. The average capacity factor (the ratio between the energy produced and the theoretical maximum) was 42% and 25% for offshore and onshore, respectively. Showing that offshore wind energy is more efficient than onshore (WindEurope, 2020b). The European Commission (2020) has seen this potential, and they made an elaborate EU strategy on how to harness the potential of offshore renewable energy. They endorse the leading position of the EU in the offshore wind energy market. Europe was the first continent with an offshore wind farm, and two European companies are among the top five in the preliminary rankings for the world's top five turbine original equipment manufactures Global Wind Energy Council (2021) (GWEC). The GWEC and EC both underwrite that technological advances have made the steep increase in offshore wind possible and that it is necessary to keep on developing and innovating in order to grow at the same pace (Global Wind Energy Council, 2020). Due to innovative technologies and a better understanding of the physical problems, wind turbines can be scaled up. The larger the wind turbine, the more efficient and the greener the electricity becomes (Caduff et al., 2012). The CAPEX and operating expenditures (OPEX) per MW will reduce due to the higher efficiencies, resulting in offshore wind being financially more attractive.

Offshore wind farms are mainly exploited by the northern countries in Europe. Placing wind farms further offshore enables larger sea areas with more stable wind conditions, reduces the impact on other economic activities and minimises potential visual impact on the coastline. Moreover, with increasing distance to shore, the water depths are also increasing, resulting in different types of support structures, see Figure 1.1. The Moray East (UK) wind farm has a depth of 45m and is the deepest bottom-founded project, using a jacket sub-structure. Another reason to choose a jacket sub-structure could be the soil conditions. Most of the projects in shallower waters use monopiles. While the project Windfloat Atlantic, Portugal, uses floating wind farms with a water depth of 100m (WindEurope, 2020a). Sánchez et al. (2019) looked into the different sub-structures and it concludes that monopiles are the most used sub-structure in shallow (0-15m) and intermediate depths (15-30m). While for depths larger than 30m, jacket and tripod structures are strong competitors. For water depths exceeding 50m, a floating sub-structure is mainly used. Oh et al. (2018) also reviewed the different sub-structures and had the same conclusion that in deeper waters (30-50m), the jacket and tripod are more favourable due to lower costs. Floating wind is currently in its start-up phase, and multiple demo sites have been built over the past two years. Europe's pipeline of floating projects for the next decade is promising (WindEurope, 2020a). The focus of this thesis will be upon jacket sub-structures.

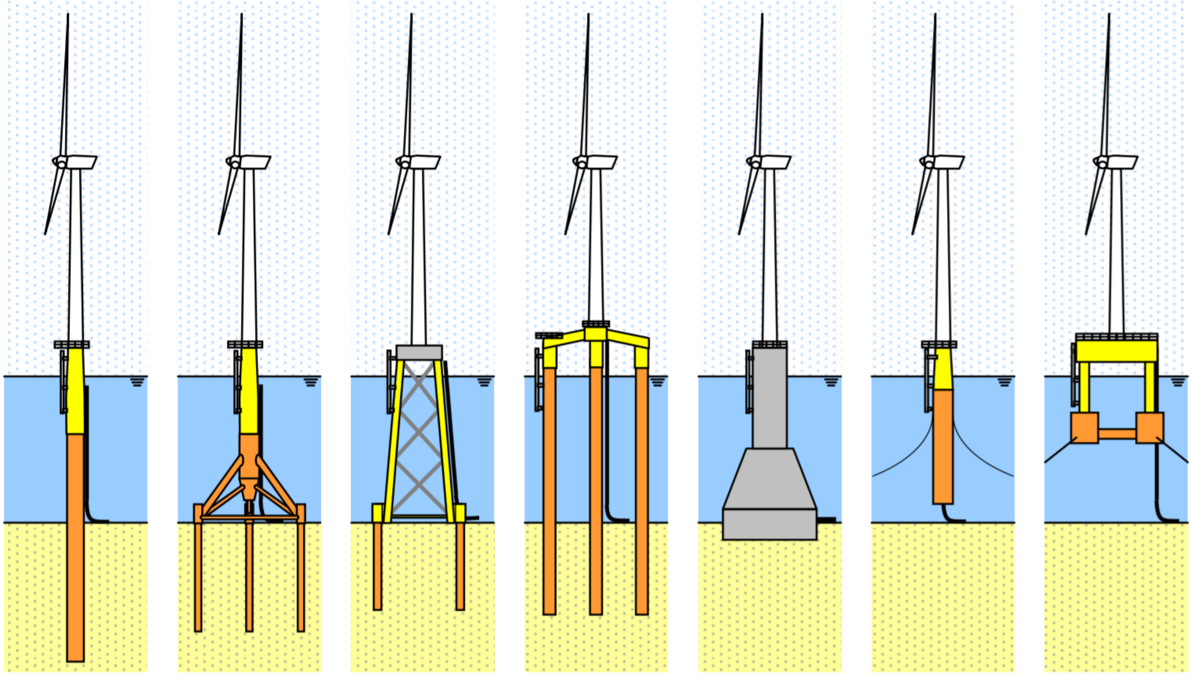

Figure 1.1: Fixed and floating support structures for offshore wind turbines. From left to right: monopile, tripod, jacket, tripile, gravity based, SPAR and semi-submersible sub-structures (de Vries et al., 2011).

Since most of Europe's offshore wind farms have been built by the northern countries, icy conditions may occur during the winter and have to be designed to operate safely. There are different ice features which are depending on their geographical location. E.g. in the Baltic Sea, first-year ice, level ice or ice floes can occur. Thus offshore wind sub-structures have to withstand these. Ice can fail in multiple ways: creep, crushing, bending, buckling, splitting and spalling, depending on ice properties and interaction geometry. These different failure modes result in different design scenarios for structures (Løset et al., 2006). Offshore wind sub-structures are mostly flexible structures and therefore can experience three well-defined types of structural vibrations due to the interaction between the ice and structure. These are called ice-induced vibrations. A lot of extensive research has been done into understanding this phenomenon. A phenomenological model has been made by Hendrikse (2017) to simulate the behaviour of a vertically sided sub-structure in level ice. This model is 1D and suitable for monopile sub-structure, but has not been applied yet for multi-legged sub-structure.

During 2020 19% of all installed offshore wind turbines were with jacket sub-structures. At the end of 2020 there were 568 jacket sub-structures built with and without grid connection (WindEurope, 2020b). That is 9.9% of the cumulative number of foundations installed, which was 8% in 2018 (WindEurope, 2018). At the end of 2017, the Wikinger wind farm was connected to the grid, which is located in the Baltic Sea, Germany (WindEurope, 2017). The Wikinger wind farm is designed for icy waters and has no braces around the mean sea level. WindEurope (2019a) expects that 9 GW of offshore wind could easily be deployed in the Baltic sea by 2030. With the right ambitions from Governments and regional cooperation, this is expected to increase beyond 14 GW of installed power.

The multi-legged sub-structures can have a problem that monopiles do not have, namely ice jamming. An ice jam occurs when ice fills the space between the legs of a multi-legged sub-structure. The legs and the jammed ice may then act as a single structural unit (Palmer et al., 2015). The International Organization for Standardization (ISO, 2019) standard no. 19906 uses Equation 1.1 to calculate the global ice action on a multi-legged sub-structure. k_j is used as a coefficient to account for ice jamming in the total global ice action, F_s. With F_1 being the ice action on one leg, which can be calculated with Annex A.8.2.4.3 for vertical and Annex A.8.2.4.4 for conical structures. k_s accounts for the interference and sheltering effects and k_n accounts for the effect of non-simultaneous failure.

$$F_s = k_s \cdot k_n \cdot k_j \cdot F_1 \qquad [N] \qquad (1.1)$$

The standard further elaborates on this coefficient, k_j: "Ice jamming between the legs can usually be expected if the L/w is less than 4. This can, but not necessarily always, lead to an increase in the ice action. Experimental data can clarify the influence of ice jamming in a particular design case.". L is, in this case, the clear distance between the legs and w is the width of the leg. Unfortunately, different letters are contributed to the clear distance or centre to centre distance. For this thesis, L is used as centre to centre distance and Q is used as clear distance thus if Q/w is less than 4 or L/w is less than 5, jamming is to be expected. If there is any chance that a jam may occur, both the unjammed and jammed case should be calculated, and the maximum value for ice action should be selected. It is emphasised that the characterisation of ice jamming can be complex.

Model tests with two conical multi-legged sub-structures (one with upward breaking and one with downward breaking legs) were performed by Kato et al. (1994). The L/w ratio was 2.7 at the waterline. Deep jamming was observed without exception for the downward bending cone, and it did not occur for the upward bending cone. An increase in ice loading was measured for the downward bending cones. Although it was not in their scope of the project, they concluded based upon the observations that an extra force due to the jamming should be included for predicting the ice force of a downward bending cone. Field observations show that jamming does not only occur for downward bending cones but also for vertical sided sub-structures. The Chinese JZ-20 platform in the Liao Dong Bay consists of four cylindrical legs with diameters of 1.7 m and spacing between leg centres of about 7.3 m (L/w ratio ≈ 4.3, Q/w ratio ≈ 3.3). An ice jam was observed between the legs of the platform and the accumulated thickness reached 4-7 m (Fan and Jin, 1990).

1.2. Thesis objective

The increasing need for renewable energy has sped up the development of offshore wind farms. To increase the efficiency while reducing the CAPEX and OPEX per MW, the offshore wind farms have been pushed further offshore into ice infested waters. Due to an increasing water depth, the multi-legged sub-structures have become favourable. However, multi-legged sub-structures may encounter ice jamming between the legs of the structure. Currently, this phenomenon has been observed for model scale downward bending cones and in the field for a vertical sided sub-structure. The ISO (2019) standard 19906 recommends an ice jamming factor, k_j, based upon model test findings, and it states that an ice jam may or may not lead to an increase in ice action. Which leads to the following objective:

"Evaluate and quantify the effects of an ice jam on the ice-induced vibrations of a vertical sided multi-legged sub-structure while encountering large ice floes of level ice."

To achieve this objective, the following research questions are identified:

- How and when does an ice jam originate based upon literature?
- What is the pressure distribution of an ice jam on the legs of a multi-legged sub-structure?
- How does an ice jam influence ice-induced vibrations of a multi-legged sub-structure?

1.3. Scope of research

The scope of the thesis is to investigate and research the impact of an ice jam on vertical sided multi-legged sub-structures while encountering large ice floes. From model tests and field observations, this phenomenon has been observed, and it could lead to an increase in ice action. The goal is to evaluate this influence and if it leads to an increase or decrease in ice action. Special ice features, e.g. ridges, icebergs, and ice rubble, which may be included in ice floes, are not considered. In this thesis sea ice and ice are interchangeable. The quantification of how ice jams occur and form is not part of this scope due to the complex nature of ice jamming. The ice jam is modelled as a continuum between the legs. As the multi-legged sub-structure the reference jacket support structure from phase I of the IEA Wind Annex Offshore Code Comparison Collaboration Continuation (OC4) workgroup is used as guidance. Because this structure is well defined and described by Vorpahl et al. (2011).

The phenomenological model as used in Hendrikse and Nord (2019) and developed by Hendrikse (2017) will be used to quantify the global ice load. COMSOL Multiphysics simulation software will be used to model the structure and ice jam. The dynamic interaction of the ice jam with the legs of a multi-legged sub-structure will be calculated using the COMSOL Multiphysics simulation software. The Livelink for MATLAB will be used to call the phenomenological model in order to obtain the global ice load.

1.4. Thesis structure

This thesis will focus on the effects of an ice jam on the ice-induced vibrations of a multi-legged sub-structure. First, a literature study is performed on the characteristics of ice and its interaction with multi-legged sub-structures, Chapter 2. Subsequently, a conclusion is drawn in Chapter 3. In which a list of requirements for the model is made. Afterwards, the model methodology and model scenarios are elaborated on, Chapter 4. The results of the different scenarios are shown in Chapter 5. Then the results are evaluated, discussed and put in a broader perspective in Chapter 6. After that, the conclusions can be found in Chapter 7. At last, recommendations for further research are given in Chapter 8.

2

Ice actions on multi-legged sub-structures

Ice actions are the result of interaction between various ice features and a structure. The ice conditions, the size and shape of the structure and the environmental driving actions can result in several different interaction scenarios, failure modes and resulting ice actions. The definition of action is defined as an external load applied to the structure (direct action) or an imposed deformation or acceleration (indirect action) (Løset et al., 2006; ISO, 2019). Thus ice actions are these actions imposed by ice. The major factors affecting and influencing the ice action can be seen in Figure 2.1. The most relevant parameters for ice jamming are highlighted in blue, and all parameters are discussed in this chapter.

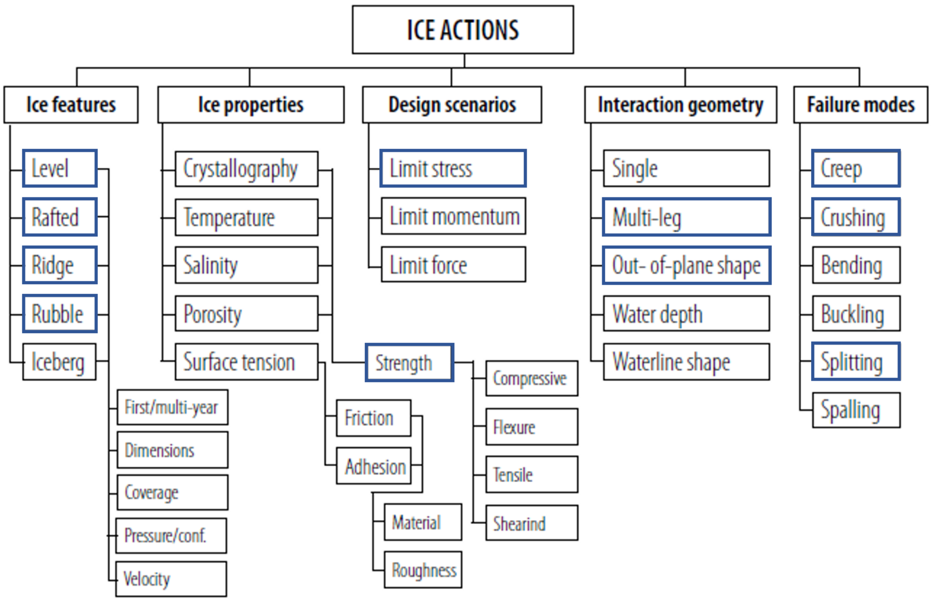

Figure 2.1: The major parameters affecting the ice action (Løset et al., 2006). In blue highlighted parameters are the most relevant for ice jamming.

First, the basics around sea ice need to be understood to understand the behaviour of an ice jam and its influences on the ice-induced vibrations. In Section 2.1 the development of ice and ice features, properties, strengths and mechanics will be discussed. In Section 2.2 the structural properties together with the interaction scenarios will be elaborated upon. Then in Section 2.3 the multi-leg effects are discussed. Afterwards, in Section 2.4 the formation of ice jams is looked at. How do they form, and what kind of effects do they have. Subsequently, Section 2.5 will be about the different failure modes that occur, and at last Section 2.6 elaborates on the three different ice induced vibrations regimes.

2.1. Sea ice

Depending on local conditions, sea ice can form in numerous manners and different types. The most relevant ice features for this thesis are level ice, rafted ice, ridges, and ice rubble. The level and rafted ice are the incoming ice that the structure has to encounter. The ice rubble is an important parameter for the origination of the ice jam. The ice ridge is an important phenomenon because the keel consists of rubble, like an ice jam. There has been done more research into ice ridges than ice jamming. Thus, that research could give insights into ice jamming. The dimensions of the incoming ice will be large relative to the structure so that the velocity and coverage are constant, e.g. an infinite ice floe with a constant velocity hitting the structure. First, the development of ice cover will be discussed. Then the ice features will be briefly explained. Afterwards, the different important ice properties are discussed. Then the resulting strengths of the ice are discussed, and at last, the ice mechanics are explained.

2.1.1. Development of ice cover

It starts with the growth of new ice crystals, the type of initial ice layer depends on the sea state. If the sea is calm, a thin layer of large separate crystals develops quickly on the ice surface. The crystals are minute spheres of ice and quickly grow into disc shapes. At a certain point, these disc shapes become unstable, and the crystals take on a hexagonal, stellar form, with long arms like dendritic stars (Arakawa, 1954), the crystal structure can be seen in Figure 2.2a. As can be seen in Figure 2.2b the ice crystal has a preferred growth direction along the a-axis in the basal plane. Suppose the sea is rough due to wind and waves. Free-floating crystals, which are disc-shaped, form a suspension in the top layer of the water column because the energy from the disturbance overcomes the buoyancy forces. An ice type called frazil or grease ice develops (Martin and Kauffman, 1981). Now there is an initial layer called primary ice. These different orientated hexagonal ice crystals continue to grow downwards. For different orientations, this downward growth is faster than others. The direction of easiest growth is parallel to the direction of the heat flow (vertical). Thus a horizontal c-axis is preferred, as can be seen in Figure 2.2c. The vertical c-axis do not grow fast enough downwards and are 'wedged out' by the horizontally oriented c-axis crystals (Deville, 2008). This vertical region in which the orientation of crystals is changing rapidly is called the transition zone and is roughly 0.05-0.3 m thick. In calm seas, it starts at the surface, and for rougher seas, it starts at the base of the frazil layer. The zone beneath the transition zone is called the columnar zone, which has a fairly uniform structure. Its dominant ice crystals have their c-axis horizontal (Løset et al., 2006). See Figure 2.3 for these different zones.

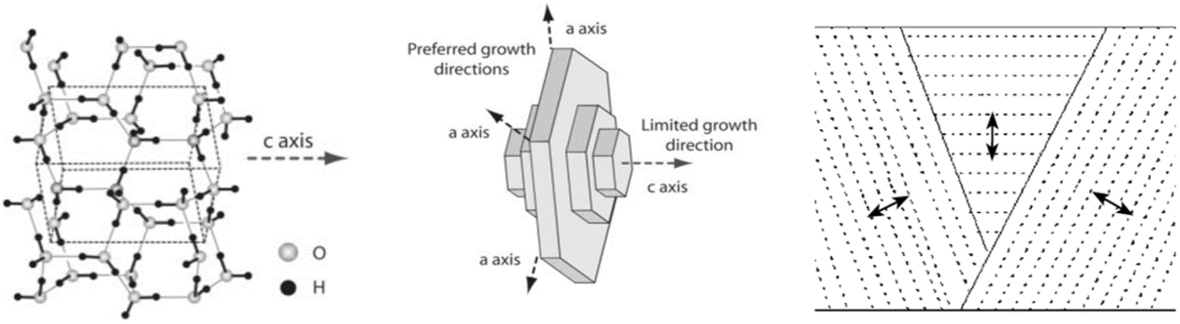

(a) Crystal structure of ice, perpendicular to c-axis is the basal plane (Deville, 2008).

(b) Morphology of growing crystals, a axis is in basal plane (Deville, 2008).

(c) Growth of different oriented crystals, arrows show c-axis (Ashton, 1986).

Figure 2.2: Crystal structure of ice (a), the morphology of growing crystals (b) and the gradual extinction of vertical oriented c-axis crystals (c).

Brine

Seawater contains salt. However, as can be seen in Figure 2.2a the crystal structure only consists of water and oxygen atoms. Thus where did the salt go? The salt got entrapped in pockets between the columnar ice. This highly saline solution is called brine (Weeks and Ackley, 1986). Due to the salt, the freezing point is lower, and the brine does not freeze. The salt is 'pushed' out as the ice crystals grow and accumulate in these brine pockets. Where it then slowly melts the ice underneath and travels downwards. An elaboration on this process can be read in Petrich and Eicken (2010), see Figure 2.3 for a brine pocket and drainage hole.

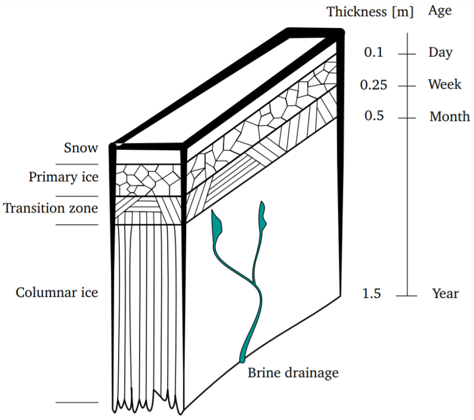

Figure 2.3: A cross-section and characteristics of an ice sheet (Willems, 2016).

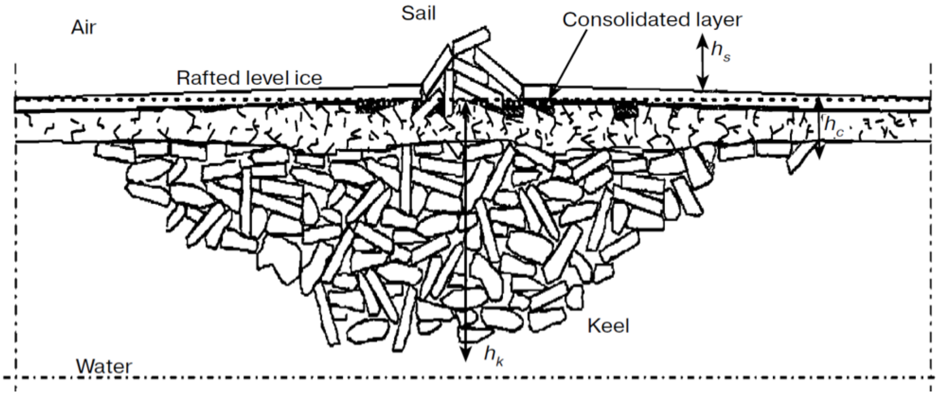

Figure 2.4: A cross-section and characteristics of an ice ridge (Løset et al., 2006).

Stages of ice cover

In calm seas, this new ice will gain thickness while elastically bending on waves and swell. This thin sheet of new ice is called nilas, which can measure up to 0.1 m. In turbulent seas, the ice keeps breaking, resulting in frazil accumulations that may take on various forms such as pancake ice, thickness up to 0.1 m. As the ice concentration increases, the pancake ice starts to consolidate into cover ice. Both are types of primary ice. An ice sheet of up to 0.3 m is called young ice. From 0.3 m, it is First-Year (FY) ice. The definition of FY ice is the ice of not more than one winter's growth. If ice has survived at least one summer's melt, it is called Multi-Year (MY) ice. Most of the MY ice features are smoother than FY ice due to erosion (Løset et al., 2006). The concentration of ice is described by the ratio expressed in tenths. Thus 10/10 means compact pack-ice, and no water is visible. While 2/10 means very open ice. Now the different ice features are discussed.

2.1.2. Ice features

Sea ice may be encountered in different types of features, depending on the physical processes it has undergone. Starting with no deformations is level ice. Broken pieces of ice are called ice rubble, which can be generated by natural or man-made destruction. Accumulation of rubble can cause rubble piles or fields. Rafted ice is a piece of ice that is overridden by another. This occurs likely for thinner ice (<0.4 m). Beyond this thickness, ridging is more likely to occur. A ridge is a line or wall of broken ice forced up by pressure or shear of pack ice. See Figure 2.4 for a cross-section including the characteristics. The underwater part of the ridge is called the keel, which can be several times the height of the visible height of the ridge (the sail). The keel of a ridge consists of a consolidated layer, a partly consolidated layer and many pieces of rubble which may or may not be partially frozen to each other (Løset et al., 2006).

These many pieces of rubble, which may be partially frozen to each other, can be called an ice jam, only between two ice sheets instead of a structure. In the ISO (2019) the Mohr-Coulomb criterion is suggested for ice rubble action formulation. This is a hydrostatic pressure-dependent model which uses two parameters, friction angle and cohesion. Based on this continuum, the keel action can be calculated with analytical methods. Which are suitable for applications which require short computational time runs, although these methods imply numerous assumptions. Numerical finite element models need to be used when a deeper understanding of the rubble behaviour is required. However, such a continuum approach is not suitable due to the large size of the ice blocks in comparison with the dimensions of the ridge/structure (Serré, 2011a). Thus several authors Liferov (2005), Polojärvi and Tuhkuri (2009) and Polojärvi and Tuhkuri (2013) use discrete element methods. Where the ice rubble is modelled as an assembly of discrete ice particles with finite strength, contacts and freeze bonds. However, for this dynamic problem, this would be too computationally expensive. Serré (2011b) uses the Drucker-Prager constitutive model, which is equivalent to the Mohr-Coulomb material law. But its mathematical formulation makes it more suitable for use with an explicit finite element method.

Visually FY ridges often have sharp peaks and slopes of up to 40° to the horizontal, while MY ridges are more weathered down with rounded peaks and slopes of 20/30° to the horizontal. A grounded ridge is called a stamukha (Løset et al., 2006).

2.1.3. Ice properties

The microscopic properties determine ice properties: distribution, size, orientation and shape of the ice crystals (Petrich and Eicken, 2010). In Section 2.1.1 the micro- and macro-structure of ice was briefly covered, but for more information and in-depth explanation review the work of Petrich and Eicken (2010), Løset et al. (2006) or Schulson and Duval (2009). These microscopic properties can be captured on a larger scale with the following physical parameters, which play an important role in the strength of the ice: crystallography, temperature, salinity and porosity.

Crystallography

The crystal structure is different along the cross-section of an ice sheet. As can be seen in Figure 2.3 the grains are random in the primary ice, also called granular ice, thus having isotropic behaviour (the same physical behaviour in different directions). In the columnar ice the grains are laminar, resulting in anisotropic behaviour (different physical behaviour in different directions). Young and FY ice can have different crystallographic profiles, as can be seen in Figure 2.3. Over time, the columnar zone will be dominant, and the granular zone can be neglected. Thus the ice can be seen as anisotropic (Løset et al., 2006).

Temperature

According to Løset et al. (2006) temperature is along with loading rate ($\dot{\sigma}$ or $\dot{\epsilon}$, these parameters will be discussed in Subsection 2.1.5) the most important parameter for the mechanical behaviour of ice. Temperature has two important effects on ice. Firstly it affects the mechanical behaviour, ice becomes weaker (lower strength, σ) and softer (lower Young's modulus, E) for an increase in temperature and vice versa (Løset et al., 2006). Secondly, any change in temperature affects the porosity and pore micro-structure of the ice as well as the salinity and chemical composition of brine (Petrich and Eicken, 2010). The temperature relation along the ice thickness is almost linear. The temperature at the surface is roughly equal to the air temperature, and the temperature at the bottom is equal to the melting temperature, as can be seen in Figure 2.5.

Salinity

The salinity profile of ice during a year is visible in Figure 2.6. Two things can be noticed. Firstly the salinity is relatively low compared to ocean water (around 33 percentile vs. 8 in the sea-ice). Secondly, there is a characteristic C-shape of the young and FY ice. A higher concentration in the top and bottom while having a lower concentration in the middle region of the ice. The overall reduction in sea ice salinity is due to molecular diffusion and advection in the pore network and ocean turbulence at sea ice-ocean transition. Three processes drive the evolution of sea ice during the winter: a net hydrostatic pressure, mostly due to the difference in density between brine in the ocean and sea ice; pressure fluctuations at the sea ice interface; and a small contribution due to volume expansion during freezing (brine exclusion). The brine is slowly draining during the winter, resulting in fewer brine pockets and thus stronger ice. In the summer melt season, meltwater will reduce the surface salinity. (Petrich and Eicken, 2010)

Porosity

Porosity is a measure of how much void (i.e. "empty") space is in the material. It is the fraction of the volume of void divided by the total volume. In ice, the void volume is calculated as the volume of everything that is not ice. This can be gas/air or brine see Equation 2.1. These pockets are weaknesses in the structure. The size of these pockets depends on temperature and salinity (Petrich and Eicken, 2010).

$$\nu_T = \nu_b + \nu_a = \frac{V_{air} + V_{Brine}}{V_{total}} \qquad [-] \tag{2.1}$$

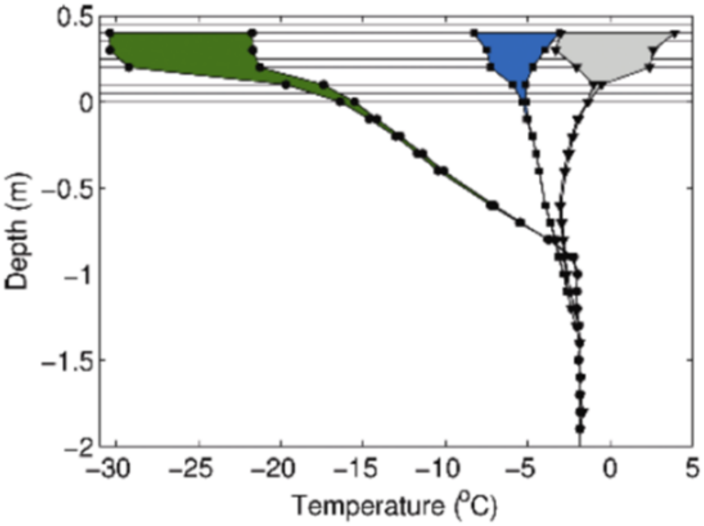

Figure 2.5: Vertical temperature profiles measured with a thermistor probe frozen into the ice in Barrow, 2008. Positive depths are snow and air, negative depths are sea ice and ocean. Profile show the temperature range encountered over a 24-hour period in mid February (day 45, circles), mid-May (day 135, squares) and at the end of May (day 150, triangles) (Petrich and Eicken, 2010).

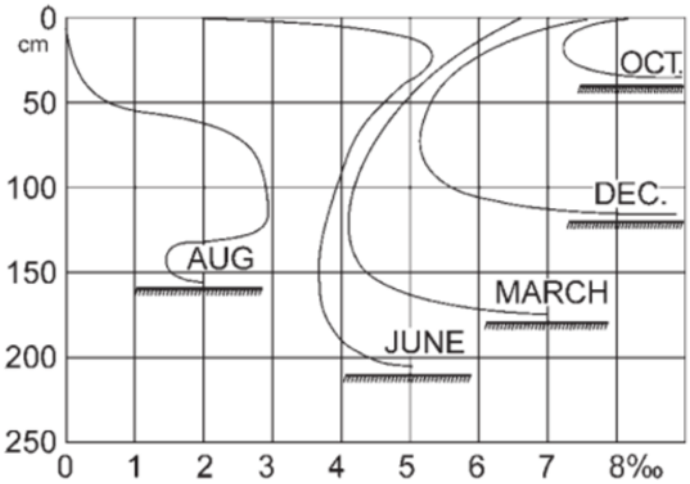

Figure 2.6: Evolution of sea-ice salinity profiles (from Malmgren, 1927). Note the characteristic C-shape of the young and FY ice salinity profile and the reduction in surface salinity due to meltwater flushing with the onset of summer melt (Petrich and Eicken, 2010).

2.1.4. Ice strength

The above mentioned physical parameters are important for the ice strength. These parameters fluctuate throughout the ice sheet. Thus the ice strength varies depending on the location and the type of loading. There are different strengths for the different types of loading. The ice sheet may be loaded by crushing, bending, shearing or a combination of those. A lot of testing and modelling has been done to get the following empirical formulas for different ice strengths, Equations 2.2 - 2.7. These formulas give insight into which of the parameters mentioned above affects these types of strengths the most and indicate the ratio between them. A large number of relevant parameters makes correlation between strength and the sample difficult. Thus often, the most critical parameters are chosen to make the best fit.

Compressive strength

For vertically sided structures crushing is of importance for the ice-structure interaction. In Timco and Frederking (1990) the results of 283 small-scale strength tests were used to make a model and they came with the following empirical formulas for columnar and granular ice, Equations 2.2 - 2.4. The vertical strength, σ_c^V, is roughly three times stronger than the horizontal strength, σ_c^H, for columnar ice. For granular ice, there is Equation 2.4 which can be used for vertical and horizontal directions since granular ice is isotropic. These equations are a function of the strain rate, $\dot{\varepsilon}$ and the porosity, ν_T. The strain rate is relevant because of ductile vs brittle behaviour, which will be explained in Section 2.1.5. The relevance of porosity is explained above. These equations are to be valid for a strain rate from $10^{-7}s^{-1}$ to $10^{-4}s^{-1}$ and a porosity up to about 0.2 (Timco and Frederking, 1990). Note that these equations are best fit and represent the strength of the given properties. These properties vary over an ice sheet, thus with it its strength (Løset et al., 2006).

$$\sigma_c^H = 37 \cdot (\dot{\varepsilon})^{0.22} \left[1 - \sqrt{\frac{\nu_T}{0.27}}\right] \qquad [MPa] \tag{2.2}$$

$$\sigma_c^V = 160 \cdot (\dot{\varepsilon})^{0.22} \left[1 - \sqrt{\frac{\nu_T}{0.20}}\right] \qquad [MPa] \tag{2.3}$$

$$\sigma_{c_{granular}} = 49 \cdot (\dot{\varepsilon})^{0.22} \left[1 - \sqrt{\frac{\nu_T}{0.28}}\right] \qquad [MPa] \tag{2.4}$$

Tensile strength

Tensile strength determines the maximum tensile stress that the ice can yield before failure. It represents an important failure mode when ice interacts with an offshore structure. Large areas of sea ice often show a large number of leads. These leads are the result of tensile failure. There have not been many tests performed to measure the tensile strength of ice due to the complex nature of testing (Timco and Weeks, 2010). In Timco and Weeks (2010) the results of four different tensile strength tests of FY ice have been plotted, and a fit to the data yields Equation 2.5. From these tests, they noticed that the tensile strength is a strong function of temperature and thus porosity, but little influenced by loading rate, $\dot{\varepsilon}$. Note that these tests were performed in the horizontal frame and when tensile stresses were tested parallel to the growth direction, the strength was about three times higher.

$$\sigma_t = 4.278 \cdot \nu_T^{-0.6455} \qquad [MPa] \tag{2.5}$$

Flexural strength

The tensile strength and flexural strength should be equal, provided the assumption that ordinary beam theory applies. However, as excepted, this is not the case. Tensile strengths are measured from small scale tests uni-axially, while flexural strengths are measured from cantilever beam or simple beam tests. The conditions throughout the beam are fluctuating, temperature and salinity gradients are present. The resulting flexural strength is an average value of the stress in the critical point at failure. These results still prove to be useful since the failure of ice against an inclined structure or ship is similar (Løset et al., 2006). During in situ and laboratory tests, the equations used to calculate the flexural strength assume that the ice is homogeneous and perfectly elastic. If this was the case, the flexural strength would be approximately equal to the tensile strength. But this is certainly not true for sea ice. Although there are many limitations, the tests are a reasonable approximation for applications (Timco and Weeks, 2010). Timco and O'Brien (1994) analysed 2495 measurements on the flexural strength of freshwater ice (1556 tests) and sea ice (939 tests), which resulted in

Equation 2.6. The flexural strength, σ_f, is in MPa and ν_b is the brine volume fraction (0-1). This equation is compiled from a variety of geographical locations thus, it should be quite representative.

$$\sigma_f = 1.76 \cdot \exp\left(-5.88\sqrt{\nu_b}\right) \qquad [MPa] \qquad (2.6)$$

Shear strength

Ice floes interacting with structures are often under a combination of uniaxial or multi-axial compressive stress. However, parts of the interaction zone are also possible to be subjected to bi-axial stresses involving tensile and compressive stresses, also known as shear. Thus the shear strength is an important property. However, testing and interpreting shear strength tests is difficult. It is assumed that the shear stress is generated on a plane of failure. However, in most cases, normal stresses are also generated on the plane of failure. Frederking and Timco (1986) performed a linear regression on the shear strength data from the studies Timco and Frederking (1986) and Paige and Lee (1967) which resulted in Equation 2.7. It should be noted that ice loaded with shear conditions would fail in tension rather than shear. Thus the shear strength is actually governed by tensile strength (Timco and Weeks, 2010).

$$\tau = 1.5\left(1 - \sqrt{\frac{\nu_t}{0.39}}\right) \qquad [MPa] \qquad (2.7)$$

2.1.5. Ice mechanics

When the load exceeds the strength of the material, failure will occur. However, before failure, deformation may take place. The combination of deformation and failure is known as mechanical behaviour (Willems, 2016), which is necessary to understand for Section 2.5 Failure Modes. Large deformations before failure are known as ductile behaviour. Failure without appreciable deformation is known as brittle behaviour. Ice is a polycrystalline material and behaves in principles like metals, with ductile and brittle behaviour. However, ice is much more complicated than metals due to two important facts. The grain size is relatively large, and ice in its natural state exists close to its freezing point. Furthermore, sea ice exists of pure ice, brine, air and sometimes solid salts. Thus an ice model would need to include linear and non-linear aspects of elasticity, visco-elasticity, visco-plasticity and fracture. The temperature, along with the loading rate, are the most important parameters for mechanical behaviour. Loading rate can be expressed with the strain rate, $\dot{\varepsilon}$, or the stress rate, $\dot{\sigma}$ (Løset et al., 2006). When ice is loaded slowly, it will behave ductile, and it will behave brittle when it is loaded rapidly, see Figure 2.8. The compressive strength increases for increasing strain rate until it reaches brittle behaviour, then the strength decreases (Schulson, 1997). Thus, the mechanical behaviour consists of ductile, transitional and brittle behaviour. Which will be explained in this section. See the work of Schulson and Duval (2009) and Sinha (1983) for a more elaborate explanation.

Ductile behaviour

The ductile behaviour of a material can be examined with a creep test. In a creep test a load, σ_0, is applied at $t = t_0$. This load is held constant for a certain duration and released at t_1. Meanwhile, the response is measured over time. Figure 2.7a is the measured response while Figure 2.7b is the applied load. The total strain consists of different components, elastic, visco-elastic and visco-plastic strain, see Equation 2.8 (Sinha, 1983).

$$\varepsilon_{tot} = \varepsilon_e + \varepsilon_{ve} + \varepsilon_{vp} \qquad [mm/mm] \qquad (2.8)$$

ε^e is the immediate elastic strain, ε^{ve} is the visco-elastic strain and ε^{vp} is the visco-plastic strain. Visco means time-dependent. The immediate elastic behaviour is time-independent and can be evaluated by Hooke's law, see Equation 2.9. The visco-elastic strain is the delayed time depended strain see Equation 2.10. For the (visco-)elastic deformations, the energy is eventually recovered when the load is removed, and the sample returns to its original form. The visco-plastic strain is the permanent or viscous deformation see Equation 2.11. All the energy is dissipated, and thus the material cannot recover (Sinha, 1983).

$$\varepsilon_e = \frac{\sigma}{E} \qquad [-] \qquad (2.9)$$

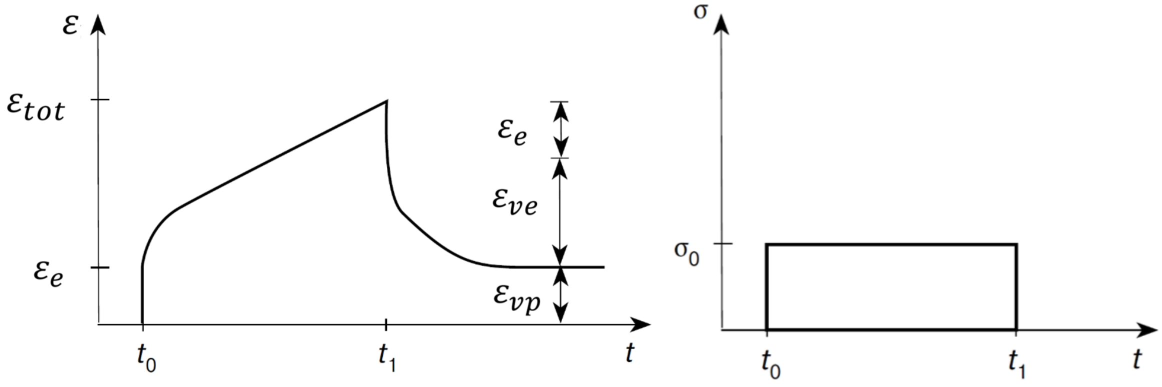

(a) Measurement of the strain components over time.

(b) Applied loading over time.

Figure 2.7: A creep test for an elastic, visco-elastic and visco-plastic material Løset et al. (2006).

Where the time independent strain, ε_e, is calculated by the fraction of the stress, σ, over the elasticity modulus, E. This is the one-dimensional case. For three dimensions, the stress and strain are tensors with three normal and three shear components. The elasticity modulus is a six-by-six matrix consisting of 36 components. The visco-elastic strain, ε_{ve}, can be calculated by the Equation 2.10. As can be seen, this equation is now a function of the time, t. It further consists of the average grain diameter, d, the unit of grain diameter, d_1, and the constants c_1, a_T and b. s is the stress exponent for delayed elasticity, and a_T is the inverse of relaxation time at temperature, T Sinha (1983).

$$\varepsilon_{ve} = c_1 \left(\frac{d_1}{d}\right)\left(\frac{\sigma}{E}\right)^s \left\{1 - \exp\left[-(a_T \cdot t)^b\right]\right\} \qquad [-] \qquad (2.10)$$

If the load is applied slowly, the ice will deform irreversibly besides the elastic deformations. This is viscous strain, which is called creep. When the load is removed, the deformations are permanent. The energy is dissipated in the dislocations of the ice crystals. This time depended, permanent behaviour can be formulated by Equation 2.11. In which the viscous strain, ε_{vp}, is a function of the viscous strain-rate, $\dot{\varepsilon}_{V1}$, for the unit stress, σ^1. The constant, n and the time, t. $\dot{\varepsilon}_{V1}$ is dependent on temperature (Sinha, 1983). During this irreversible deformation, strain-rate hardening will occur. This means that the ice strength increases. However, non-propagating grain-sized micro-cracks occur at higher strain-rates within the ductile regime due to the dislocations known as strain-rate softening (Schulson and Duval, 2009).

$$\varepsilon_{vp} = \dot{\varepsilon}_{\mathrm{V}_1} \left(\frac{\sigma}{\sigma^1}\right)^n t \qquad [-] \qquad (2.11)$$

Transitional behaviour

The transition from ductile to brittle is a gradual transition instead of an abrupt change in mechanical behaviour. This transition is the cause of the strain-rate hardening (ductile behaviour) and strain-rate softening (brittle behaviour) due to these dislocations and formation of micro-cracks, respectively. The intersection point between ductile and brittle is where the resistance or strength is the highest, as can be seen in Figure 2.8 (Schulson and Duval, 2009).

Brittle behaviour

The brittle behaviour is characterised by a stress-strain curve that rises pseudo linearly and fails at the terminal failure stress. At higher strain-rates no ductile behaviour will occur. Load-drops characterise the stress-strain curve in compressive strength. These load-drops are related to the creation and growth of micro-cracks which is also known as strain-rate softening, reducing the terminal failure stress (Schulson and Duval, 2009).

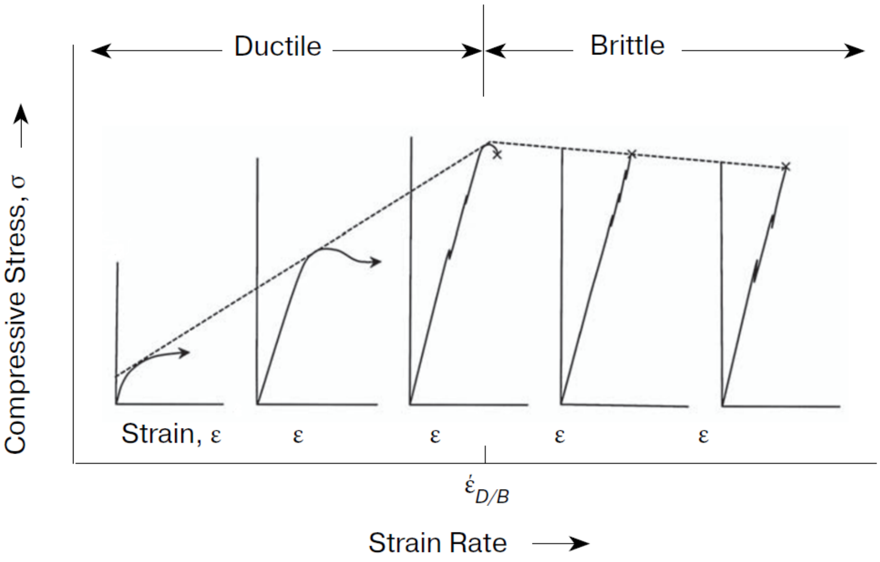

Figure 2.8: The transition from ductile to brittle as a function of strain rate. The terminal failure stress is denoted with x (Schulson, 1997).

2.2. Multi-legged support structure

An important factor is the support structure. It consists of the sub-structure type (mono-pile or multi-legged), the out-of-plane form at the waterline area (conical or vertical) and the structure's size. Structures with vertical sides at the waterline are subjected to higher actions than inclined sides because the strength of ice in bending is less than in compression. However, sloping structures have a larger waterline area increasing hydrodynamic loading and are more complex to build. The size of the structure is important due to the existence of the scale effect. Which says that the effective pressure (the total action divided by the nominal contact area) for a narrow structure is higher than for a wide structure (Løset et al., 2006). Sanderson (1988) demonstrates that the effective pressure depends inversely on the square root of the nominal contact area, thus depending on the size. Besides the scale effect, there is also the size effect on the structural strength. The effect that the nominal strength of an ice feature decreases when the size of the interaction problem increases, under the condition that geometrically similar interaction problems are considered. The ice is as strong as its weakest connection, and a larger ice floe has a lot more connections than a small ice floe. Thus the size of the ice-structure interaction plays an important role (Løset et al., 2006).

First, the equation from the ISO (2019) 19906 standards will be discussed. Then the structural properties for the industry standard offshore wind turbine are given, and at last, the different interaction scenarios for designing structures are elaborated on.

2.2.1. Leg effect coefficient

Equation 2.12 is used according to the ISO (2019) 19906 standard to calculate the global limit stress action, F_s, on a multi-legged structure. k_s accounts for the interference and sheltering effects, k_n accounts for the effect of non-simultaneous failure, k_j is used as coefficient to account for ice jamming and F_1 is the ice action on one leg. F_s, k_s, k_n and k_j are further elaborated on in Sections 2.2.3, 2.3.1, 2.3.2 and 2.4, respectively.

$$F_s = k_s \cdot k_n \cdot k_j \cdot F_1 \qquad [N] \qquad (2.12)$$

$$k = k_s \cdot k_n \cdot k_j \qquad [-] \qquad (2.13)$$

For model and numerical tests, these different coefficients can also be described by a single coefficient k. This is more practical because, during tests, the total force, F_s, is measured, which then can be divided by the ice action on one leg, F_1. This value can be measured by means of a control test with one leg. Karulin and Karulina (2014) calculated this coefficient based upon data from different experimental scenarios and compared them with the numerical calculations from Shkhinek et al. (2009), who in their research compared it with the ISO (2019) 19906 standard. The standard gives a maximal value for k in the range of 3.0-3.5. The theoretical and experimental values were lower than that except for 1 test. The k value was in the range of 1.5-3.00 (excluding the 3.62 for that 1 test). A higher k was seen for higher ice velocities and for a larger gap between the legs. The latter can be explained due to an increase in overal width of the structure.

2.2.2. Structural properties

An industry standard wind turbine is defined by Jonkman et al. (2009) to support concept studies aimed at assessing offshore wind technology. Here, the NREL 5-MW Offshore Baseline Wind Turbine is defined, which helps the industry obtain comparable information with this standardised wind turbine to make a fair comparison. In March 2020, a new NREL 15-MW Offshore Reference Wind was published by Gaertner et al. (2020). To keep ahead of the development curve. Currently, the average offshore wind turbine in Europe is 8.2 MW (WindEurope, 2020a). Unfortunately, its sub-structure is a monopile. Because of this, the old reference turbine is used. In the International Energy Agency (IEA) Wind Annex Offshore Code Comparison Collaboration Continuation (OC4) project the UpWind reference jacket model developed by Vemula et al. (2010) is used with the NREL 5-MW wind turbine and this model is described by Vorpahl et al. (2011). The jacket support structure is designed for a deep water site in 50 m of water. The four-legged jacket is supported by piles, which are modelled as being clamped at the seabed. There are four levels of X-braces, mud braces and four grouted piles with a penetration depth of 45 m. The transition piece (TP) connects the jacket with the tower, see Figures 2.9a and 2.9b. The properties of the relevant components are given in Table 2.1, and below it, some physical and damping properties are given:

Table 2.1: Properties of the reference jacket.

Component	Color in Figure 2.9b	Outer diameter [m]	Thickness [mm]
x- and mud braces	grey	0.8	20
leg at Section 1	red	1.2	50
legs at Sections 2 to 4	blue	1.2	35
leg crossing TP	orange	1.2	40

The properties of the steel for the whole jacket are given here below: density, ρ, Young's modulus, E and Poisson's ratio, ν.

$$\rho_{steel} = 7850\ [kg/m^3], \quad E_{steel} = 2.1 \cdot 10^{11}\ [N/m^2] \quad \text{and} \quad \nu_{steel} = 0.3\ [-]$$

Furthermore, the critical structural-damping ratio, $\zeta_{structure}$ and the corresponding logarithmic decrement, $\delta_{structure}$ for all modes are defined as follows:

$$\zeta_{structure} = 1\ [\%] \quad \text{and} \quad \delta_{structure} = 6\ [\%]$$

The reference jacket, as can be seen in Figure 2.9a, has braces at the mean sea level (MSL). In icy waters, this is not common due to its impact on the potential interaction width and area. The interaction width plays an important role in the increase in ice action. In Figure 2.9c a jacket support structure for the Baltic Sea is shown. The main discrepancy is around the MSL, where there are no braces. For this thesis, the MSL will be shifted towards the K-joint in between sections 3 and 4, see Figure 2.9a. Now there is clearance for the ice, albeit minimal. The new water depth is 54.38 m. By doing it in this manner, the reference jacket can still be used.

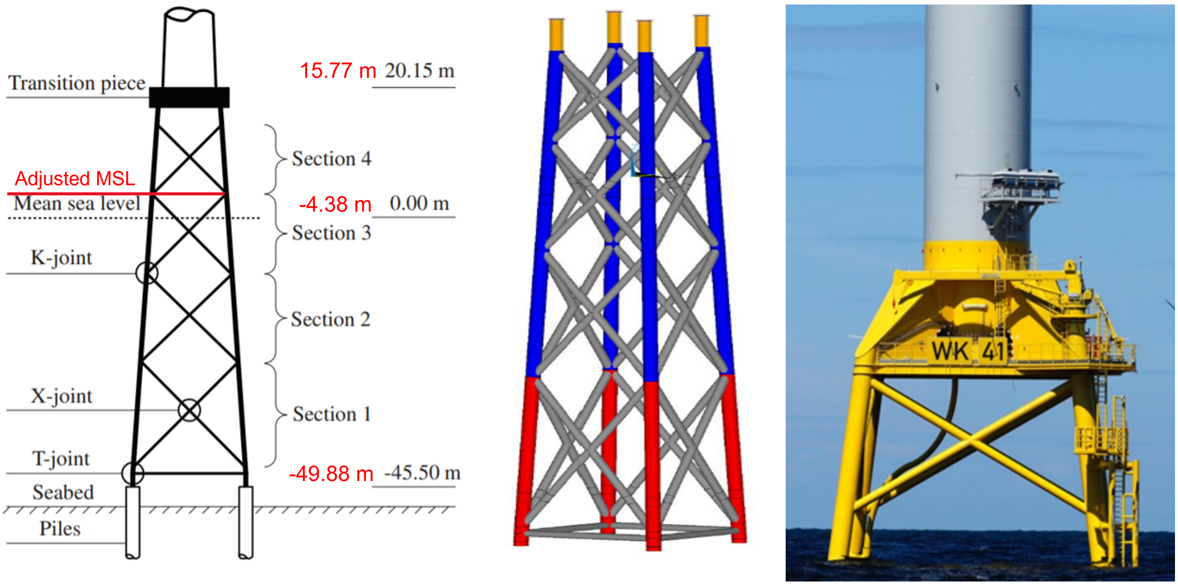

(a) Side view of the OC4 reference jacket Oest et al. (2017). The new situation with the adjusted MSL is shown in red.

(b) 3D model of the OC4 reference jacket Vorpahl et al. (2011).

(c) Side view of the Wikinger jacket by Iberdrola.

Figure 2.9: Side views of the OC4 reference jacket besides an existing jacket from the Wikinger wind farm in the Baltic Sea.

2.2.3. Interaction scenarios

There are multiply interaction scenarios that have to be taken into account while designing structures in icy waters. According to ISO (2019) there are three types of ice-structure interactions which have to be assessed. A so called limiting mechanism describes these. The definition of a limiting mechanism is "The interaction mechanism that limits the ice action on a structure". These three are limit stress, limit energy and limit force. Formulas to calculate these limits are given in ISO (2019) Annex A.8.2.4 Global ice actions. When more than one limiting mechanism can occur at the same time, the one with the lowest ice action is governing.

Limit stress

Limit stress is the mechanism that governs when there is sufficient energy or driving force to envelop the structure fully across its total width. Then the stress (compressive, tensile, flexure, shear, buckling) will reach a limit, and failure occurs. This scenario very often controls the maximum action Løset et al. (2006). The maximum ice action depends on the geometry and the failure mode. These different failure modes will be elaborated upon in Section 2.5.

Limit energy

Limit energy or limit momentum is the mechanism that is related to the momentum/kinetic energy of the ice feature. Often these mechanisms involve impacts from icebergs, refloated stamukhi, thick ice floes or ice islands. The ice action on a structure follows from the dissipation of kinetic energy. Due to eccentric impacts, a lot of energy can be dissipated by the rotation of the ice feature, thus mitigating the action relative to a head-on impact (ISO, 2019). The loss of kinetic energy is equal to the work done by the ice action on the structure by the ice feature see Equation 2.14. m is the mass, and v is the velocity of the ice feature. The force, F, interaction width, w, ice thickness, h and ice pressure, $p(x)$, may depend on the penetration x. If $v_{end} = 0$ then the maximum ice action for limit energy is the maximum of $F(x)$, see Equation 2.15.

$$\int F(x)dx = \int p(x)w(x)h(x)dx = \frac{1}{2}mv_{\text{beg}}^2 - \frac{1}{2}mv_{\text{end}}^2 \qquad [N] \qquad (2.14)$$

$$F_{LE} = max(F(x)) \qquad [N] \qquad (2.15)$$

Limit force

Limit force is the mechanism that is determined by the forces driving or pushing the ice feature against the structure. The ice feature and the structure do not deform and may be considered rigid. The driving forces may be due to direct ice actions, current drag, wind drag, and thermal expansion see Equation 2.16. The drag

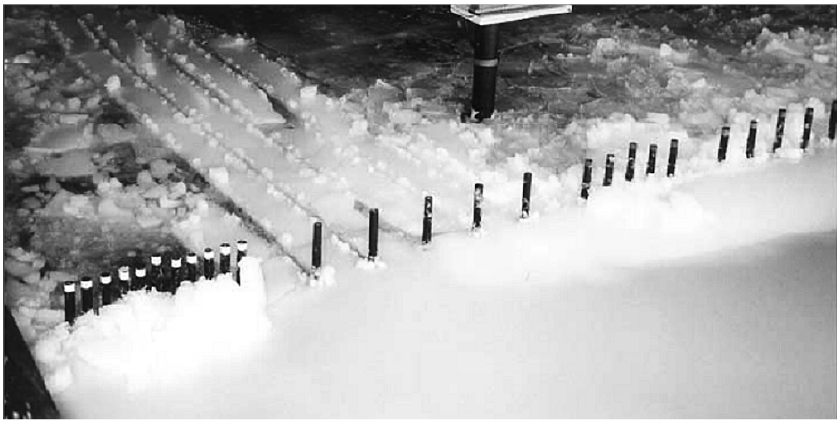

Figure 2.10: Model-scale testing of piles with different spacings (Gürtner and Berger, 2006).

component consists of a drag coefficient, C_d, density, ρ and velocity, V, of the medium and the diameter, D_{floe}. When the ice floe is not confined, the thermal expansion is equal to zero.

$$F_{LF} = F_{\text{direct}} + F_{d,\text{ wind}} + F_{d,\text{ current}} + F_{\text{thermal}} \quad [N] \tag{2.16}$$

$$F_d = \frac{\pi}{8} C_d \rho V|V| D_{\text{floe}}^2 \quad [N] \tag{2.17}$$

2.3. Leg interaction

Multi-legged sub-structures have multiple legs compared to a single leg for the monopile. This results in different interactions between the legs and the ice. Unfortunately, different terms are used, the clear distance over width and the centre-to-centre distance over width. E.g. in ISO (2019) L is used as clear distance variable while in Løset et al. (2006) and Timco and Pratte (1985) Q is used as clear distance and L is the center-to-center distance. In this thesis, Q is used as clear distance, and L is used as centre-to-centre distance. First, the sheltering and interference effects will be discussed in Section 2.3.1. Then in Section 2.3.2 the non-simultaneous failure effects are elaborated on.

2.3.1. Sheltering and interference effects

The sheltering and interference effects are accounted for in coefficient, k_s. The ice action depends on the centre-to-centre distance, L the clear distance, Q the diameter, D or width, w of the legs and the number of legs. The effect of pile spacing on the pile force and direction and failure behaviour of the ice has been studied by Timco and Pratte (1985) and Gürtner and Berger (2006), respectively. A numerical study on the leg influences of a four-legged structure was performed by Shkhinek et al. (2009). Karulin and Karulina (2014) performed model tests with a four-legged structure and compared their experimental data with the numerical study and the ISO (2019) 19906 standard.

In Gürtner and Berger (2006) there were several arrangements in which the centre-to-centre pile spacing varied from 2D to 8D as can be seen in Figure 2.10. The diameter was 30mm, and the ice thickness 6mm. The test models were scaled 1:16. Thus the actual pile diameter 0.48m and 0.1m for the ice thickness. The observations were that for an increasing centre-to-centre pile spacing, the amount of rubble generation decreased. The pile interaction was noticed up to and including a centre-to-centre spacing of 6D. For the pile spacing of 8D, there was no pile interaction observed. In Figure 2.10 the center-to-center spacing is from left to right 2D, 8D, 4D and 6D. Resulting in a Q/D of 1, 7, 3 and 5, for direct comparison with Figure 2.11.

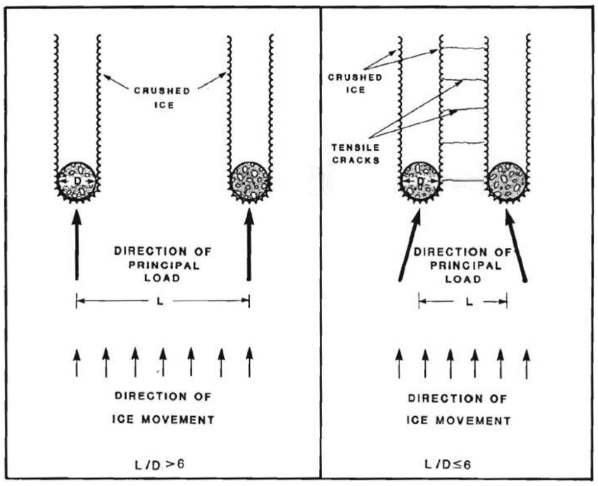

Figure 2.12: Influence of pile spacing on force direction and the formation of tensile cracks between the cylinders (Timco, 1986).

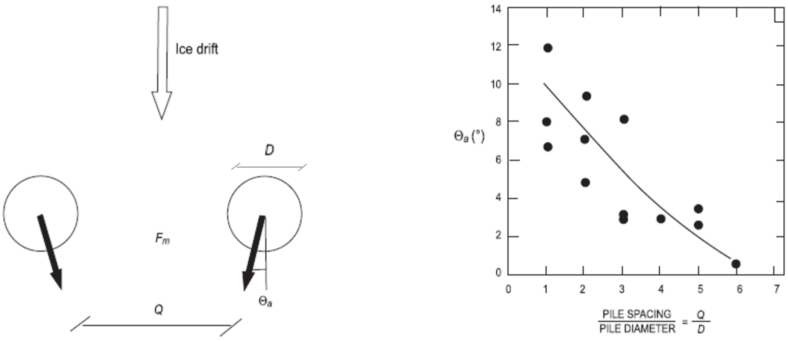

Figure 2.11: Left the situation sketch and right the direction of the load (θ_a) versus pile spacing (Timco and Pratte, 1985).

Timco and Pratte (1985) studied the direction of the pile force for an arrangement of 2 piles with varying pile spacing, see Figure 2.11. Notice that for the model tests of Gürtner and Berger (2006) the centre-to-centre distance is used while here, the clear distance, Q, is used. For a Q/D ratio higher than 6 the ice action does not show interference. As spacing increases, the transverse force component (perpendicular to the ice movement) decreases. The normal force component (in line with the ice movement) increases for increasing pile spacing. Thus for a small ratio, the normal force is higher for a single pile than a configuration of piles in the same conditions. The influence of the piles does not change the magnitude of the total ice actions but does change the direction.

There was no mention of the generation of ice rubble in the description of the experiments. However, the formation of tensile cracks were observed, see Figure 2.12. This formation is attributed to the lateral movement of the cylinders (Timco and Frederking, 1986).

Shkhinek et al. (2009) found numerically that up to a ratio of L/D = 5 the load on any leg is independent of influence of other legs and up to a ratio of L/D = 10 for a Jacket. Which coincides with the research mentioned above. Furthermore, they found that the maximum value of k for a four-legged structure in moving ice for longitudinal loads is about 2.8. However, their numerical experiments only went to L/D=10.

Experiments conducted by Karulin and Karulina (2014) show this pile influence effect beautifully, see Figure 2.13. They towed a 4 legged structure in a ice basin under 0°, 30° and 45° for 2 different L/D ratios, 2.5 and 6.0. The results are clear. The structure having an L/D ratio of 2.5 creates a wide channel with broken ice in its wake (Figure 2.13a). While the structure with an L/D ratio of 6.0 creates a number of ice strips equal to its number of legs (Figure 2.13b). Lateral/tensile cracks were observed in these ice strips.

One or several legs of a multi-legged structure can be fully or partially brought in a track formed by the other legs. These sheltered legs will interact with broken ice instead of level ice, which will lead to a reduction

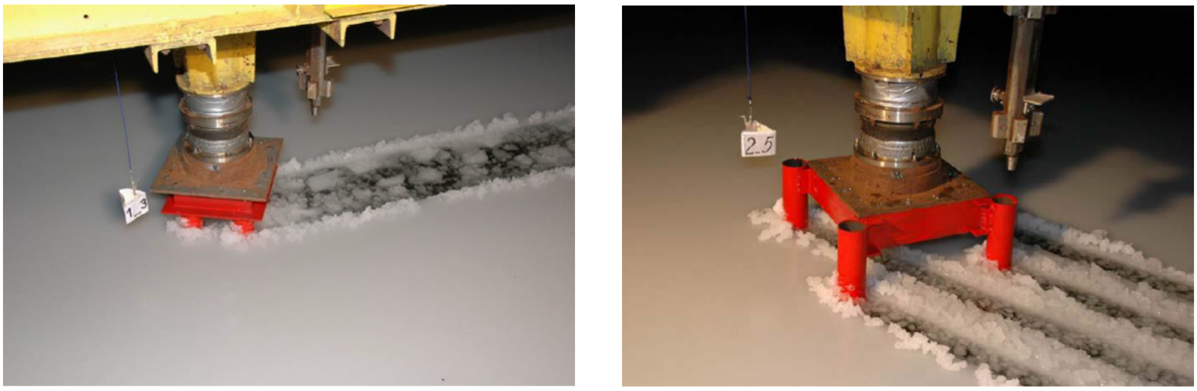

(a) L/D ratio of 2.5, ice drift direction 30°.

(b) L/D ratio of 6.0, ice drift direction 30°.

Figure 2.13: Experiments performed by Karulin and Karulina (2014).

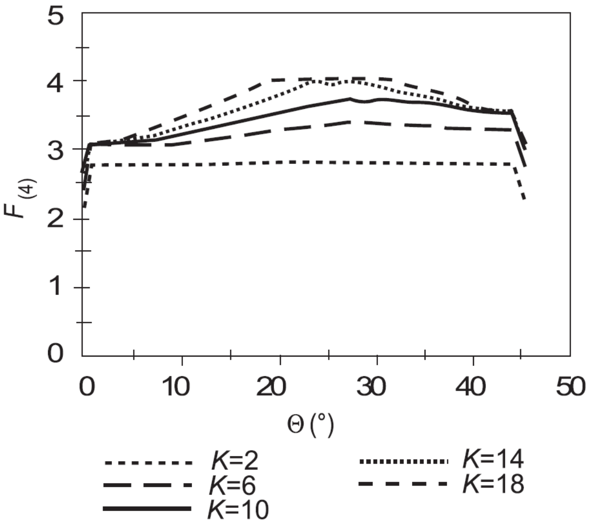

Figure 2.14: The ratio of the force on four legs, $F_{(4)}$ versus the force on one leg as a function of the ratio (K) of the distance between the centers to the diameter of the legs and the indentation direction (θ) (Takeuchi et al., 1993).

of actions (Løset et al., 2006). Nawata et al. (1986) performed laboratory experiments with a four-legged, rectangular in-plane model in which it showed that if the ice motion is parallel to the front legs, then the actions on the back legs do not exceed 6-7% of the actions on the front legs. If the ice is moving in the direction of the structure's diagonal, then the ice actions on the sheltered leg were about 35% of the front leg. Takeuchi et al. (1993) and Kato et al. (1994) have investigated the effect of sheltering. These investigations found the factor $F_{(i)} = f(K,\theta)/F_{m1}$, which is the ratio of actions on the whole structure $f(K,\theta)$ over the force on a single leg F_{m1}. It takes into account the i-number of legs, the ratio (K) the distance between the centres to the diameter of the legs (L/D) and the intrusion angle (θ). The results from Takeuchi et al. (1993) for a four-legged structure are given in Figure 2.14. For (K) => 18 a lack of sheltering is visible for angles (θ) in the range 20-33°. For (K) =< 2 the maximum total action is only (2.6-2.7) times the force on one leg. These results will differ for a vertical or conical sided structure. These results are a bit higher than the ones from Shkhinek et al. (2009), which stated that the 2.8 will be the maximum until K=10. Kato et al. (1994) conducted model tests with two structures having four conical legs spaced $K = 2.6$ at the waterline. One structure had downward bending cones, and the other had upward bending cones. The conclusions from this research were that the total ice action was maximal for an indentation angle of 30 °. Furthermore, the total ice action was the same for downward and upward bending but that there was a factor 2 difference in the normalised ice action, the downward bending was twice the upward bending normalised. The ice force for an independent downward cone was half the ice force for an independent upward cone. Thus the total force is approximately the same. This could be attributed to the ice jamming, which occurred for the downward bending cone (Kato et al., 1994).

Figure 2.15: Ice splitting during model tests (Hoving et al., 2013).

Another effect that leads to a decrease in ice action due to leg interaction is ice splitting, which can be seen in Figure 2.15 during model experiments. Splitting failure occurs when the action required to split the ice at an angle α is lower than the action required to crush the ice within the range of the angle α. Thus splitting will occur at the angle for which the lowest energy is required to fail the ice against the structure (van den Berg, 2013). This may explain the relation from Timco and Pratte (1985), where the load direction is depending on the leg spacing. When the legs are close, Q/D<6, the direction of the load is under an angle θ_a. Which could be the results of ice splitting, which reduces the load on the α-side and thus introducing an angle θ_a on the principal load direction. The splitting force can be calculated with Equation 2.18 and the angle α can be calculated with Equation 2.19. Where σ_c is the ice strength, L_{split} is the splitting length, h is the ice thickness, D_{leg} is the diameter of the leg and L_{CTC} is the centre to centre distance between the two legs. The area inside the red triangle is the area susceptible to splitting failure, which can be seen in Figure 2.16. In van den Berg (2013) these Equations are used to model the ice force. With these equations the model is more accurate in amplitude and direction of mean ice force when compared with test data from Hoving et al. (2013). It is unknown whether this equation is also valid for real scale scenarios.

$$F_{\text{split}} = \frac{1}{105}\sigma_c L_{\text{split}}\, h \tag{2.18}$$

$$\alpha = \arcsin\left(\frac{D_{\text{leg}}}{2L_{CTC}}\right) \tag{2.19}$$

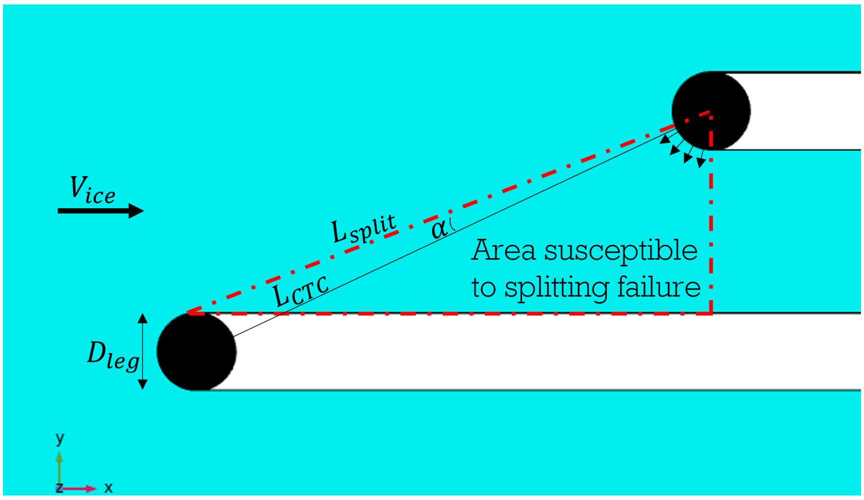

Figure 2.16: Overview of the ice splitting parameters.

2.3.2. Non-simultaneous failure effects

The probability that the maximum of actions will occur simultaneously on all the legs is moderate. This is also known as the non-simultaneous failure effect. This has been researched full scale by Johnston et al. (2000) and model scale by Huang et al. (2013a;2013b), Kato et al. (1994) and Takeuchi et al. (1993). The full-scale test by Johnston et al. (2000) was performed on a pair of legs of a Chinese JZ-20 platform. The investigation in the data showed that one leg may or may not be synchronised with that of the adjacent leg. Furthermore, it showed that the most conservative evaluation of the non-simultaneous failure influence on the ice actions is about 0.85 – 0.9. This data is in line with the data obtained from laboratory experiments by Wessels and Jochmann (1990). The total ice action on the entire platform was only 50% higher than the action on one of the legs. Takeuchi et al. (1993) obtained a non-simultaneous failure coefficient of approximately 0.8. Huang et al. (2013a) quantified this non-simultaneous effect by defining a non-simultaneous factor η as the ratio of the maximum total ice load with the sum of maximum pile ice loads, see Equation 2.20. Where F_{i-Max} is the maximum ice load on the i-th pile, n is the number of piles, and $F_T - Max$ is the total maximum ice load. The phasing effect is also taken into account so that the F_{i-Max} value should be the peak value whose occurring time point is the nearest to the time point corresponding to $F_T - Max$. The results are shown in Figure 2.17 for a range of ice velocities, V. The different tests have increasing structural stiffness values, with F1 being the least stiff and F3 the stiffest. As can be seen in Figure 2.17 there is a narrow velocity range to high non-simultaneous factor values. These high values beyond 0.95 indicate that the non-simultaneous effect can almost be ignored. This narrow band can be categorised into the "ductile-to-brittle" stage for each test set-up Huang et al. (2013b). Kato et al. (1994) also mentioned the importance of effects of non-simultaneous failure in order to estimate realistic ice forces. That without this parameter, the ice forces would be overestimated. According to the ISO (2019) 19906 standard the value for the effects of non-simultaneous failure, in absence of test data, is $k_n = 0,9$. This matches above mentioned research.

$$\eta = F_{T-Max}\left[\sum_{i=1,\cdots,n}^{n} F_{i-Max}\right]^{-1} \tag{2.20}$$

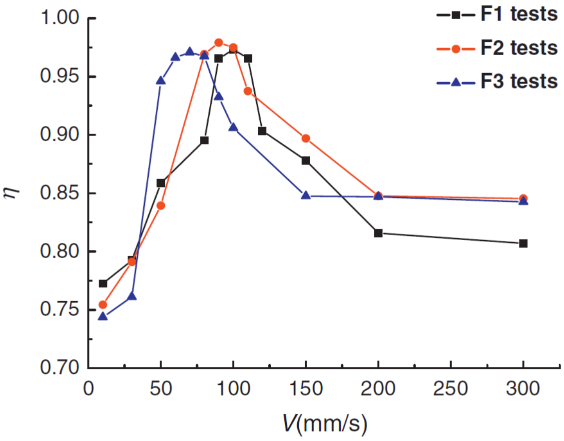

Figure 2.17: Non-simultaneous factor, η, against ice velocity, V, for different structural stiffness values (Huang et al., 2013b).

2.4. Ice jamming

A potential risk of multi-legged foundations is the accumulation of rubble between the legs, which is called ice jamming. The jammed ice often has sufficient strength and is not easy to clear away from the legs. The legs and the jammed ice may then act as a single structural unit (Palmer et al., 2015). Two different types of jams can be distinguished, a front jam and an internal jam. When structures are not designed for such jams, the consequences can be severe. E.g. Bohai No. 2 platform in the Bohai Sea, which had an internal ice jam that caused the local structure to fail and eventually, the whole structure collapsed, see Figure 2.18 (Xu et al., 2009). First, the formation of ice jams is discussed in Section 2.4.1. Then related phenomena in other contexts where solid particles flow through gaps will be discussed in Section 2.4.2. At last, situations from the field and model tests will be looked at in Section 2.4.3.

Figure 2.18: The internal ice jam of Bohai No.2, which eventually was pushed over by sea ice. (Xu et al., 2009)

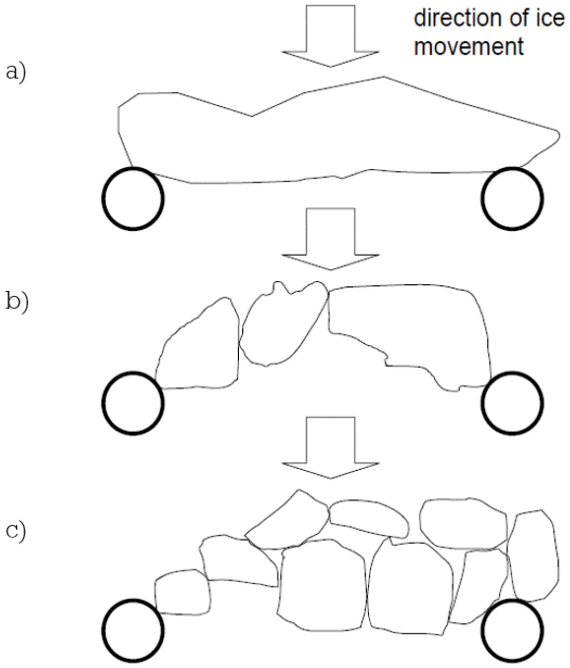

Figure 2.19: Three distinct frontal jamming modes by Palmer et al. (2015).

2.4.1. Formation of Ice Jams

The formation of ice jams in the field of offshore engineering has not been researched that much. In the last decades, more research has been done in the field of river ice jams. An ice jam can occur when the broken ice is not cleared in time after an ice action event on the structure. This ice rubble can accumulate and initiate an ice jam. According to Palmer et al. (2015) there are three types of front jamming modes, see Figure 2.19. If the fragments are larger than the gap, a single fragment can bridge between the legs (2.19a). The current can carry other smaller fragments against the first one, and a jam starts to accumulate. If the fragments are smaller than the gap, the gap can be bridged by a small number of fragments. These fragments then form an arch. The stability of this arch will depend on the current, waves, friction between fragments and friction between fragments and the platform legs (2.19b). If the fragments are much smaller than the gap, they may still form an arch and initiate an ice jam (2.19c), although less likely. The internal friction between the fragments has become more critical to the stability of the arch, and the shape of the fragments is more significant than the other jams. The ice and current force on the fragments increases the horizontal stresses and increase the arch's stability.

The internal jam is visible at the Bohai No.2 structure see Figure 2.18. Ice starts to accumulate in between legs, risers or conductors. Due to limited ice clearance, the accumulation can reach several meters. A cold environment will also accelerate the growth of the ice jam by adding snow or slush. The cold air helps to refreeze everything, grow the ice and increase strength.

Cones around the waterline will impact the formation of ice jams. During the experiments from Kato et al. (1994) not a single jam occurred with upward bending cones, while for downward bending cones, it did every time. This strategy has been applied to multi-leg platforms in the Bohai Sea and on the multi-pier Confederation Bridge in Canada. On the one hand, if cones are present, the ice will break in bending, and those fragments are larger than those formed by crushing, which would lead to making ice jamming more likely. On the other hand, the flow of ice around a structure appears to be smoother if cones are present, and this tends to be a positive factor that reduces the chance of the formation of an ice jam (Palmer et al., 2015).

2.4.2. Related phenomena

A lot more research has been performed into the formation of river ice jams. Beltaos (1995) goes into the formation and breakup of river ice jams. The fragments in river ice jams are usually quite small, far smaller than the river's breadth. Not much information is given about the initiation of the jam, but sharp turns, narrowing, and the presence of structures play a part. A river ice jam significantly reduces the flow and can cause flooding. In the prevention of river ice jam flooding ice control structures (ICS) can be placed in the river. These structures are typically vertical sided cylindrical piers placed at equal spacing perpendicular to flow direction, which bear a resemblance to multi-legged structures. Tuthill and Lever (2006) describe the design of such structures. An important note regarding ICS is that an ice jam is desirable, whereas in multi-legged structures, it is not. The Q/w ratio is an important threshold value for the performance of ICS. A laboratory study by Calkins and Ashton (1975) showed that for surface concentrations of greater than about 30 %, moving ice will arch between piers when the ratio Q/w is less than about 4. Model and field tests with upward-sloping ICS were performed by Lever et al. (1997), and they created ice jams when Q/w was less than about 5/6. The average diameter of the breakup ice floes was about 3/4 times the ice thickness. Thus, the maximum ICS gap which can be used is about 15 times the minimum ice thickness that poses an ice jam threat.

An analogy with masonry can also be made. The stability of a masonry arch depends on the form of the arch as a whole, the individual components and the friction between them. The strength of the stone has little importance because the stresses are much lower than the strength of the stone. This conclusion can be applied to a naturally formed ice arch between the legs of a multi-legged structure. For example, an ice arch that spans 15 m consisting of 1 m cubes of 900 kg/m^3 and is loaded by a 1 m/s current the hydrodynamic force on the ice arch is 1.8 kN/m, the thrust in the arch is roughly 25 kN and the corresponding mean stress is 25 kPa. Even if non-uniformity and increased loading increase this stress by a factor of 10, the resulting 0.25 MPa is far lower than the compressive strength of ice. However, if an ice jam of fragments form an arch, a continuous ice sheet might drift against this arch, resulting in forces larger than the compressive strength (Palmer et al., 2015).

2.4.3. Multi-legged ice jams

Ice jams have been observed on full scale and model scale multi-legged structures. The JZ-20 platform in the Bohai Sea has jammed between the legs of the platform, and the jam accumulated to a thickness of 4 - 7 m (Fan and Jin, 1990), see Figure 2.20a for the platform. The corresponding Q/D ratio was roughly 3.3. The JZ9-3 WHPA jacket structure encountered an internal ice jam in between the conductors see Figure 2.21. This jam was mainly induced due to the narrow distance between the conductors. Because of that, the natural environmental driving forces were small to clear the accumulated ice rubble. Also, a frontal jam is visible in Figure 4.4b against the conductors. These jams threaten structural performance and safety. Another risk is that the internal jam grows to the deck and excites a force from under the deck. Another structure in the Bohai Sea, the JZ20-2 MNW multi-leg platform, encountered a frontal ice jam, see Figure 2.22. This structure has upward bending cones and conductors. The jam consists of small broken ice pieces which are not yet frozen together. The result is that the structural response is less than without a jam. Because the loose ice blocks absorb the energy input due to ice action, however, once the front jam is fully frozen, the structural response could be more severe.

Karulin and Karulina (2014) performed model experiments with a semi-submersible (6 legs) and ice jamming led to an increase in ice load, see Figure 2.23. With a Q/D ratio of 3.9. The ice concentration was 5/10. During model experiments by Kato et al. (1994) ice jamming was observed for the downward bending cone and not for the upward bending cone. The Q/D ratio was 1.7 at the waterline. Experiments with a model scale jack-up vessel with a Q/D ratio of 6.1 were performed by Hoving et al. (2013). During tests with a 6/10 ice coverage, ice jammed between the front legs, as can be seen in Figure 2.20b.

Politko and Kantardgi (2017) performed numerical calculations to quantify the effect of jammed ice on the total ice load. From their numerical analysis, the ice load increased by no more than 10% for a four-legged structure and for a three-legged structure, it did not show any significant increase in ice action. Shkhinek et al. (2009) also obtained a numerical solution for ice field interactions with a 4-legged structure. However, it did not show an increase in ice action. It should be noted that here the properties of the jammed ice were modelled to have lower strength than the intact ice by a factor of 0.5 and 0.7. A test run where the jam was stronger with a factor of 1.5 resulted in large oscillations in the load time series. Unfortunately, these results were discarded and not shown.

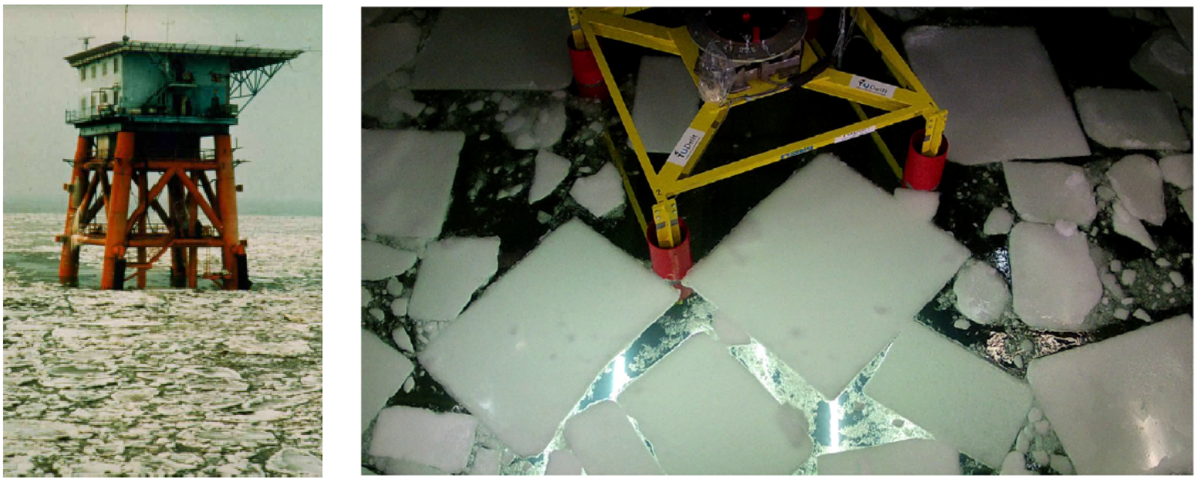

(a) JZ-20 platform (Johnston et al., 2000).

(b) Ice tank test with a four-legged structure (Hoving et al., 2013).

Figure 2.20: Left: JZ-20 platform in the Bohai Sea (Johnston et al., 2000). Right: Ice tank tests with four-legged structure. The picture is from van den Berg et al. (2018), experiments performed by Hoving et al. (2013).

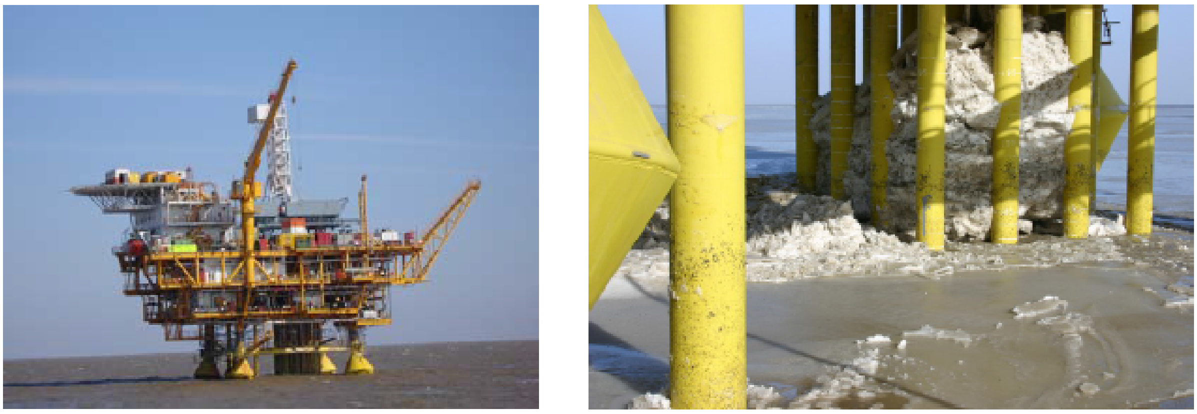

(a) The JZ9-3 WHPA jacket structure.

(b) Internal ice jam in between the conductors.

Figure 2.21: The JZ9-3 WHPA jacket structure with an internal ice jam in between the conductors Xu et al. (2009).

(a) The JZ20-2 MNW multi-legged platform.

(b) Frontal ice jam in front of the JZ20-2 platform

Figure 2.22: Frontal ice jam in front of the JZ20-2 MNW multi-legged platform Xu et al. (2009).

(a) Frontal ice jam of semi-submersible, $Q/w \approx 3.9$.

(b) Frontal and central ice jam of semi-submersible.

Figure 2.23: Frontal and central ice jam of semi-submersible, experiment by Karulin and Karulina (2014).

2.5. Failure modes

Materials can fail in different modes, e.g. compressive, tensile, flexural, etc. The developed pressure distribution will determine the mode of failure among ice strength level, thickness, velocity, size and structural shape. In previous sections, the different ice parameters and structural shapes have been discussed. This section will focus on the different failure modes and their impact on the ice-structure interaction. These failure modes can replace each other during the same indentation event depending on the local conditions of interaction. Sanderson (1988) classified the following failure types: creep, radial & circumferential cracking, buckling, spalling and crushing, see Figure 2.24 for a graphic representation of the failure modes and the failure mode map. The latter shows that the failure mode is a function of ice velocity and the aspect ratio (structure width, or diameter *d* to ice thickness *h*).

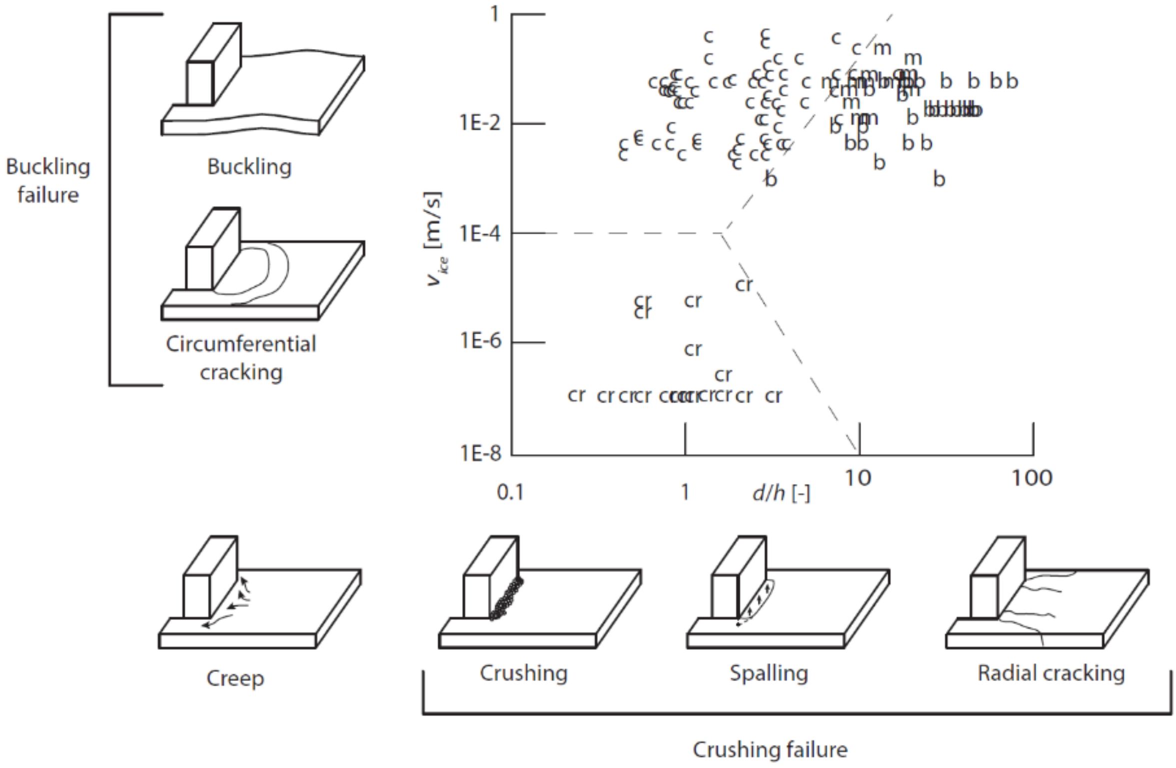

Figure 2.24: Graphical representation of the failure modes and failure mode map by Hendrikse (2017) using data from Timco (1991). The failure modes are plotted on a map with on the vertical axes the ice speed, V_{ice}, and on the horizontal axes the aspect ratio (structure width, or diameter, *d* to ice thickness *h*). Legend: cr = creep; c = crushing failure (crushing, crushing with spalling, and crushing with radial cracking); b = buckling failure; m = mixed crushing and buckling failure.

2.5.1. Creep

As can be seen from Figure 2.24 the creep failure mode occurs at low ice speed velocities and low aspect ratios. This ductile deformation develops continuously, and no cracks form in the ice. The ice deforms in a plastic manner to flow around the structure see Figure 2.24 for a sketch. The contact area between the ice and structure is almost perfect, resulting in a uniform pressure along the width of the structure.

This leads to a gradual increase in ice action. After it reaches its maximum it decreases slowly to a steady-state (Hendrikse, 2017), see Figure 2.25 for a graph of the global ice load over time. The maximum velocity at which creep occurs is the transition velocity which is estimated at 1 mm/s (Schulson and Duval, 2009). In Section 2.1.5 this transition was mentioned as the ductile to brittle transition. Around this velocity, the maximum ice load can be expected for low aspect ratios because otherwise buckling will occur, which is also visible in the failure mode map. Creep will mainly occur for ice with decreasing velocity or during thermal expansion (Willems, 2016).

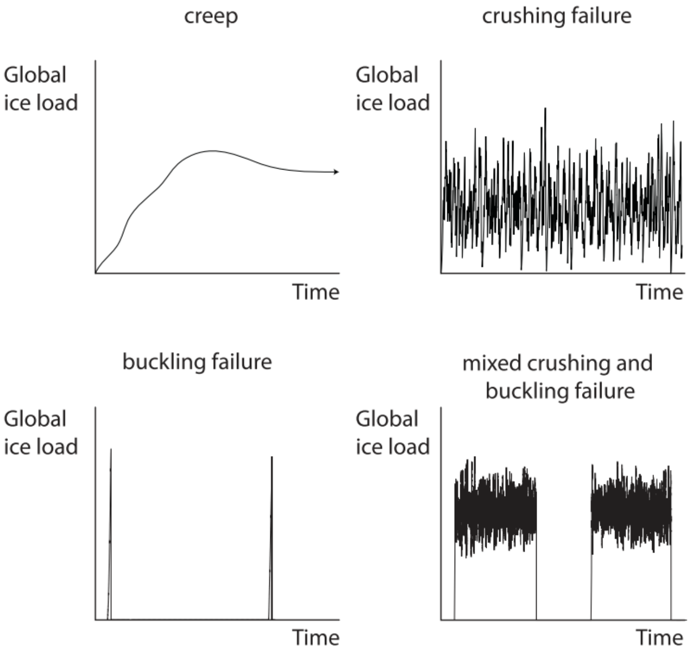

Figure 2.25: Time traces of the different failure modes showing the characteristic of each mode from Hendrikse (2017). These graphs are not to scale.

2.5.2. Buckling

Buckling failure consist of buckling and circumferential cracking. See Figure 2.24 for the sketches. Buckling failure is defined by out-of-plane bending failure due to compressive loading, which can develop for low and high ice velocities and occurs for high aspect ratios (Hendrikse, 2017). The bending stress exceeds the flexural strength resulting in the buckling failure (Owen, 2017). The flexural stiffness of an ice sheet scales with h^3, thus buckling failure mainly happens at high aspect ratios (Willems, 2016), which is illustrated in the failure mode map. Vertical loads, due to a conical shape at the waterline or ice rubble, can produce a failure mode with a similar outcome, bending failure (Hendrikse, 2017). Circumferential cracking occurs at the front of flexural strength exceedance in the ice sheet (Willems, 2016).

The global ice action over time for buckling is displayed in Figure 2.25. The buckling event consists of three stages: first, contact between the structure and the ice sheet, then the pressure increases until the critical buckling load is reached. A global failure along the line of the flexural strength exceedance of the ice sheet occurs, which causes a loss of contact between the intact ice sheet and the structure, resulting in a sharp drop in the global ice load. In between these events, the global ice load is almost zero (Owen, 2017).

2.5.3. Crushing

At ice velocities higher than the transition velocity, the ice will fail in a brittle manner. Instead of the steady and flowing ductile manner, the brittle manner is more violent. Due to the higher ice velocity, the pressure is not uniformly along the contact area. High local pressure peaks pulverise the ice locally and, in return, create other pressure peaks. Along with the pulverising crushing, spalling and radial cracking can occur Willems (2016). See Figure 2.24 for the sketches of these failure modes. The generation of spalls and flakes are caused by cleavage cracks propagating to the free surface. This creates a wedge shape in front of the ice when looking from the side (Hendrikse, 2017). Or another way of describing them is that they are formed by out-of-plane tensile and shear failure in the columnar ice. Resulting in the extrusion of disc shaped plates at the top and bottom of the ice (Willems, 2016). This type of failure happens for aspect ratios greater than one (Hendrikse, 2017). Radial cracks are caused by in-plane tensile and shear failure and are formed in the direction of the loading, thus perpendicular to the contact area. For a rectangular shape, this means that the radial cracks from the direction of the ice velocity. For cylindrical shapes, these cracks will form normal to the structure's outer diameter. Radial cracks occur at relatively high aspect ratios (Willems, 2016).

The global ice action over time for crushing is displayed in Figure 2.25. This load is found to be quasi-random around a mean value due to the randomness in the location of high-pressure zones in the contact area, which leads to a stochastic local failure of ice.

2.5.4. Mixed crushing and buckling

In Figure 2.24 it looks like the failure modes have distinct regions in which they occur. The data is from model-scale experiments by Timco (1991), and the full-scale data shows to be more scattered around this failure mode map (Hendrikse, 2017). Thus transition areas exist in which crushing and buckling both occur.

The global ice action over time for crushing and buckling is also displayed in Figure 2.25 as can be seen it consist of behaviour from crushing and buckling combined. Typically crushing failure occurs, then a buckling failure occurs, resulting in the loss of contact with the intact ice sheet. Resulting in almost zero loads, and then the contact is restored, and crushing failure continues.

2.6. Ice-induced vibrations

The failure modes mentioned above are only fully correct if the associated structure is rigid. Most support structures are compliant or have some flexibility, and thus the dynamic phenomena do have to be taken into account. Ice-induced vibrations are observed for practically all vertical and near-vertical fixed structures exposed to moving ice. The severity depends on structural properties and ice conditions. It increases increasing flexibility of the structure. Ice-induced vibrations are observed when ice fails predominantly by crushing (ISO, 2019) 19906. Creep failure can be disregarded due to the relative low ice velocity and mostly plastic deformations. The changes in global loading are not of a significant magnitude to cause severe vibrations (Owen, 2017). Buckling failure is also disregarded because its vibrations are small in amplitude, despite its rapid changes in the magnitude of global ice loading (Hendrikse, 2017). This section is largely based on the work by Hendrikse (2017).

These ice-induced vibrations occur mainly in the crushing failure mode. Thus a low aspect ratio or relative thick ice is needed together with an ice velocity above transition velocity. Three distinct loading regimes are observed: intermittent crushing (ICR), frequency lock-in (FLI) and continuous brittle crushing (CBR). These regimes are visually presented in Figure 2.26 as a function of ice velocity. The difference between a rigid and flexible structure is shown. Note that these three regimes do not necessarily occur for each flexible structure, but for the lowest ice velocities, intermittent crushing is observed, followed by frequency lock-in and for the highest ice velocities, continuous brittle crushing. ICR is important because it gives the highest global loads, and FLI gives the largest amplitudes of structural oscillation. These regimes will be further elaborated upon, but for a more in-depth explanation, consult the work of Hendrikse (2017).

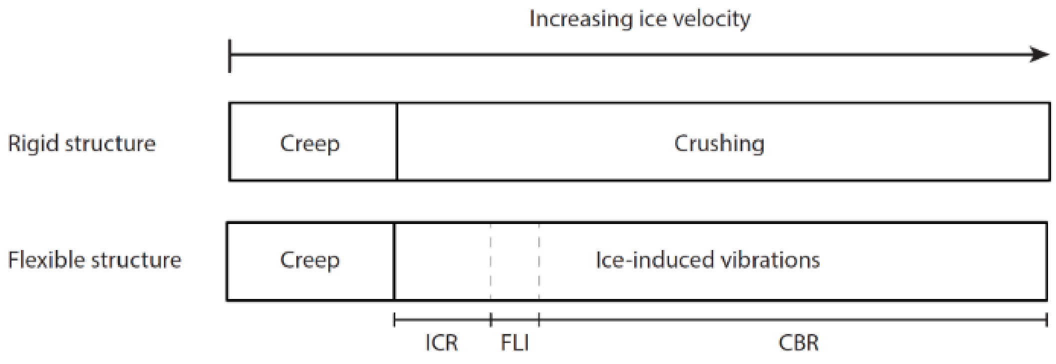

Figure 2.26: Visualization of ice failure modes with respect to ice velocity for rigid and flexible structures from Hendrikse (2017).

2.6.1. Intermittent crushing

Intermittent crushing occurs at relative low ice velocities for a relatively flexible structure see Figure 2.27 for a time trace of the structural displacement and global ice load. This regime is distinguished by a saw-tooth pattern in structural displacement and global ice load. Its frequency is approximately constant for a certain structure in non-varying ice conditions and increases with ice velocity until FLI or CBR become dominant. Figure 2.28 shows the global load, contact area and local pressures for an intermittent crushing event. The

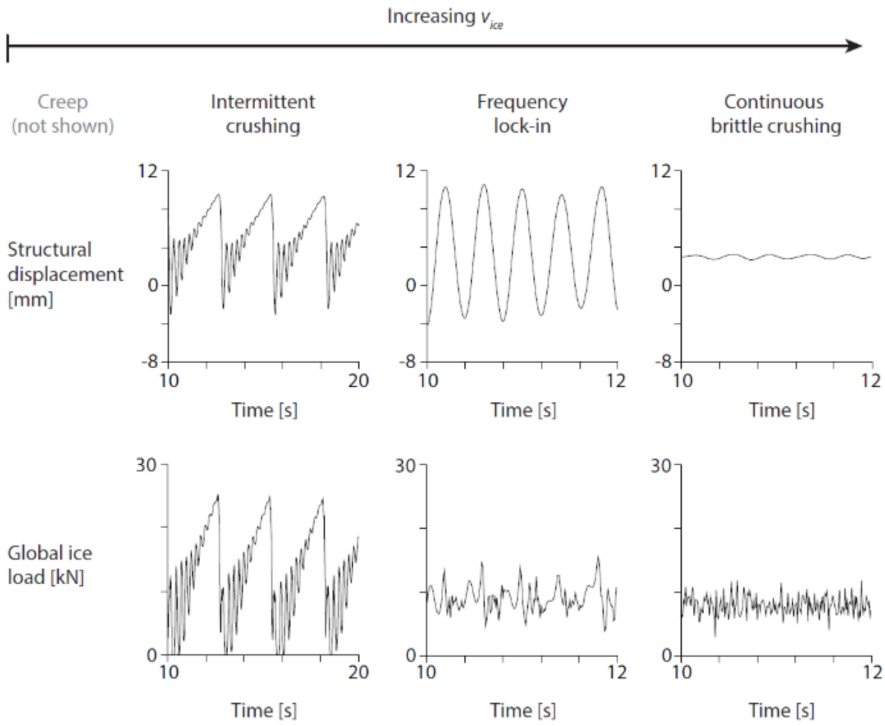

Figure 2.27: Graphical visualisation of the three ice-induced vibration regimes with structural displacement and global ice load as a function of time. These values are computed from numerical simulations and should be regarded as relative and not actual (Hendrikse, 2017).

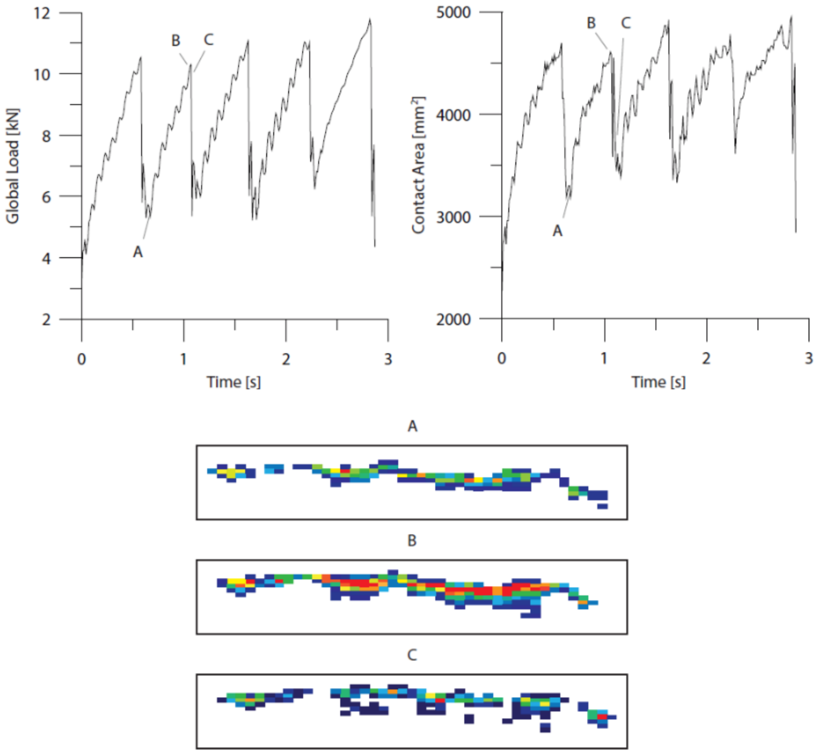

Figure 2.28: Time trace of global ice load and contact area during an intermittent crushing event, with corresponding pressure distribution over the contact area. From Hendrikse (2017) according to the experiments from Maatanen et al. (2012). Legend for pressure color scheme: blue = low pressure; red = high pressure.

letters A, B and C denote different moments in time. There is a loading and an unloading phase. During the loading phase, the ice behaves in a ductile behaviour, which leads to an increase in contact area (A to B). Although the ice velocity is above transition velocity, the relative velocity is below it. The relative velocity is the ice velocity minus the structural velocity. The contact area and global loading increase in an oscillation motion. Until the maximum load is reached and the unloading phase begins (instant B). The high-pressure zones lead to local brittle failure. This triggers a chain reaction. As one high-pressure zone fails, another high-pressure zone will arise, which then also fails, continuing the reaction (Owen, 2017). This results in a structural velocity opposite to the ice velocity, and its relaxation vibration follows the structure's natural frequency (B-C). Due to damping and interaction with the ice, the vibrations decay during the new loading cycle (Willems, 2016).

2.6.2. Frequency lock-in

Frequency lock-in occurs over a range of ice velocities for structures with low damping and low natural frequencies, see Figure 2.27 for a time trace of the structural displacement and global ice load. A sinusoidal motion characterises this regime in the structural displacement. The ice failure frequency will adapt to one of the lowest natural frequencies of the structure. As a result, the structural displacement has an oscillation movement which can be amplified significantly due to resonant behaviour. Particularly if there is low structural and foundation damping (ISO, 2019). The global ice load follows a quasi-random pattern. Peaks occur in the global ice load when the relative velocity is low.

A nearly linear relation between ice velocity and the maximum structural velocity per frequency lock-in cycle is found. The relation is described by Equation 2.21. Where $\dot{u}_{\max}$ is the maximum structural velocity during a frequency lock-in cycle, β is an empirical coefficient which is mainly in the range 1.0 to 1.5 but not limited to it as frequency lock-in has been observed outside this range and v_{ice} is the ice velocity. The physical mechanism which causes this relation is not clear Hendrikse (2017).

$$\dot{u}_{\max} = \beta v_{\text{ice}} \qquad [m/s] \tag{2.21}$$

2.6.3. Continuous brittle crushing

For relative high ice velocities, the regime continuous brittle crushing is dominant and is observed for all types of flexural structures. See Figure 2.27 for the time traces of the structural displacement and global ice load. This regime is characterised by a seemingly random global ice load that fluctuates around a constant mean value. Due to the high ice and relative velocity, there is only brittle behaviour. The loading is of an aperiodic nature, resulting in an aperiodic structural response. The amplitude of the structural response is relatively small and much smaller compared to the other regimes ICR and FLI.

3

Conclusion literature study

Ice interaction with a multi-legged support structure is a complex phenomenon. In the past years, much research has been done into ice-induced vibrations, especially for mono-piles and ice actions on multi-legged support structures. The effects of an ice jam in between multi-legged sub-structures are relatively unknown. The ISO (2019) 19906 standard gives Equation 2.12 as guidance for the calculation of the global limit stress. However, there is much uncertainty regarding sheltering, non-simultaneous failure and jamming. The use of models and laboratory tests can diminish this uncertainty. The following key points are the most important takeaways from the literature study:

- Existing models to model the keel of ice ridges can be used as guidance for modelling ice jams. Several discrete element methods have been used, where the ice rubble is modelled as an assembly of discrete ice particles. Although it is computationally expensive. Another option is to use continuum models such as Mohr-Coulomb or Drucker-Prager, which is computational more friendly. However, choosing the right cohesion and friction angle will be key in generating meaningful data.
- Limit stress will be the design scenario that has to be taken into account.
- The global ice load on multi-legged sub-structures is generally less than the number of legs multiplied with the force on an isolated leg.
- Pile interaction will occur when the pile spacing is small enough that the piles cause interference. For piles in a line perpendicular to the incoming ice, the interaction is neglectable for spacing of Q/D greater than 6. The pile spacing is thus an important design parameter to control the loads.
- The effect of sheltering can reduce the ice loads significantly. Depending on the type of sub-structure and the number of legs, the total ice load can differ a lot. The total ice load is not simply a multiplication of the i-number of legs with the load on one leg. The indentation angle, θ, determines whether legs will align or face undisturbed ice. For a four-legged sub-structure, the maximum load occurs in the range of 20-35 degrees.
- The effect of non-simultaneous failure depends on the ice velocity, and in worst-case scenarios, this coefficient approaches 1. While for more favourable situations, the reduction can be significant with a coefficient of roughly 0.8.
- Internal and frontal ice jams can lead to severe damage if not adequately designed for.
- Although most ice jams occurs for structures with a Q/D ratio less than 4. Ice jams may still occur when this gap is more significant, even with small ice fragments. A high surface concentration will contribute significantly to this.
- Upward bending cones around the waterline can help to stay jammed free. They break the ice in larger fragments which is negative but also increases the flow around the structure, reducing the likelihood of arch forming.

- Numerical models and experiments have to conclude whether the total global ice load will increase due to an ice jam.

The first research question can now be answered and was as follows:

"How and when does an ice jam originate based upon literature?"

The formation of an ice jam between the legs of a multi-legged structure is a complex phenomenon. The initiation and stability are governed by the fragments' shape, internal strength, the interface and friction strength between the fragments, the surface concentration, and the gap between the legs. Two types of ice jams can be distinguished, frontal and internal jam. From field observations, numerous jams are initiated due to connectors/risers, decreasing the natural driving forces resulting in an accumulation of ice rubble. The clearing distance between the legs is an important parameter, and most jams occur for structures with a Q/D ratio of less than 4, following the ISO standards.

3.1. List of requirements

Following the conclusions from the previous section, a list of requirements for the model is made, which can be used to investigate the main research question. However, not all requirements are equal. This list can be split into "must-have" and "nice-to-have". The "must-haves" are essential for producing a model which can be used to generate meaningful/valuable data. The resulting model can approximate the global response and forces. The "nice-to-have" requirements are, as the name spoils, nice to have. This list will bring the model from a global approximation to a more in-depth local quantification. Things to keep in mind are the complexity, feasibility and required computational power of the model.

Must have:

- A range of ice velocities
- A frontal and internal ice jam
- Contact modelling between the jam and structure
- A continuum model for the ice jam
- A known offshore jacket support structure
- A model to calculate the global ice load

Nice to have:

- A range of ice thicknesses for the jams
- Variety in leg spacing
- Simulation range of 100/200 seconds to capture the vibrations
- A continuum ice model where its properties are based on crystallography, temperature, porosity and salinity.

4

Modelling methodology

In this chapter, the model setup is explained by first explaining the individual parts and then how they interact with each other, see Section 4.1. Then the different scenarios are described in Section 4.2. At last, the simulation matrix is explained in Section 4.3.

4.1. Model setup

The model is consists of two main parts, the phenomenological model from Hendrikse and Nord (2019) and the COMSOL Multiphysics simulation software. In the orientation phase, it is concluded that COMSOL Multiphysics will be the vehicle, and the ice model will be called at every time step and iteration from within COMSOL Multiphysics. First, the phenomenological model is explained and then all taken steps in COMSOL Multiphysics are discussed.

4.1.1. Ice model

The phenomenological model from Hendrikse (2017) is used to calculate the local-global ice load on the structure's legs. The full explanation and origination of this model can be read in his work. In this section, a brief overview of the mathematical description and definition of input parameters of the model are given. This section is based on Hendrikse and Nord (2019). In which a simplified version of the model is published, which can be found on Mendeley Data. The model is one-dimensional and simulates the global ice load on a structure in the ice drift direction. The ice edge is modelled as N elements to capture the full range of ice loads, i.e. the different ice mechanics, ductile, transitional and brittle deformation and the different failure modes. Each element is modelled by a non-linear and linear spring and dashpot to capture the elastic, delayed-elastic and viscous deformation, see Figure 4.1. The initial position of the elements is obtained from Equation 4.1. Where $u_{i,j}$ is the position of j-th node of i-th element, these nodes can be seen in Figure 4.1. Which are obtained by offsetting $u_{s,0}$, which is the initial position of the structure, with a uniform distributed value between zero and the summation of r_{max} and $v_{ice}t_f$. Where r_{max} is the maximum offset of an element with respect to the structure, v_{ice} is the ice drift speed, and t_f is the time between initial contact and failure for an individual ice element. $v_{ice}t_f$ is added to ensure that the initial distribution of elements is similar to the distribution occurring during the interaction. t_f can be obtained by solving the equations of motion for a single element, assuming a non-moving structure, Equations 4.5 - 4.7, using $N = 1$, $u_{i,1} = u_s = 0$ and $u_{i,2}(t = t_f) = \delta_f$.

$$u_{i,1} = u_{i,2} = u_{i,3} = u_{s,0} - \mathrm{U}\left(0, r_{max} + v_{ice}t_f\right) \qquad [m] \qquad (4.1)$$

Each element propagates with the ice drift speed, $v_{ice}(t)$, until contact is established between an element and the structure. Then the local deformation and failure behaviour of the ice is modelled by the combination of non-linear and linear springs and dampers, see Figure 4.1.

The non-linear front spring, in between nodes 1 and 2, with stiffness K_2 captures the local elastic deformation of the ice and failure upon reaching a predefined critical local deformation. This spring cannot pass on a tensile force nor can it exceed its critical load, see Equations 4.2 - 4.3 for the definitions.

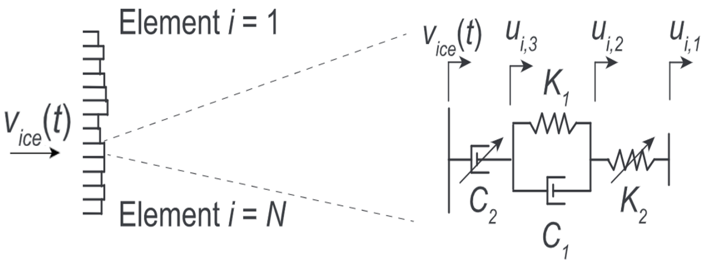

Figure 4.1: The ice edge is divided in N independent elements. Each element consists of a combination of (non-)linear springs and dashpots (Hendrikse and Nord, 2019).

$$K_2 = K_2 \text{ for } 0 < u_{i,2} - u_{i,1} \leq \delta_f \qquad [N/m] \tag{4.2}$$

$$K_2 = 0 \quad \text{else} \qquad [N/m] \tag{4.3}$$

The middle linear spring-dashpot combination with spring stiffness, K_1 and damping coefficient, C_1 captures the delayed-elastic deformation of the ice. The rear non-linear dashpot with damping coefficient, C_2 mimics the effects of the creep deformation. The dimensions of C_2 are $[N^3 m^{-1} s]$ and the load transferred by the dashpot is defined hereunder in Equation 4.4.

$$F_{C2} = \sqrt[3]{C_2 \left(v_{ice} - \dot{u}_{i,3}\right)} \qquad [N] \tag{4.4}$$

The equations of motion for a single element are described by Equations 4.5 - 4.7. Where $u_{i,j}$ are the three degrees of freedom of i-th ice element over the j-th nodes, 1-3. u_s is the structural displacement. This results in a velocity depended on deformation and failure behaviour for each element, see Figure 4.2. At low ice speeds, the viscous-elastic behaviour (mainly due to the rear non-linear dashpot) results in large deformation before reaching the critical deformation $K_2\delta_f$. At high ice speeds, the behaviour is elastic until the critical deformation $K_2\delta_f$ is reached. As can be seen from Figure 4.2 the type of deformation is dependent on the ice speed and the interaction with the structure.

$$u_{i,1} = \begin{cases} u_{i,2} & u_{i,1} < u_s \\ u_s & u_{i,1} \geq u_s \end{cases} \qquad [m] \tag{4.5}$$

$$\dot{u}_{i,2} = \frac{K_2}{C_1}\left(u_{i,1} - u_{i,2}\right) + \frac{K_1}{C_1}\left(u_{i,3} - u_{i,2}\right) + v_{ice} - \frac{1}{C_2}\left(K_2\left(u_{i,2} - u_{i,1}\right)\right)^3 \qquad [m/s] \tag{4.6}$$

$$\dot{u}_{i,3} = v_{ice} - \frac{1}{C_2}\left(K_2\left(u_{i,2} - u_{i,1}\right)\right)^3 \qquad [m/s] \tag{4.7}$$

The ice load on the structure can be calculated with Equation 4.8 where the global ice load is the summation over N elements of the individual ice load of each element, F_i. The Heaviside function indicates whether contact is established or not. In the MATLAB implementation, the Heaviside function is approximated by a hyperbolic tangent. When the critical deformation is reached for an element, this element is removed from the model, and a new one is generated based upon Equation 4.9. This equation looks similar to Equation 4.1 which initializes all the elements. Except for $v_{ice}t_f$, which is not used because the ice is interacting with the structure. Thus the distribution during interaction stays the same.

$$F_{ice}\left(u_s, t\right) = \sum_{i=1}^{N} F_i = \sum_{i=1}^{N} K_2\left(u_{i,2} - u_{i,1}\right) \mathrm{H}\left(u_{i,1} - u_s\right) \qquad [N] \tag{4.8}$$

$$u_{i,1} = u_{i,2} = u_{i,3} = u_{s,0} - \mathrm{U}\left(0, r_{\max}\right) \qquad [m] \tag{4.9}$$

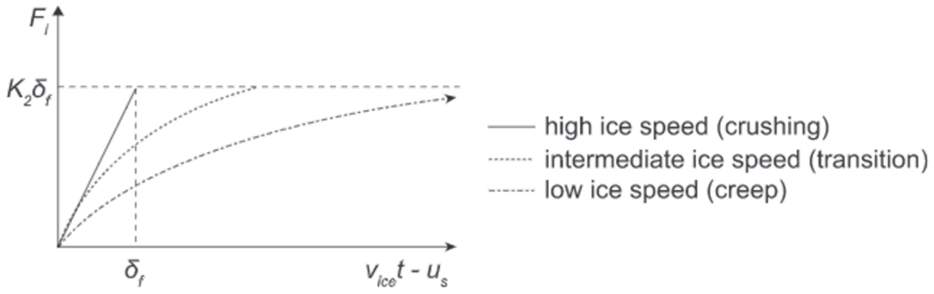

Figure 4.2: Local ice load transferred by an ice element versus the total deformation of an ice element, assuming constant ice speed and a rigid structure. At high ice speeds, the deformation grows approximately linearly until it equals the predefined local crushing deformation. At intermediate ice speeds, around the transition from ductile to brittle, local brittle failure develops after a total element deformation is reached, which exceeds the predefined critical deformation. At low ice speeds, brittle failure never occurs due to large ductile deformations (Hendrikse and Nord, 2019).

Input parameters

The Equations 4.1 - 4.9, are used to calculate the propagation, global ice load and failure of the ice field. However, seven input parameters still have to be defined: K_1, K_2, C_1, C_2, N, r_{max} and δ_f. Which are obtained based on measurements, hence it is a phenomenological model. These measurements are obtained from tests with a rigid structure. The resulting input parameters can then be used for simulations of a flexible structure in similar ice conditions. An example of the calculation of these parameters based on measurements can be found in Hendrikse et al. (2018).

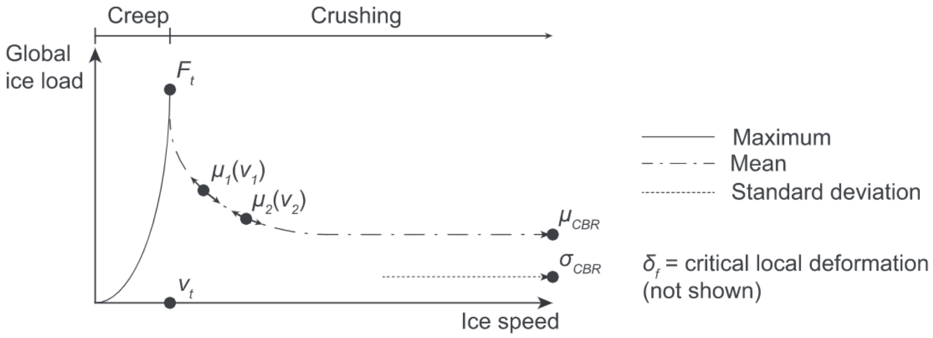

Figure 4.3: Trends in global ice load on a rigid structure with six well defined points, used to calibrate the model input parameters. The critical local deformation is not shown in this graph but that is the seventh point (Hendrikse and Nord, 2019).

The trends in global ice load on a rigid structure can be uniquely defined by six points indicated in Figure 4.3. These six points implicitly contain the effects of grain size, ice thickness, ice strength, temperature, porosity, etc. And can be obtained from measurements with rigid structures. The first point, V_t, is the transition velocity between creep and crushing. The second point, F_t, is the maximum global load that can develop for an ice speed equal to the transition velocity. The third and fourth points, μ_{CBR} and σ_{CBR}, are the mean global ice load and standard deviation of the global ice load for high ice speed, respectively. High ice speed is defined as significantly above V_t. The fifth and sixth points, $\mu(V_1)$ and $\mu(V_2)$, define the slope of the mean global ice load as a dependency of ice speed. The seventh data point, critical deformation for ice crushing at high ice speed, is defined separately because it relates more to local crushing at the ice-structure interface. A constant value is assumed due to difficulties obtaining a spectrum for this parameter. Tactile sensors are used to capture this deformation. However, in practice, load signals are short duration and show global low-frequency variations due to their natural variations in ice properties. Thus an average value for the critical deformation of a single element is used (Hendrikse et al., 2018). Five out of the seven input parameters can be calculated explicitly based on Equations 4.10 - 4.14. K_1 and $C1$ can be found iterative by solving the expected global ice load, Equation 4.8, by using the other parameters and assuming a non-moving structure. Resulting in solving Equations 4.15 and 4.16.

$$\delta_f = \delta_f \qquad [m] \qquad (4.10)$$

$$r_{\max} = \delta_f \left(\frac{F_t}{\mu_{cbr}} - 2 \right) \qquad [m] \qquad (4.11)$$

$$N = \frac{\left(\frac{2F_t}{3\mu_{cbr}} - 1 \right)}{\left(\frac{\sigma_{cbr}}{\mu_{cbr}} \right)^2} \qquad [-] \qquad (4.12)$$

$$K_2 = \frac{F_t}{\delta_f N} \qquad [N/m] \qquad (4.13)$$

$$C_2 = \frac{F_t^3}{N^3 v_{ice}} \qquad [N^3 s/m] \qquad (4.14)$$

$$\mu_1 (v_1) = \frac{F_t}{\delta_f} \frac{\int_0^{t_f(v_1)} u_{i,2}(t)\mathrm{d}t}{\frac{0.5 r_{\max}}{v_1} + t_f (v_1)} \qquad [N] \qquad (4.15)$$

$$\mu_2 (v_2) = \frac{F_l}{\delta_f} \frac{\int_0^{t_f(v_2)} u_{i,2}(t)\mathrm{d}t}{\frac{0.5 r_{\max}}{v_2} + t_f (v_2)} \qquad [N] \qquad (4.16)$$

For this model, the input parameters are calculated with confidential preprocessing tools from the TU Delft. These generate the ice input parameters for different scenarios and are used before every simulation. The following parameters are used as input for these tools: structural width, ice strength, and ice thickness.

4.1.2. Structural model

The structural model is based on the jacket support structure, which is designed for phase 1 of the OC4 project. This jacket was originally designed by Vemula et al. (2010). The turbine for which this jacket is designed is known as the NREL 5-MW baseline turbine described by Jonkman et al. (2009). Vorpahl et al. (2011) describes this jacket support structure in detail, and for this section, it will be the main reference. Some adjustments have been made in order to suit the jacket for ice loads. The results from the OC4 project are published in Popko et al. (2012) and these will be used to check the model in COMSOL Multiphysics simulation software.

The model consists of beam and solid elements. The structure is modelled with beam elements to reduce the degrees of freedom of the system unless stated otherwise. E.g. the transition piece is modelled as a solid. For the beam elements, the Timoshenko beam formulation is used. Another option is the Euler-Bernoulli beam formulation. The former is used because it takes shear deformation into account and is thus slightly more accurate. However, the difference would be small because the beams are relatively slender. The solid boundaries are connected with the beam points as if they are 'welded' (COMSOL, 2018b).

Description of the jacket support structure

The support structure is a four-legged jacket with four levels of X-braces, mud braces and four central piles with a penetration depth of 45 m being grouted to the jacket legs. For modelling purposes, the piles are clamped at the seabed. The water depth is 54.38 m, such that the MSL lies at the intersection between sections 3 and 4. The transition piece between the jacket and tower is a block of concrete penetrated by the upper part of the four jacket legs. The conical tower has a total length of 68 m. Resulting in a hub height of 86.17 m. See Figure 4.4 for front and side view. The x-axis of the global Cartesian coordinate system points downwind with respect to the main wind/ice/current direction. The origin lies at the MSL in the centerline of the tower. The jacket is positioned with its sides parallel to the x- and y-axis. Jacket leg 1 (L1) has positive x and y values. Legs 2 (L2), 3 (L3) and 4 (L4) are counted counter-clockwise from L1 in top-view, see Figure 4.5a.

Grouted connection

The structure is clamped at the seabed. Thus, all six degrees of freedom are zero at those positions. Only the part above the seabed is therefore modelled. The piles are connected with grout material at each jacket corner see Figure 4.5b. The pile-grout-leg section is modelled as a tubular section with high stiffness. The density of the grout material is 2000 $[kg/m^3]$. Combined with the steel parts, this results in the following properties:

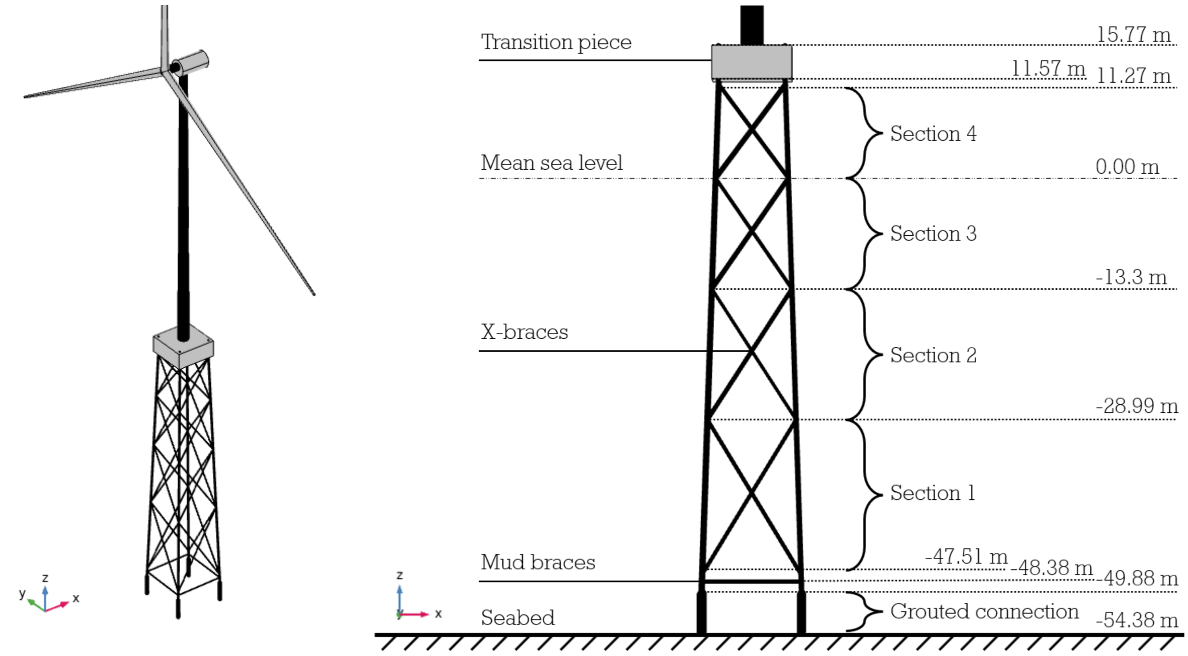

(a) Front view of the model.

(b) Side view of the jacket support structure.

Figure 4.4: Front and side view of the offshore wind turbine. Including definitions and depth levels.

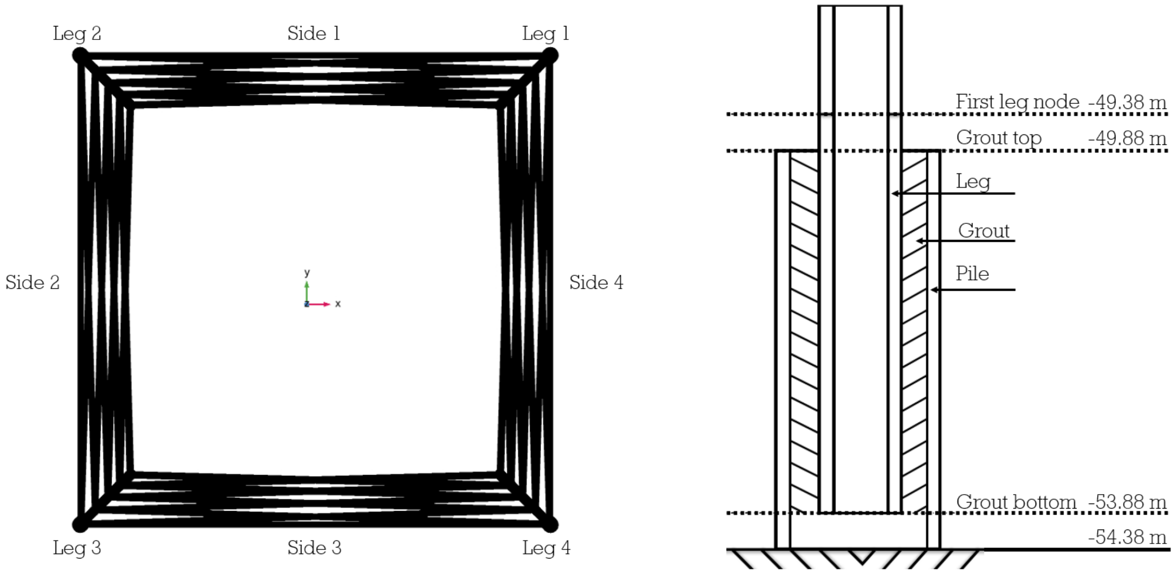

(a) Inclined top view of the model to clarify leg naming.

(b) The pile-grout-leg connection.

Figure 4.5: Inclided top view and a side view of the pile-grout-leg connection.

$$\rho_g = 3339\ [kg/m^3],\quad E_g = 2.1\cdot 10^{15}\ [N/m^2]\quad \text{and}\quad G_c = 8.077\cdot 10^{15}\ [N/m^2]$$

Primary steel

The main part of the jacket consists of its primary steel members. The properties vary for the different parts of the jacket and can be seen in Figure 4.6a. Table 4.1 gives the dimensions for each of the different part. The steel properties used for the structural model are as follows:

$$\rho_s = 7850\ [kg/m^3],\quad E_s = 2.1\cdot 10^{11}\ [N/m^2]\quad \text{and}\quad \nu_s = 0.3\ [-]$$

Table 4.1: Properties of the jacket sub-structure.

Component	Color in Figure 4.6a	Outer diameter [m]	Thickness [mm]
x- and mud braces	cyan	0.8	20
legs at section 1	green	1.2	50
legs at sections 2 up to 4	magenta	1.2	35
legs crossing transition piece	red	1.2	40
piles	black	2.082	60
grouted connection	yellow	2.082	491

Transition piece

The transition piece is modelled as a solid concrete block with higher stiffness. Its mass is 666 $[t]$ and its size is 4x9.6x9.6 $[m]$. It is positioned on top of the jacket, with its centre in the centerline of the tower. The four legs are grouted into the concrete, as can be seen in Figure 4.6a. The displacement and rotation of the connected beam elements are coupled with the concrete block. The properties are as follows:

$$\rho_c = 1807\ [kg/m^3],\quad E_c = 3\cdot 10^{12}\ [N/m^2]\quad \text{and}\quad G_c = 1.34\cdot 10^{12}\ [N/m^2]$$

Tower

The tower is connected on top of the transition piece and has a step-wise diameter see Figure 4.6b. The diameter and wall thickness decrease with height and are displayed in Table 4.2, except for the last section, where the thickness increases again. The sections have a more conservative diameter and thickness. Another option is to model the tower tapered between the nodes. In this model, the diameter changes step-wise.

Table 4.2: Properties of the tower.

Section	Node	Outer diameter [m]	Thickness [mm]	Point mass [t]
5	1	5.600	32	1.9
6	2	5.577	32	No
7	3	5.318	30	No
8	4	5.082	28	No
9	5	4.800	24	1.4
10	6	4.565	22	No
11	7	4.329	20	No
12	8	4.118	30	No
	9	4.000	30	1.0

Rotor Nacelle Assembly

The rotor nacelle assembly (RNA) is modelled as a point mass on node 9 with the respective mass moment of inertia. Since the centre of gravity is not centred relative to the structure. The RNA is also known as the NREL 5-MW reference turbine, described by Jonkman et al. (2009). The RNA weights 350 $[t]$ and its mass moment of inertia are:

$$J_{xx} = 3.22\cdot 10^{7}\ [kg\cdot m^2]\quad \text{and}\quad J_{yy} = J_{zz} = 2.07\cdot 10^{7}\ [kg\cdot m^2]$$

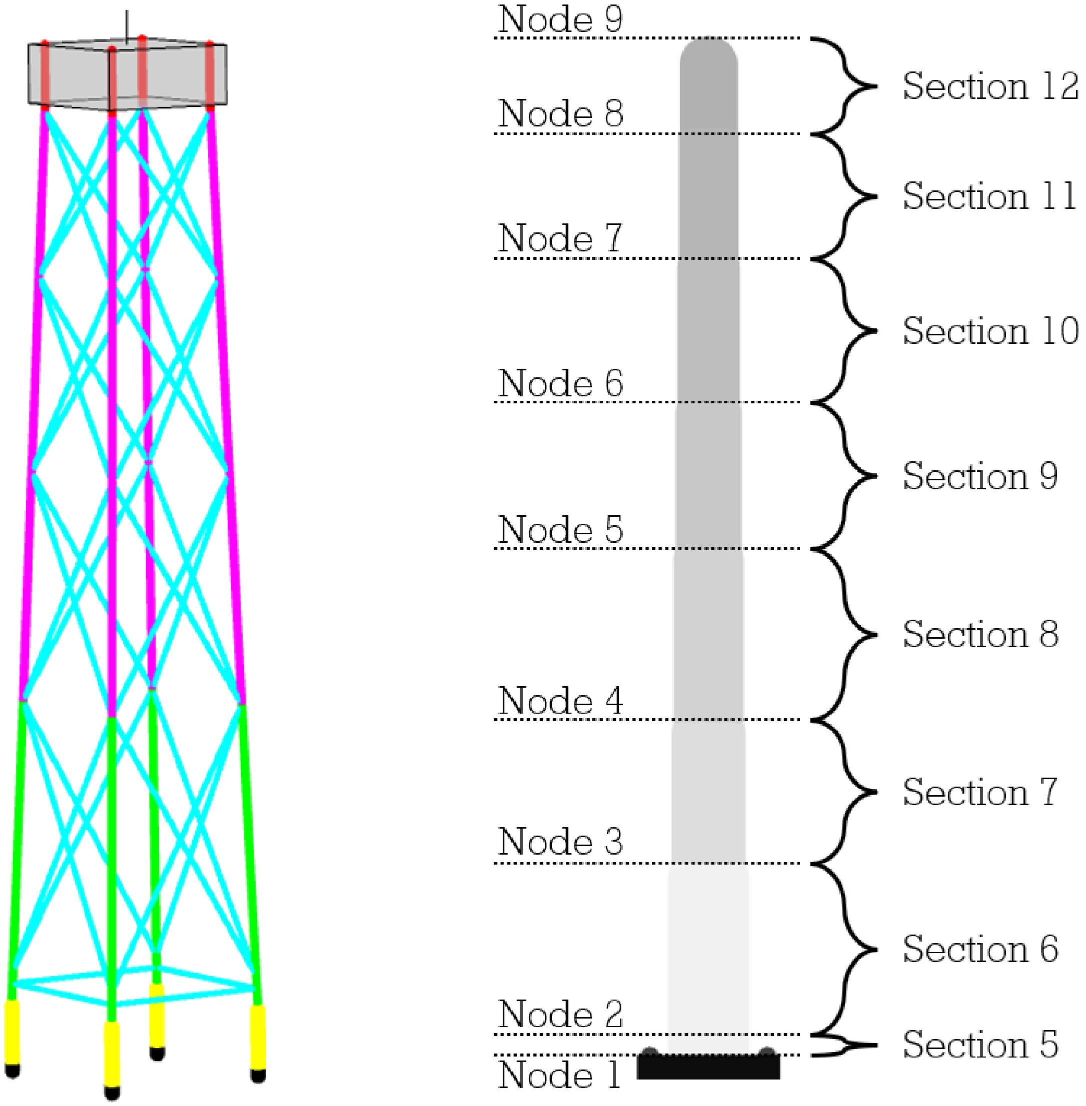

(a) Sub-structure segments

(b) Tower segments

Figure 4.6: The different segments of the jacket sub-structure and tower.

Marine growth and free flooded members

Marine growth adds weight to a structural component and influences the geometry. Hence it may influence the maximum load and dynamic behaviour. Thus it is included in the model by following the respective guideline on marine growth from DNV (2014), see Table 4.3 for the depth range with respect to MSL to apply marine growth. The legs of the jacket structure are assumed to be free flooded by seawater with a density of $\rho_w = 1025\ [kg/m^3]$, and the braces are not.

Table 4.3: Marine growth in the jacket model

Depth range:	$-40 \leq z_g \leq -2\ [m]$
Thickness:	$t_g = 100\ [mm]$
Density:	$\rho_g = 1100\ [kg/m^3]$

Eigenfrequencies

The structural model is explained in the sections above, and an eigenfrequency study can now be computed. The obtained eigenfrequencies are compared with load case 1.0c from Popko et al. (2012). The DOF's from the support structure are enabled, there is no air/wind and gravity, and damping is included. The above-mentioned model is used for the base case tests. However, when implementing the ice jams, the structure had to be slightly adjusted. These changes will be discussed in Section 4.2. Thus in total, three models are used, and their resulting eigenfrequencies can be seen in Table 4.4.

Table 4.4: Overview of the different eigenfrequencies compared to the results from load case 1.0C from the OC4 project.

Mode [Hz]	Average OC4	Standard deviation OC4	Base case	Central jam	Frontal jam
1st global fore-aft	0.313	0.007	0.329	0.331	0.334
1st global side-side	0.311	0.005	0.327	0.328	0.332
2nd global fore-aft	1.153	0.042	1.144	1.149	1.151
2nd global side-side	1.158	0.076	1.125	1.129	1.131
1st global torsion	1.407	0.264	1.425	1.426	1.425

Damping

The reference jacket has a critical structural-damping ratio ζ, equal to 1% and a logarithmic decrement of 6%. Implementing damping in the structural model can be done by using Rayleigh damping. This type of damping is not directly related to any physical property, but it is a way to take the total damping of a structure into account. The critical damping ratio is calculated with Equation 4.17. It is proportional to a linear combination of the stiffness and mass, using the mass damping parameter α_{dM}, and stiffness damping parameter β_{dK}. Which can be calculated using Equations 4.18 - 4.19 by using the known frequencies and their critical damping. The 1st and 2nd fore-aft frequency is used together with the 1% critical damping ratio to obtain these parameters (COMSOL, 2018b). The eigenfrequency study now also shows the critical structure-damping ratio $\zeta_{structure}$, and it is around 1% for the lower frequencies until $1.4[Hz]$ and increasing for the higher frequencies, $> 1.4[Hz]$. The logarithmic decrement $\delta_{structure}$ is also around the 6%, thus in agreement with Vorpahl et al. (2011).

$$\xi = \alpha_{\mathrm{dM}} m + \beta_{\mathrm{dK}} k \qquad [N] \tag{4.17}$$

$$\alpha_{\mathrm{dM}} = 4\pi f_1 f_2 \frac{\varsigma_1 f_2 - \varsigma_2 f_1}{f_2^2 - f_1^2} \qquad [1/s] \tag{4.18}$$

$$\beta_{\mathrm{dK}} = \frac{\varsigma_2 f_2 - \varsigma_1 f_1}{\pi\left(f_2^2 - f_1^2\right)} \qquad [s] \tag{4.19}$$

Simulation duration

What kind of simulation time would be sufficient to say something about the ice-structure interaction? During the initial disturbance/excitation, the ice-structure interaction is in a transient phase. The structure is starting to move, and the outcome is not yet stable. This transient reaction would dampen out over time. The question that rises, after how many seconds is this transient reaction phased out? This can be calculated using the logarithmic decrement method, see Equation 4.20. The logarithmic decrement $\delta, structure$ is known to be 6%. As a conservative estimation, it is assumed that after a 90% reduction of the initial excitation, the initial excitation has no more significant contribution to the steady-state. Thus Equation 4.21 can be used together with the known decrement to calculate n, the number of oscillations needed to have a 90% reduction in amplitude. n multiplied with the period of the first natural frequency would give the most conservative amount of time before simulation data is truly in the steady-state, $n = 38$ multiplied with 3 seconds would give a minimum simulation time of 114 seconds.

$$\delta = \frac{1}{n} \ln \left| \frac{x_1}{x_{n+1}} \right| \tag{4.20}$$

$$x_{n+1} = 0.1 \cdot x1 \tag{4.21}$$

Ice jam

The ice jam is modelled as a linear elastic continuum. This is not fully realistic as concluded in Section 2.1.5 because a correct ice model has to include linear and non-linear aspects of elasticity, visco-elasticity, visco-plasticity and fracture. However, this would make the problem more complex and computational more expensive. For ice rubble properties, the ISO (2019) proposes a hydrostatic pressure-dependent model such as the Mohr-Coulomb material model. Which is based on two parameters: the friction angle ϕ and cohesion c. Serré (2011a) uses the Drucker-Prager material model, which is equivalent to the Mohr-Coulomb material model. However, for these models, their precision and quality are strongly depending on the physical parameters. ISO (2019) states that the friction angle can vary between 10° to 80° while recommending 25° to 45° and the cohesion value can vary from $0[kPa]$ to $100[kPa]$. Thus the natural variation in physical properties is large, and experiments need to be conducted to validate the used parameters.

Besides that, the main focus of this research is on the influence of an ice jam on ice-induced vibrations. What happens if there is a jam in between the legs of a multi-legged structure? Thus precise modelling is not yet necessary. A global glance at its influences on the ice-induced vibrations is the purpose of the model. Also, after each test, the local stresses can be checked whether or not the ice jam would have failed. Concluding, this more simple approach is sufficient for the needs of this research. The properties of the ice jam are as follows. The ice strength C_R, is taken from ISO (2019) which recommended 1.8 $[MPa]$ for the Baltic sea.

$$\rho_{ice} = 900\ [kg/m^3], \quad E_{ice} = 5\ [MPa] \quad \text{and} \quad C_R = 1.8\ [MPa]$$

COMSOL Multiphysics makes use of Contact nodes for modelling contact problems. A problem that now arises is that the Contact nodes cannot be used with beam elements. Thus the section at which the jam is placed has to be modelled with a solid element, see Figure 4.7a. The beam points (in purple) are coupled with the solid element (in yellow). Their rotations and displacements are the same. The beams are 'welded' onto the solid element. Every contact node has a source and destination boundary. The legs are the source, and the jam is the destination boundary because the legs are stiffer. The mesh on the destination side has to be finer than the mesh on the source side. However, a finer mesh increases the much needed computational power see Figure 4.7b. The pressure is calculated with Equation 4.22:

$$P_{contact} = -\frac{f_p E_{char}}{min(h_{mesh})} d_{gap} \qquad [N/m^2] \tag{4.22}$$

The obtained pressure $P_{contact}$ is a function of the penalty factor f_p, characteristic stiffness $E_c har$, the minimum element size of the destination h_{mesh}, and the distance of the gap d_{gap}. The penalty factor is an arbitrary number that can be used to fine-tune the solver process. A higher penalty factor will decrease unphysical penetration, but the solver will be less stable. Also, the number of iterations needed for convergence will increase. The default is for the penalty factor is 1. The characteristic stiffness is the Young's modulus. The distance of the gap will be negative if there is contact. Furthermore, if there is no contact, there will be no contact pressure either COMSOL (2018b).

LiveLink for MATLAB

An important element is the LiveLink for MATLAB connection between COMSOL Multiphysics and MATLAB, since the ice forces are calculated in MATLAB while the dynamic structural part is in COMSOL Multiphysics,

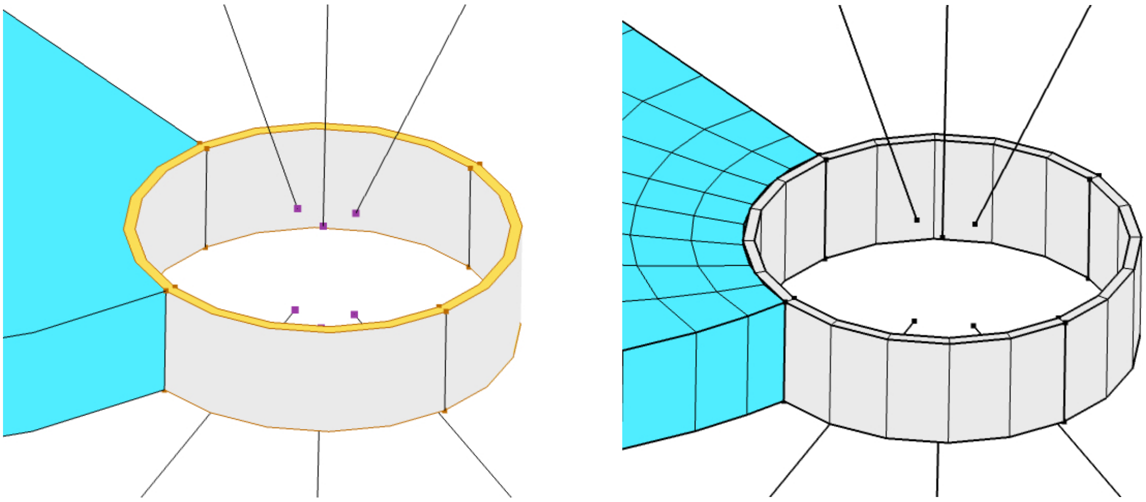

(a) Interaction between beam-solid elements.

(b) Mesh of the jam - leg connection.

Figure 4.7: Side-view of the jam-leg connection.

the main source is COMSOL (2018a). The first priority is enabling External MATLAB functions from within the COMSOL Desktop. Then the MATLAB Function Node can be added to the structural model. The function name should be the same as the name of the function.m file, as this is the filename the LiveLink will search for in its directory. An important consideration is that the input and output both must be vectors of the same length. All arguments and results must be double-precision vectors real or complex-valued. With this consideration in mind, the functions can be added. For every leg/jam a new function is needed. This is because some data stays stored within the MATLAB function as it cannot be extracted or added due to the limitation regarding input/output. Thus if there is ice loading on L1, L2 and the jam, then three functions are needed.

Solver settings

The implicit time-dependent solvers break down each problem into one or several linear systems of equations by approximation the given problem with a linearized problem, this paragraph is based on COMSOL (2019) and COMSOL (2018b). The coefficient matrix of this discretized linearized problem is called the Jacobian or system matrix. This is done by using the backward differentiation formulas(BDF) or generalized-α solver. The BDF method ranges from first (equal to backward Euler) to fifth-order while the generalized-α is similar to second-order BDF. Low order BDF has severe numerical damping for higher frequencies. But the advantage of BDF is that it is more robust, thus more stable and better at handling changes to the time step. The generalized-α is more accurate and preferred when the time step is constant. A non-linear solver is used to update the variables at each time step. The discretized linearized problem is of the following order

$$[A+\sigma B+\sigma^2 C]x = b \tag{4.23}$$

where A is the stiffness matrix, B is the damping matrix, and C is the mass matrix. This system is then solved using the direct MUMPS solver. A direct solver is more robust and costs more memory but is quicker to solve the system than an iterative solver. The sparsity pattern is stored and reused if possible to improve solution performance. To further improve the solution performance, the Batch Sweep function is used. This function utilizes multi-core computing, which can run a number of processes parallel with a certain amount of cores for each process. A parameter sweep is made over the ice velocities. E.g. five simulations are running parallel to test a range of 5 ice speeds, with two cores allocated for each simulation. Resulting in a significant speed-up of the total solution time.

For the base case, the BDF is chosen with a free time-stepping scheme with a maximum time step of 0.005s. Its order is automatic based on the residual error. For the jammed situation, the Contact node is used, for which manual time-stepping should be used because the solver can otherwise try to solve wave propagation through domains adjacent to the contact pairs. This could decrease the time step significantly and would unnecessarily increase the computation time. For manual time stepping, the recommended solver is the generalized-α, which is used.

4.1.3. Model overview

The models to calculate the ice load and the structural model are explained in the sections above. A global overview of this interaction is shown in Figure 4.8. This section goes briefly through the flow of the flowchart and discusses how everything is coupled.

It starts with setting up the structural model and the ice jam. Then an assembly can be made with the contact nodes. This should be double-checked, because they are created automatically. Now the mesh can be generated. Now it is important to double-check the mesh around the contact nodes and make sure the boundary has meshed finer than the source. The simulation can now be started with the solver/simulation settings and make sure that the LiveLink is enabled and the MATLAB functions are set up in the model. In the initialization phase, all dependent variables are set up, and the matrices are assembled. Since the ice force is still unknown to COMSOL Multiphysics, a call is made to MATLAB. The global flowchart of the MATLAB model can be seen in Figure 4.9. This call is made at $t = 0$ to check the ice force in the initialization phase. The blue parts are now discussed, and the green ones will be elaborated on in the next paragraphs. Due to the input/output restrictions of the MATLAB Function Node, the ice field has to be stored within the MATLAB function while making sure nothing from outside the function can delete that data, other processes or scripts. Thus all the variables in MATLAB are made persistent, e.i. they are only visible for the function itself and are stored locally in the function's memory. Only if the memory is cleared, this data will be gone. Then the preprocessor is run for these input parameters, and those results are saved as well. Then the ice field can be initialized and saved. For $t = 0$, the function ends here since the ice field is generated a small distance from the structure. Thus the ice force is zero. Now that the model is initialized, the time-dependent study can begin.

Depending on the solver settings for the basecase, the BDF solver comes with a time-step control which determines the time step with a maximum of 0.005s. For the jammed situations, the generalized-α uses 0.005s as time step. A non-linear solver, Newton Method, is used to update the variables at the next time step. It starts with an initial guess U_0, where U is the solution vector. $f(U)$ is the residual vector, see Equation 4.24. The solver then forms a linearized model using U_0 as the linearization point. Then it solves the discretized form of the linearized model for the Newton step δU using the linear system solver, Equation 4.25. Then it computes the new iteration solution vector U_1, see Equation 4.26. Where λ is the damping factor, which is 1. Thus, this non-linear solver guesses the next solution and checks it with the derivative until it convergences, and the residual is below the threshold, i.e. close to zero.

$$f(U) = 0 \tag{4.24}$$

$$F(U_0)\delta U = -f(U_0) \tag{4.25}$$

$$U_1 = U_0 + \lambda \delta U \tag{4.26}$$

Now that there is an 'educated guess' on the solution, the ice force will be calculated with MATLAB. The arguments of the MATLAB function are the current time t, the displacement at time t u_t, the ice velocity v_{ice}, the ice strength C_R, the ice thickness h_0, the width d and the maximum time T_{max}. A global flowchart of the MATLAB model is visible in Figure 4.9.

1. If it is the first time, thus $t > t_{last}$ then this time will be saved in the time vector, and a vector of length N with random numbers between 0-1 will be generated and saved. The use of that will become clear at point five.
2. Now the ice velocities are calculated using Equations 4.6 - 4.7. Keep in mind that these are the ice velocities at t_{last}, calculated using the ice field positions and structure displacement at t_{last}.
3. Using the difference between t and t_{last} the time step can be determined, and the ice field is updated for time t.
4. The model now checks all the ice elements if they have exceeded the critical deformation.
5. If so, then based on Equation 4.9 a new element is produced. The uniform distribution between zero and r_{max} is achieved by using a random number between 0-1 and multiplying that with r_{max}. Here is

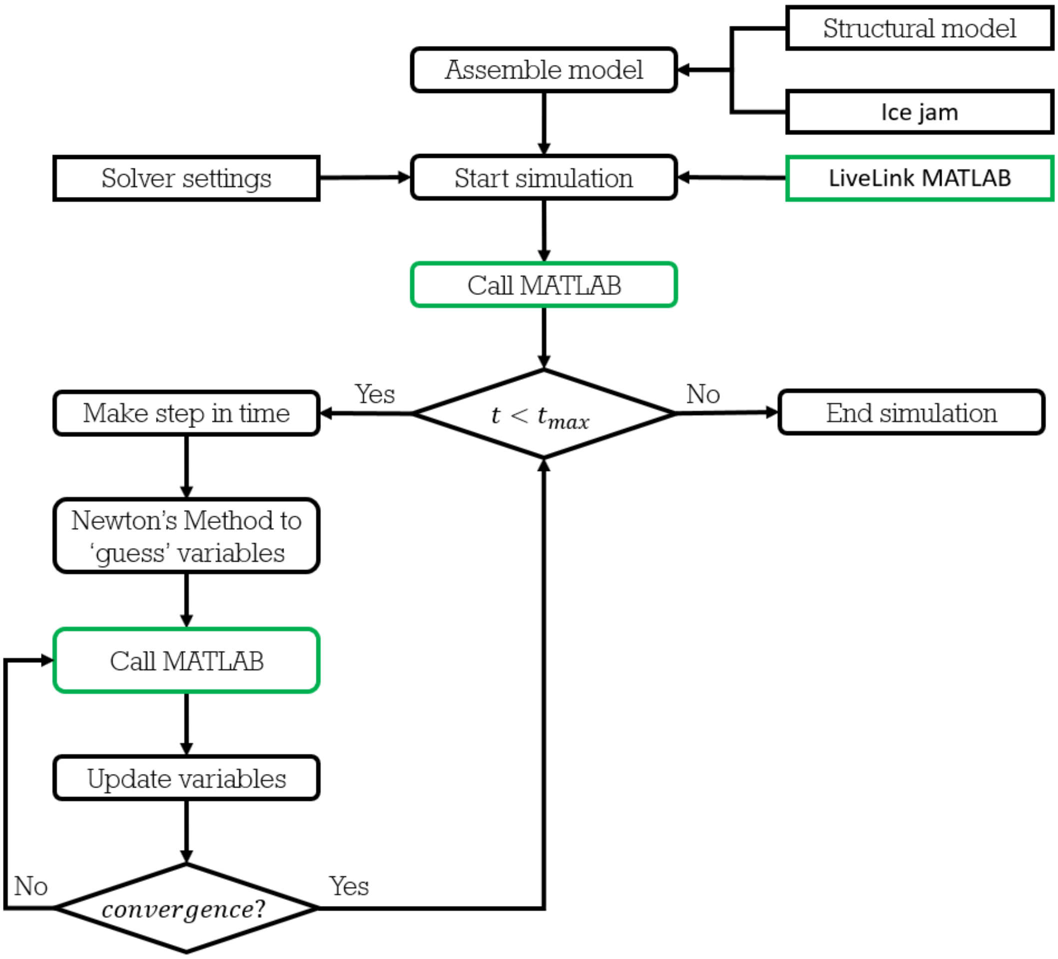

Figure 4.8: Global flowchart of the model

where the vector with stored random values comes in. During the iterations towards convergence, the same elements will fail and have to be replaced with the same element to prevent difficulties converging. Between time steps, the random number changes so that the uniform distribution will be obtained.

6. The ice load can now be obtained with Equation 4.8.

7. All the data is stored in the persistent variables.

Now there is a new ice force, and COMSOL Multiphysics updates its variables and checks for convergence. Suppose this is below a threshold, i.e. almost zero. Then it goes to the next iteration. However, if it is not converged, then MATLAB is called with a newly obtained displacement. The main difference now in the function overview is that only the new ice load has to be calculated because the ice velocities depend on the previous step's ice field and structural displacement. Now, there is another situation it does not converge at all. Then after 25 iterations, the solver goes back to the previous time step and tries a time step that is one-fourth of the original time step and tries again.

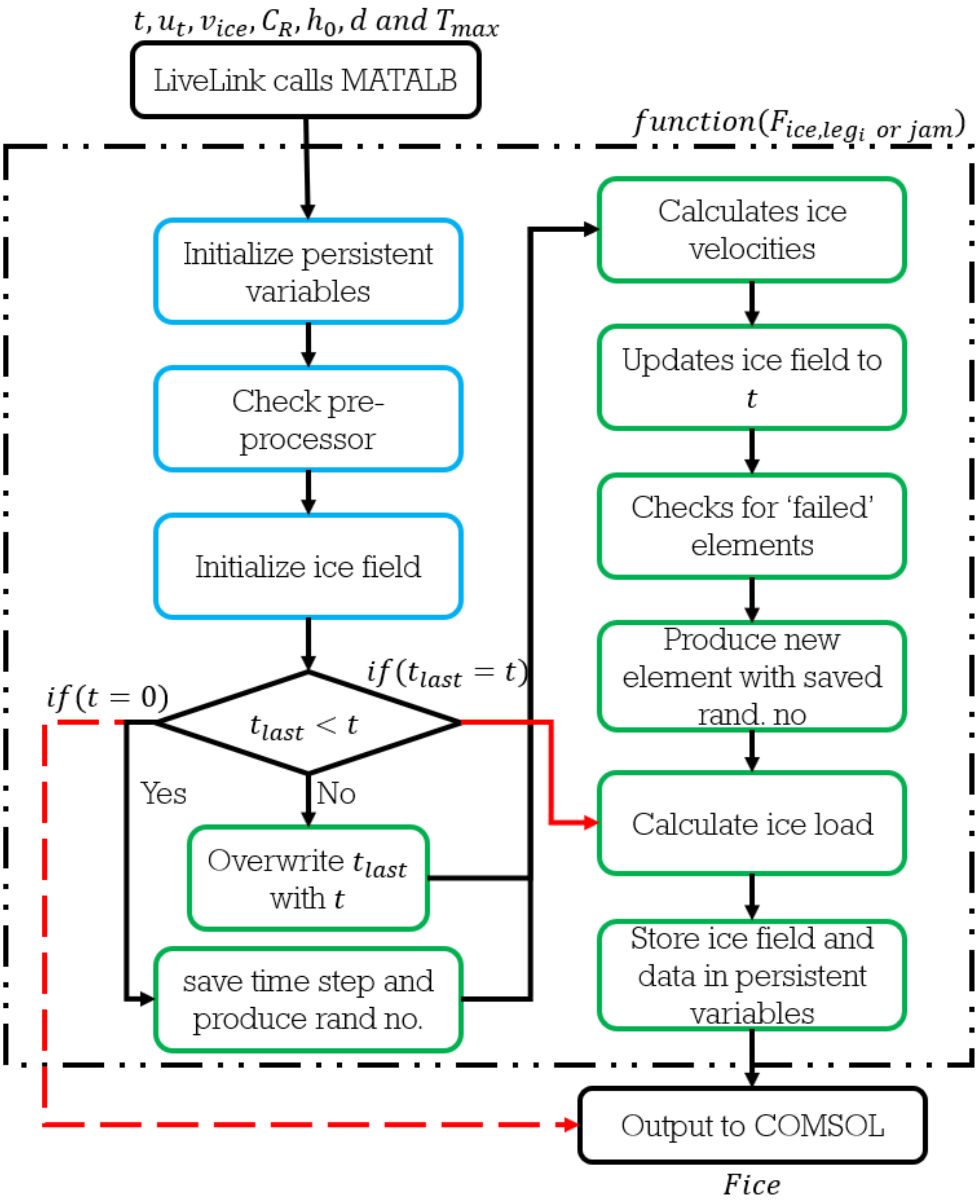

Figure 4.9: Global flowchart of the MATLAB model

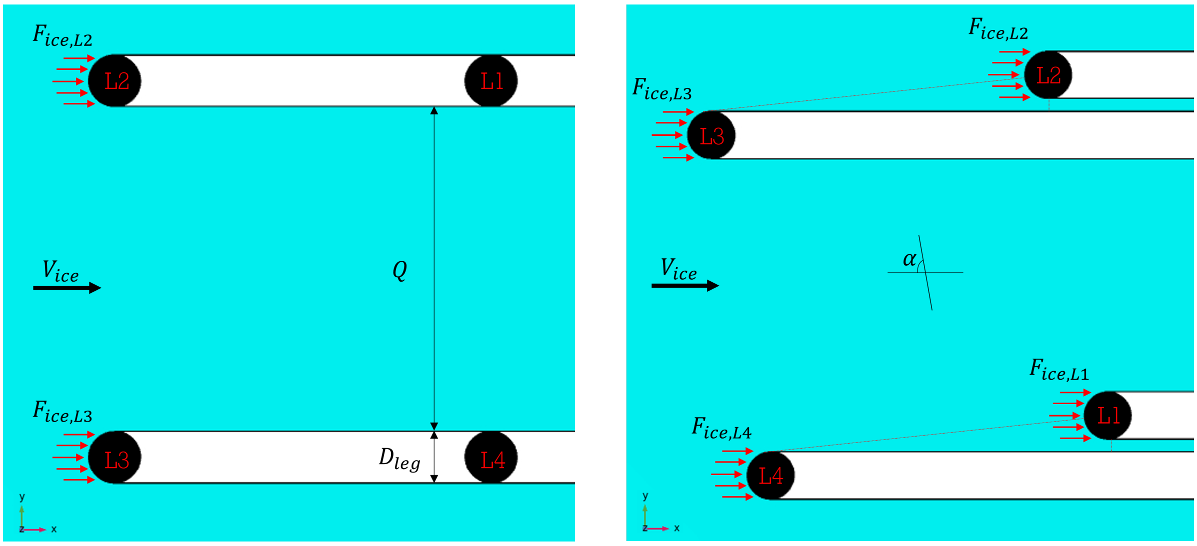

(a) Top view base case, situation A

(b) Top view base case, stucture under an angle, situation B

Figure 4.10: Top view base cases

4.2. Model scenarios

The above-described model is used for different scenarios. In Section 2.4 two different types of jams were identified, the frontal and internal jam. In order to evaluate the influence of the jam, a base case is necessary. There is an angled scenario for the base case and frontal ice jam at which the structure is rotated 80°. This angle was chosen such that an ice jam has the most chance of holding. With this angle, the frontal jam is still pushed into the legs, thus stable. At the same time, keeping the jam on the same legs (L2 & L3) as in the standard case. The ice travels in the positive x-direction for all scenarios.

Base case

The base case consists of a normal scenario A, and the angled scenario B, see Figure 4.10. For scenario A the rear legs shelter behind the front legs, as can be seen in Figure 4.10a. For the angled scenario, this is not the case see Figure 4.10b. For both these scenarios, the whole sub-structure is modelled using beam elements, with the ice load on the legs in contact with the incoming ice floe.

Internal ice jam

The internal jam can be seen in Figure 4.11. The ice jam is modelled as a solid between the four legs, with the above-mentioned properties. The legs and jam are both modelled using solid elements. This is needed for the contact nodes to work. The ice jam has the same thickness as the incoming ice.

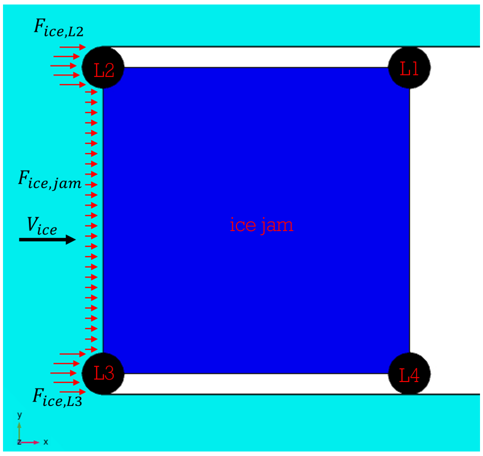

Figure 4.11: Top view internal jam

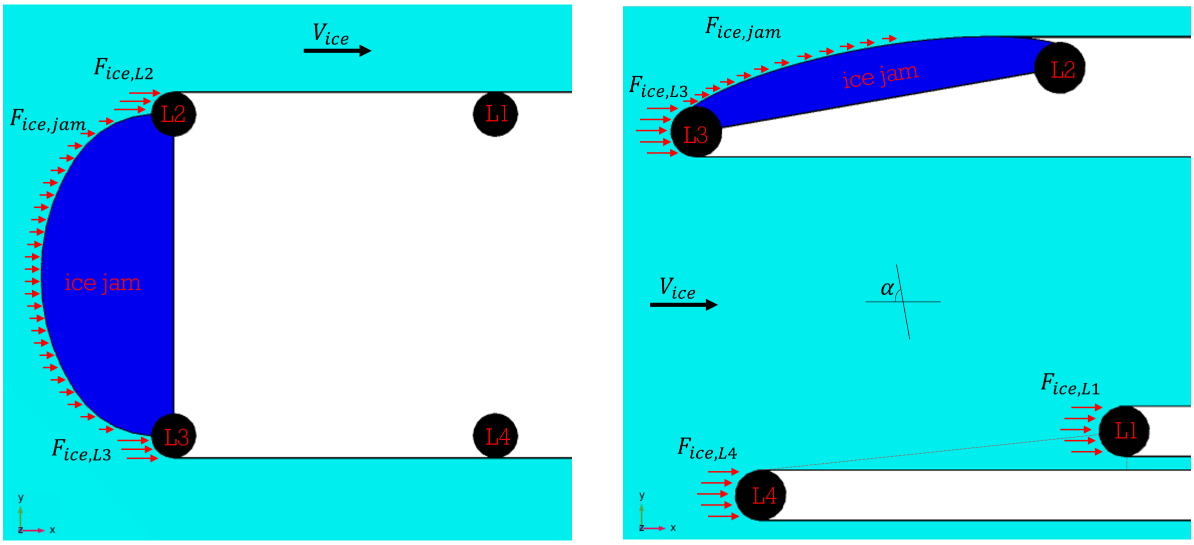

(a) Frontal jam

(b) Frontal jam under an angle

Figure 4.12: Top view frontal jams

Frontal ice jam

The frontal ice jam is modelled for two scenarios, the normal scenario A and the angled scenario B, see Figure 4.12. The ice jam and the legs which are in contact with the jam are modelled as solids. The thickness of the ice jam for scenario A is the same as the incoming ice. For scenario B, the thickness is twice the thickness of the incoming ice. This represents a broken piece of rafted ice, which is formed by one piece of ice over-riding another. Hence twice the thickness of the incoming ice floe.

4.3. Simulation matrix

Table 4.5 shows the simulation matrix. In this table, all the different scenarios and their respective parameters are shown. The ice strength $C_{R,M}$ shown here is used in the MATLAB model to calculate the ice load and is thus slightly different than the ice strength of the ice jam. The simulation time is a lot smaller for the scenarios with ice jams. This is due to the computational power required in order to compute those contact forces and pressures. The maximum time step for all simulations is 0.005 seconds. The solver might take a smaller time step if the model does not converge.

Table 4.5: Simulation matrix

Scenario		$h_0 [m]$	$C_{R,M} [MPa]$	$h_{jam} [m]$	$\alpha [°]$	Sim. time $[s]$	Ice speed $[m/s]$
Base case	A	0.35	1	-	0	120	0.01:0.01:0.15 - 0.2 0.25 - 0.3 - 0.4 - 0.5
	B	0.35	1	-	80	120	0.01:0.01:0.15 - 0.17 0.20 - 0.25 - 0.30
Central jam		0.35	1	0.35	0	15	0.01 - 0.04 - 0.08 - 0.15
Frontal jam	A	0.35	1	0.35	0	15	0.01 - 0.04 - 0.08 - 0.15
	B	0.35	1	0.70	80	15	0.01 - 0.04 - 0.08 - 0.15

5

Results

The influence of an ice jam on the ice-induced vibrations is tested for different scenarios. These scenarios were determined through the literature study. The results of these scenarios are shown in this Chapter. The results of the base case scenario are shown in Section 5.1. This scenario is meant as a reference and baseline for the other results. The results from the internal jam are shown in Section 5.2. At last, the results from the frontal jam are shown in Section 5.3.

The used global ice load is on the indicated leg and **not** the total global ice load. The structural velocity and displacement are at the waterline of the indicated leg. The results are shown for one leg to keep the graphs clear, as can be seen in the Appendix A - Figures A.1 - A.5. the displacement of the legs follows the same pattern. There is a vertical shift, but the amplitude and frequencies remain similar. For all the scenarios **leg 3** will be used for the comparison. For the base case scenarios, the global ice load, structural velocity and structural displacement on and from leg 3 are displayed for the ice drift velocities used during simulations for the jammed scenarios. The full force-time traces for these scenarios are shown in Appendix B - Figures B.1 and B.2. For the jammed scenarios the structural displacement is shown and the force-time traces are shown in Appendix B - Figures B.3 - B.5, in this Chapter only their structural displacement is plotted to keep the amount of plots manageable.

The different ice-induced vibration regimes, as explained in Section 2.6 are used to identify the structural response for the base case at different velocities and then compared to the jammed scenarios. Because it is an important observation, the definitions are restated from Owen and Hendrikse (2019):

- The intermittent crushing can be identified based on structural displacement and global ice load time trace following a sawtooth-like pattern. The maximum global ice loads during intermittent crushing should be greater than or equal to those observed during frequency lock-in vibrations.
- Frequency lock-in is categorized by the ratio of the maximum structural velocity and the indentation speed, known as β, between 1.0-1.5. When β is between 1.0 - 1.5, the structural response is quasi-sinusoidal near the structures natural frequency. The global ice load is periodically amplified, ensuing the time when the relative velocity between ice and structure is low. The relative velocity is the structural velocity minus ice drift velocity.
- Continuous brittle crushing is classified by a stochastic global ice load time trace with maximum and mean global ice loads that are not greater than those observed during intermittent crushing and frequency lock-in vibrations. The structural response is similar to that of a structure excited by an aperiodic load with maximum and mean displacement that is lower than those observed during intermittent crushing and frequency lock-in vibrations. At last, the β value is less than 1.0 for three consecutive cycles of structural vibrations.

5.1. Base case

The goal for the two base case scenarios was to establish the baseline. A reference point to compare the results with from the jammed scenarios. For scenario A the structure's sides are parallel with the x- and y-axis. For scenario B the structure is rotated 80° as indicated in Figure 4.10b. The rear legs no longer have shelter behind the front legs.

Base case scenario A

For this scenario, a wide range of ice drift speeds is simulated. The results are shown in Figures 5.1 - 5.4 for the same ice drift speeds used in the jammed scenarios. The full simulation is 120s, but for readability, only a section of the simulation is shown. The full force-time traces of the same simulations are shown in Figure B.1. Looking at Figures 5.1 - 5.4, the development of the ice-induced vibrations is well defined. The sawtooth-like pattern is observed at lower ice drift velocities for the global ice load and structural displacement. The structural velocity is approaching the ice drift velocity before failure. Then at slightly higher velocities, between $0.04-0.08[ms^{-1}]$, the global ice force changes to an aperiodic nature while having periodically amplifications ensuing the time when the relative velocity between ice and structure is low. These trends are still observed at $0.15[ms^{-1}]$. The max-normalized amplitude spectrum for the four different ice drift velocities are shown in Figure 5.5. This spectrum is calculated using the second half of the simulation. Thus data from 60s until 120s were used to filter out the transient effects. Here it is clearly visible that the frequency of the structural displacement moves towards its 2nd eigenfrequency, resulting in higher structural displacements and velocities. In Figure 5.10 the statistical of the global ice load and structural velocity are plotted over the wide range of ice drift speeds. In the top graph, the statistics from the global ice load are plotted. Which shows a decay in the maximum, mean and standard deviation of the global ice load with increasing ice drift speed. At lower ice drift velocities, the decay is stronger compared to higher ice drift velocities. In the bottom graph, the maximum value of the structural velocity is plotted against the ice drift speed. The dashed lines show the 1.0 - 1.5 relation between structural velocity and ice drift speed.

With these results and the definitions as mentioned earlier for the ice-induced vibration regimes, it can be concluded that the structure is in the intermittent crushing regime between 0.01 - $0.05[ms^{-1}]$ at which it transitions into the frequency lock-in regime until $0.2[ms^{-1}]$. At which it transitions into the continuous brittle crushing regime.

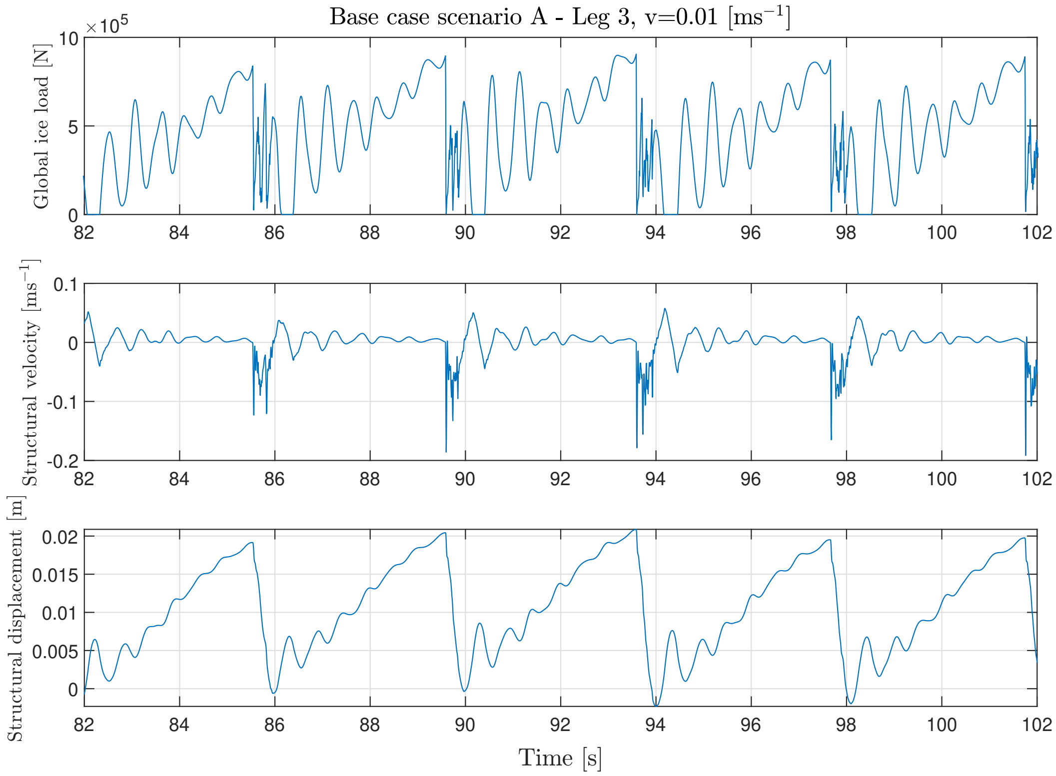

Figure 5.1: Base case scenario A - global load and structural response Leg 3, v=0.01ms^{-1}.

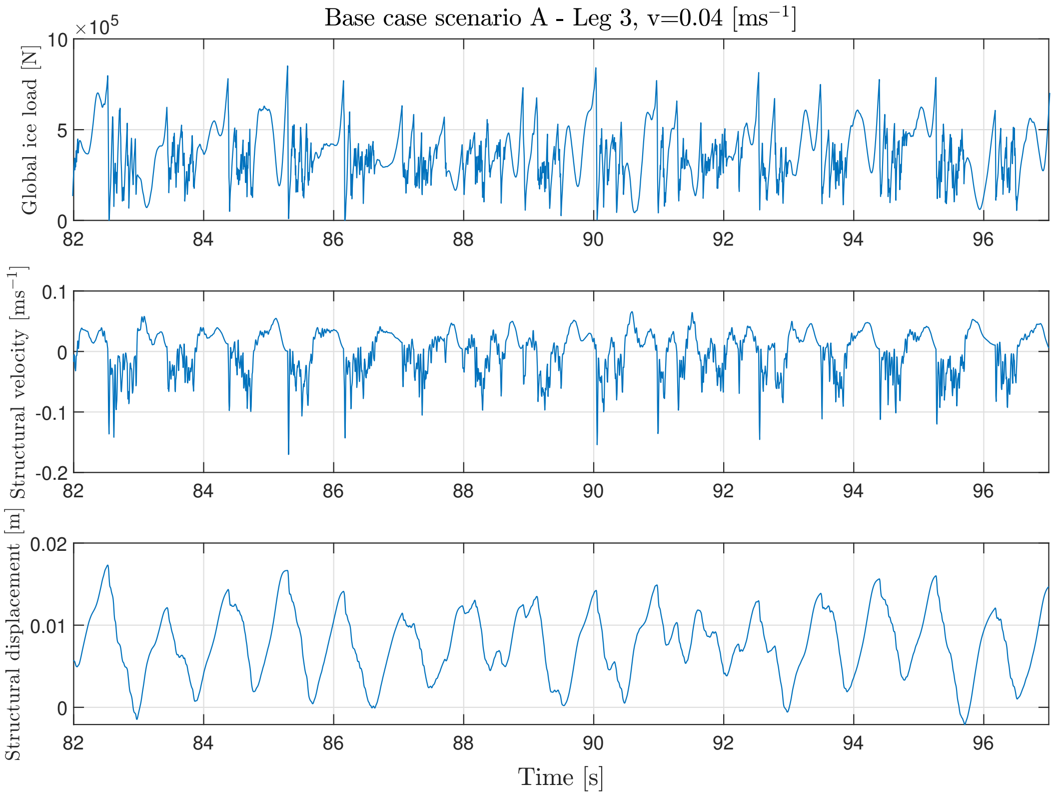

Figure 5.2: Base case scenario A - global load and structural response Leg 3, v=0.04ms^{-1}.

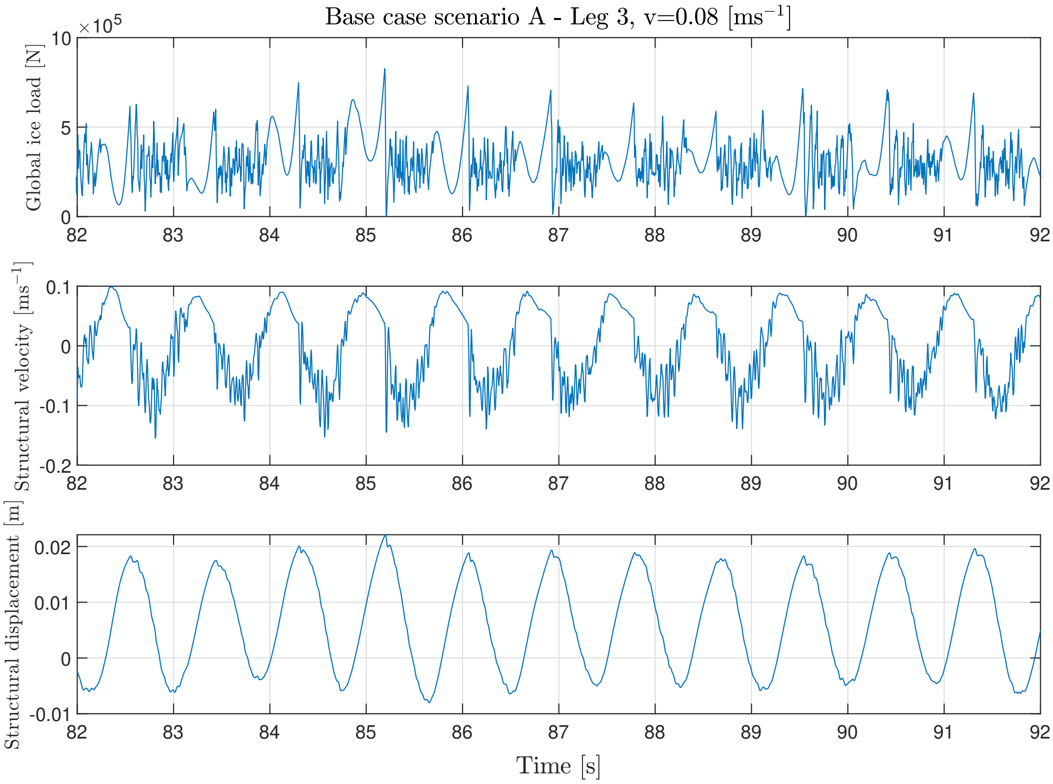

Figure 5.3: Base case scenario A - global load and structural response Leg 3, v=0.08ms^{-1}.

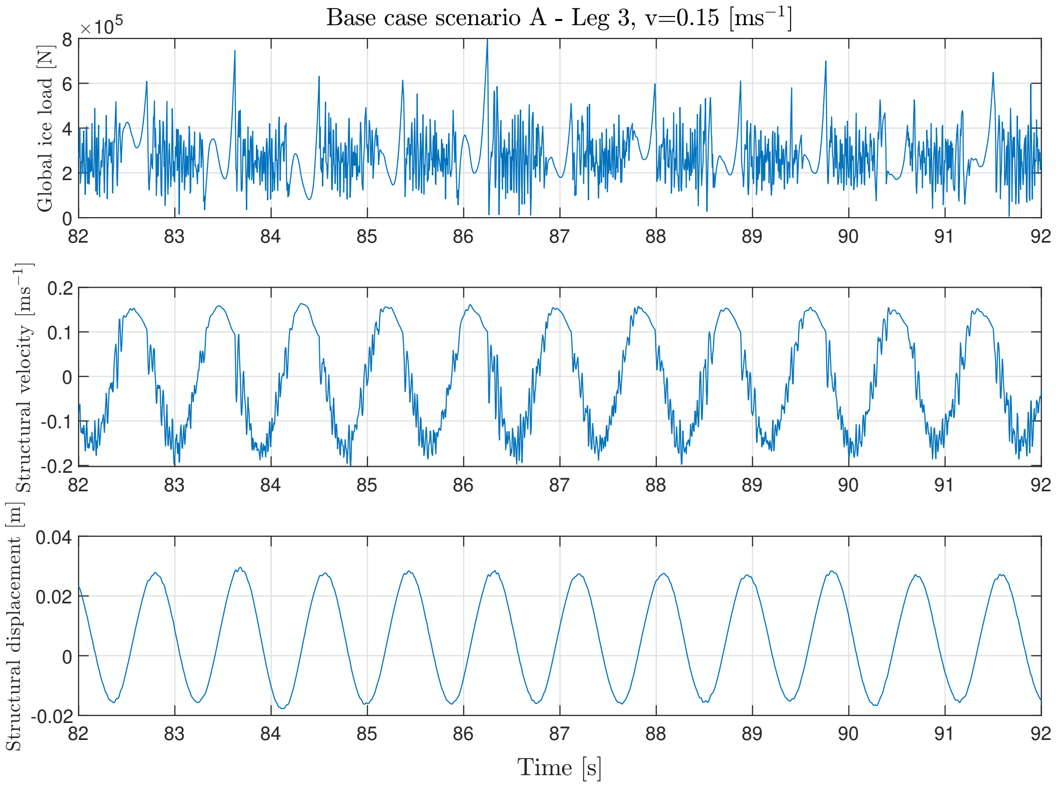

Figure 5.4: Base case scenario A - global load and structural response Leg 3, v=0.15ms^{-1}.

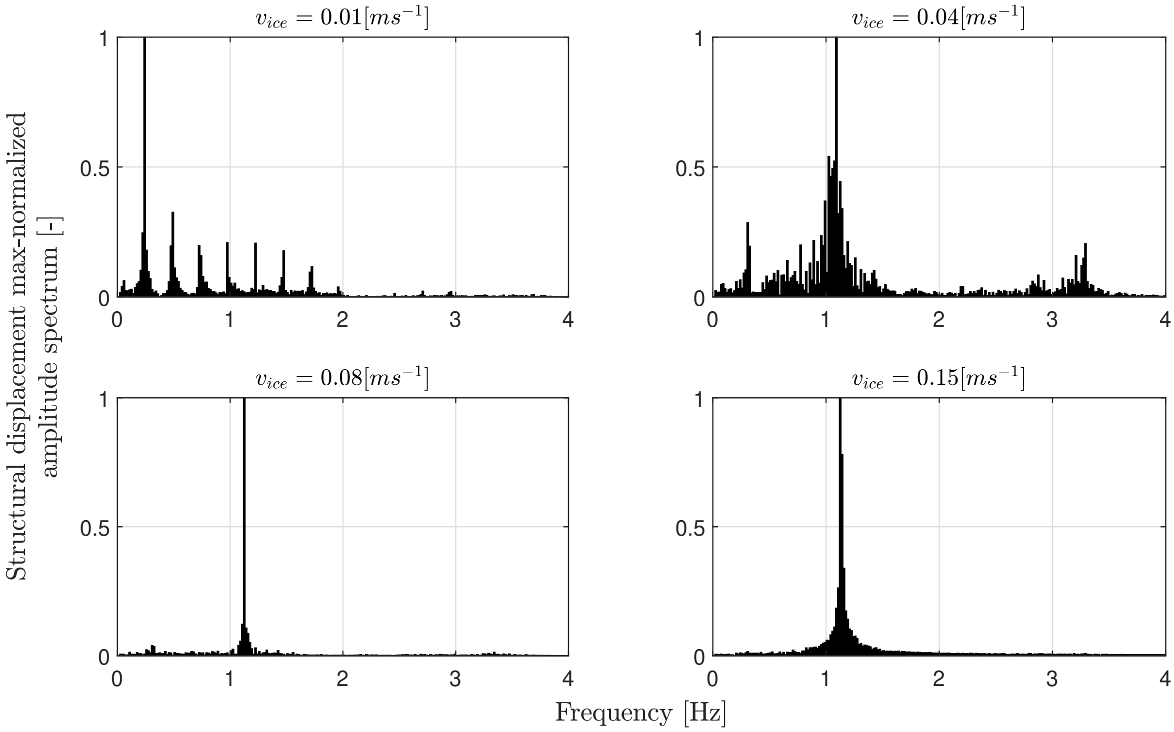

Figure 5.5: Base case scenario A - max-normalized frequency spectrum structural displacement leg 3. The second half of the simulation (60-120s) were used to calculate the frequency spectrum.

Base case scenario B

In scenario B, four legs are in contact with the incoming ice floe. Resulting in a higher total global ice load. The global ice load, structural displacement and velocity for leg 3 are shown in Figures 5.6 - 5.9. The full force-time traces of the same simulations are shown in Figure B.2. The saw-tooth-like pattern is observed for the global ice load and the structural displacement for the lower ice drift. Then at slightly higher velocities, $0.04-0.08[ms^{-1}]$, the global ice force changes to an aperiodic nature while having periodically amplifications ensuing the time when the relative velocity between ice and structure is low. These trends are still observed at $0.3[ms^{-1}]$. In Figure 5.10 the statistical of the global ice load and structural velocity are plotted over the wide range of ice drift speeds. These results are similar to scenario A, albeit that the maximum global ice load is higher at higher ice drift velocities. In the bottom graph, the maximum value of the structural velocity is plotted against the ice drift speed. The dashed lines show the 1.0 - 1.5 relation between structural velocity and ice drift speed.

With these results, it can be concluded that the structure is in the intermittent crushing regime between $0.01-0.08[ms^{-1}]$ at which it transitions into the frequency lock-in regime until $0.3[ms^{-1}]$.

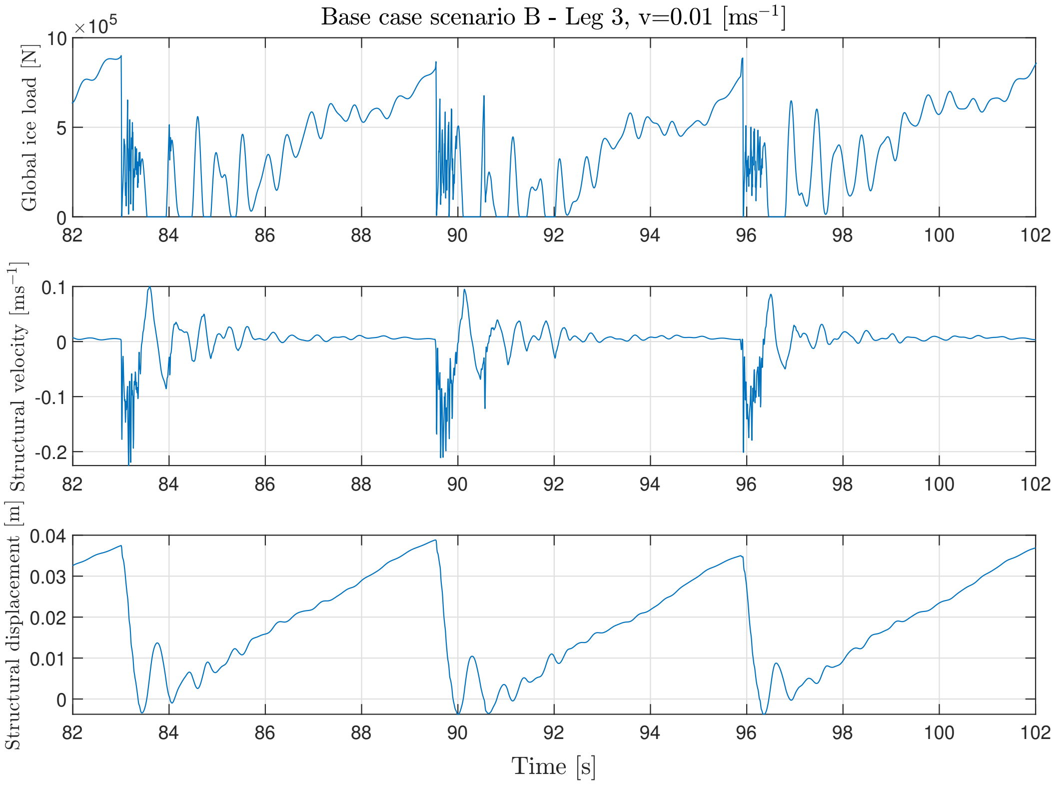

Figure 5.6: Base case scenario B - global load and structural response Leg 3, v=0.01ms^{-1}.

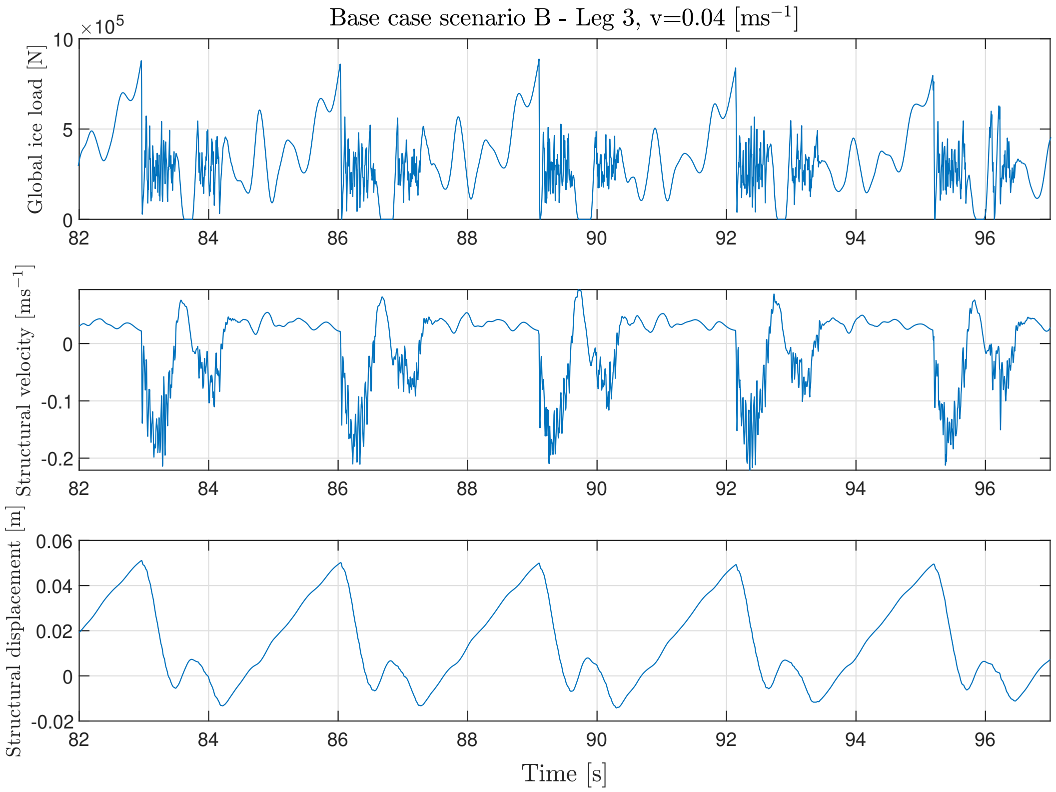

Figure 5.7: Base case scenario B - global load and structural response Leg 3, v=0.04ms^{-1}.

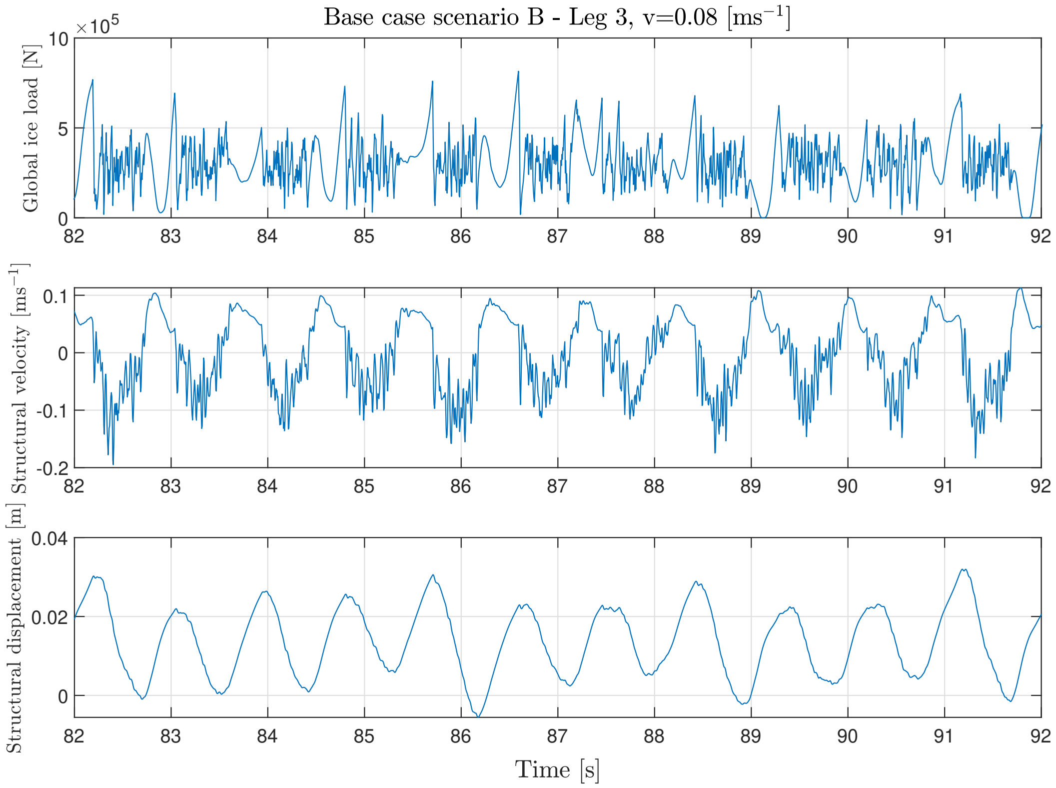

Figure 5.8: Base case scenario B - global load and structural response Leg 3, v=0.08ms^{-1}.

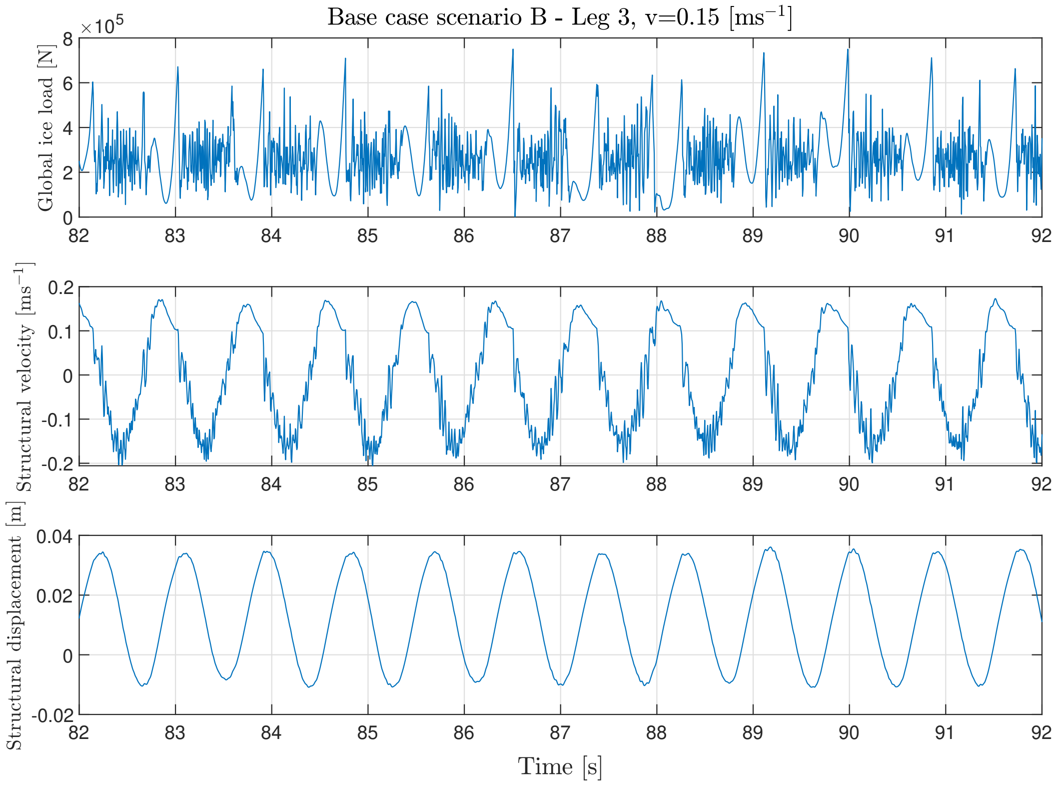

Figure 5.9: Base case scenario B - global load and structural response Leg 3, v=0.15ms^{-1}.

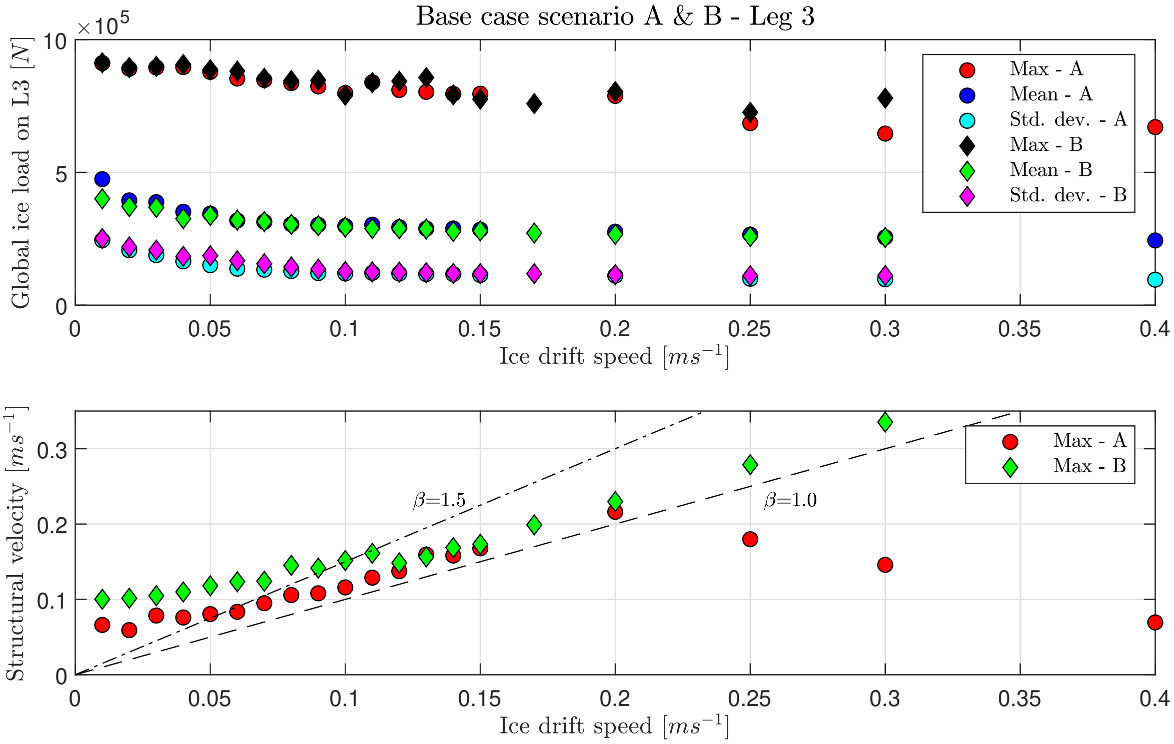

Figure 5.10: Base case - global ice load statistics from the last half (60-120s) of the simulations and maximum velocity over ice drift speed.

5.2. Internal jam

The internal jam is jammed in between the four legs of the jacket, see Figure 4.11, With ice forces on legs 2, 3 and on the ice jam. The structural displacement and internal stress are shown in Figures 5.11 - 5.12 and the force-time trace is shown in Figure B.3. Figure 5.11 shows for lower ice velocities the saw-tooth like pattern and for the higher velocity an oscillation around its second eigenfrequency. The periods of one cycle of intermittent crushing is longer than the base case as well that the transition between intermittent crushing and frequency lock-in happens at higher ice drift speeds. The amplitude of the structural displacement is a factor 2 higher for the lower ice drift speeds and roughly the same for the higher ice drift velocities. The oscillations have more irregularities, however, they still converge to a period that is equal to the second natural frequency of the jacket. Figure 5.12 shows the von Mises stress in the ice jam at two time steps for 0.04$[m/s^{-1}]$. Which correspond to the build-up and collapse of the first peak in the structural displacement, see Figure 5.11. The stresses near the rear legs, L1 & L4, are the largest and exceed the ice strength. This happens at both time steps.

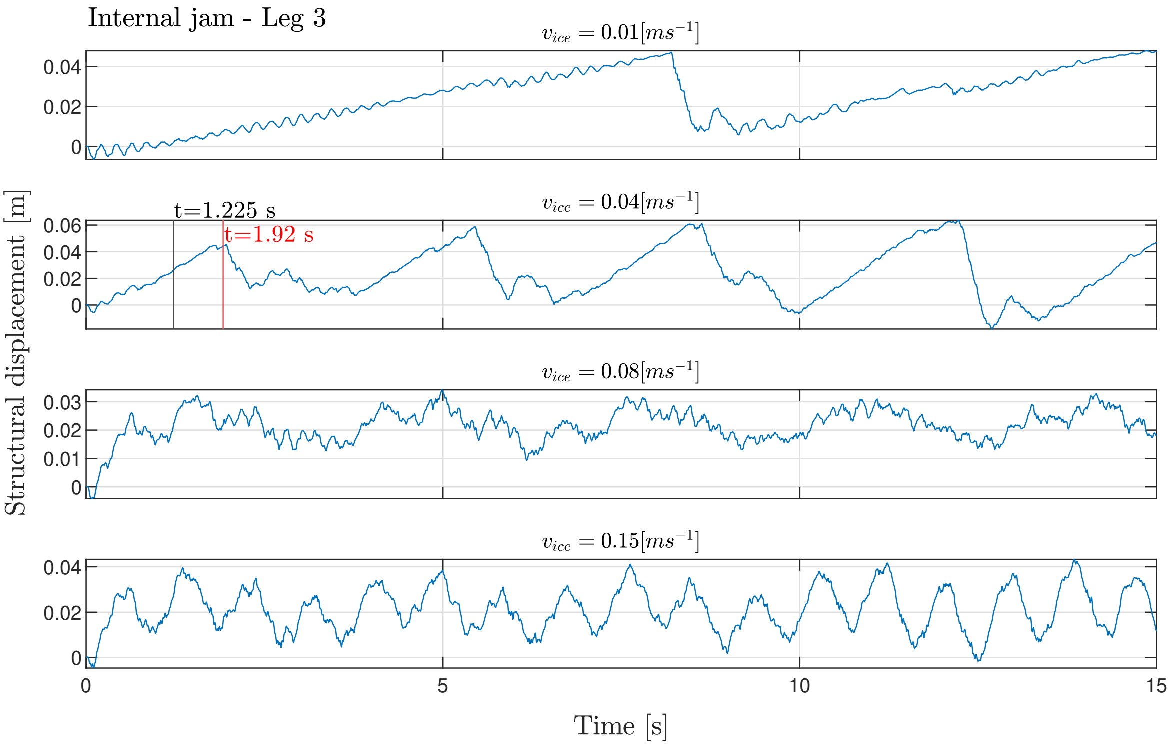

Figure 5.11: Internal jam - structural displacement leg 3. The indicated time instances show the moment at which the snapshot is taken that can be seen in Figure 5.12.

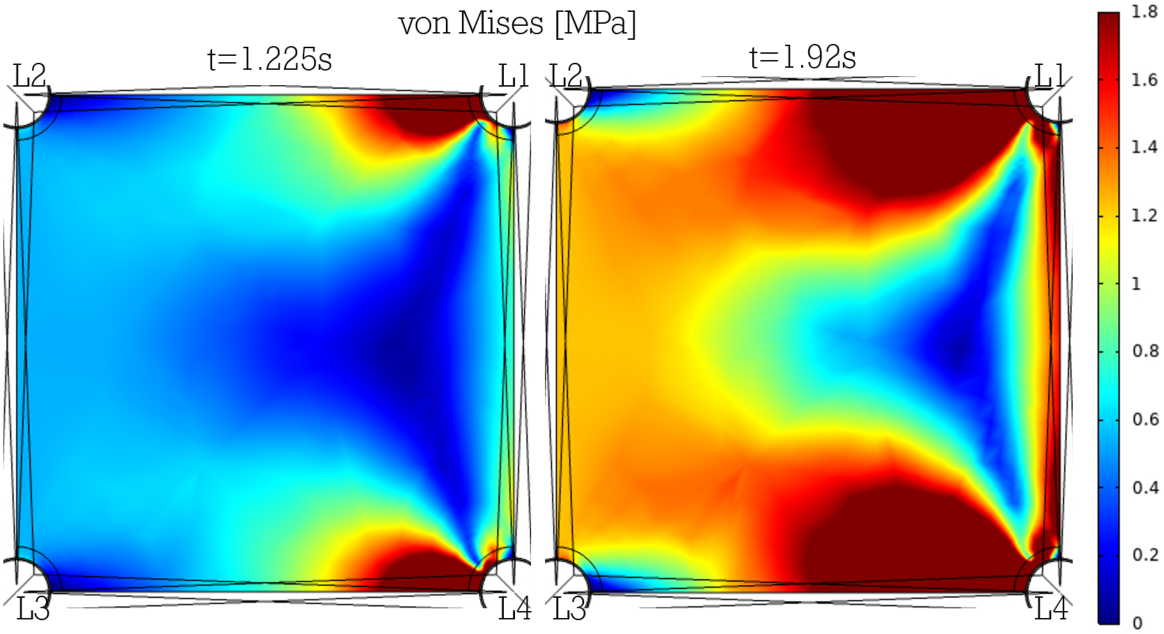

Figure 5.12: Stresses in the internal jam at two time steps with v_{ice}=0.04 [ms^{-1}].

5.3. Frontal Jam

The frontal jams consist of two configurations, scenario A and scenario B which is angled, see Figure 4.12. In scenario A, the structure is in the same position as base case scenario A. Scenario B represents a situation in which it is most likely that an ice jam can be sustained throughout the dynamic interaction and is in the same position as base case scenario B.

Frontal jam scenario A

The frontal jam is blocking the clear path between legs 2 & 3, resulting in an extra ice load on legs 2 & 3. The structural displacements are shown in Figure 5.13 and the von Mises stresses are shown in Figure 5.14. The force-time traces are shown in Figure B.4. The displacement signal contains more irregularities than the base case. The period of the oscillations is longer. The structure stays longer in the intermittent crushing regime. However, it will go to the frequency lock-in regime for the higher ice drift velocities. Where it oscillates around its second natural frequency. Figure 5.14 shows the von Mises stresses of the ice jam at two different time steps for v_{ice}=0.15 [ms^{-1}], which are indicated in Figure 5.13. The left figure shows the stresses when they are at a minimum. The right figure shows the stresses at a maximum. In both situations, the von Mises stresses exceed the ice strength of 1.8[MPa].

Frontal jam scenario B

Scenario B is made to achieve a situation in which it is most likely that the stresses in the ice jam would not exceed its strength. The effective width of the jam is smaller compared to scenario A. Furthermore, the ice jam is twice as thick. The top-view of this scenario can be seen in Figure 4.12b. The structural response is shown in 5.15 and its corresponding force-time traces are shown in B.5. The von Mises stresses in the jam are shown in 5.16. The period of the oscillations is longer, and the time traces contain more irregularities than the base case. The transition between intermittent crushing and frequency lock-in happens around v_{ice}=0.08 [ms^{-1}]. The frequency lock-in regime is again around its second natural frequency. Figure 5.16 shows the minimum and maximum stresses inside the ice jam for v_{ice}=0.08 [ms^{-1}] at 2 points in time, which are indicated in Figure 5.15. Now there is a scenario in which the ice strength is not exceeded. The maximum von Mises stress still exceeds it but the overall stresses are a lot lower. In Figure 5.17 the average von Mises stress at the contact area of the jam is shown, which is at the jam-leg interface. This figure shows that the average stress throughout the contact area is numerous times the ice strength. While for the oblique frontal jam, this is not the case. It should be noted that this is the von Mises stress averaged over the contact surface of the jam. Thus the peak stresses are higher. Nonetheless, it shows the difference between the jams and that the angled frontal jam could be sustained.

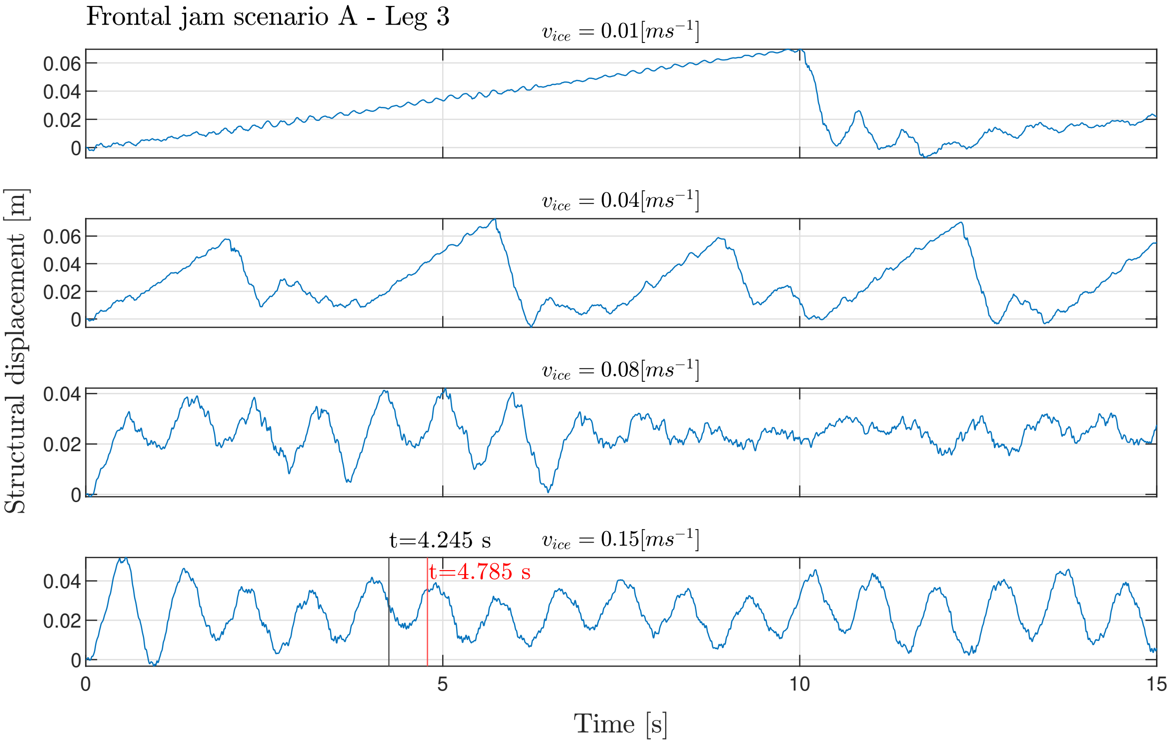

Figure 5.13: Frontal jam scenario A - structural displacement leg 3. The indicated time instances show the moment at which the snapshot is taken that can be seen in Figure 5.14.

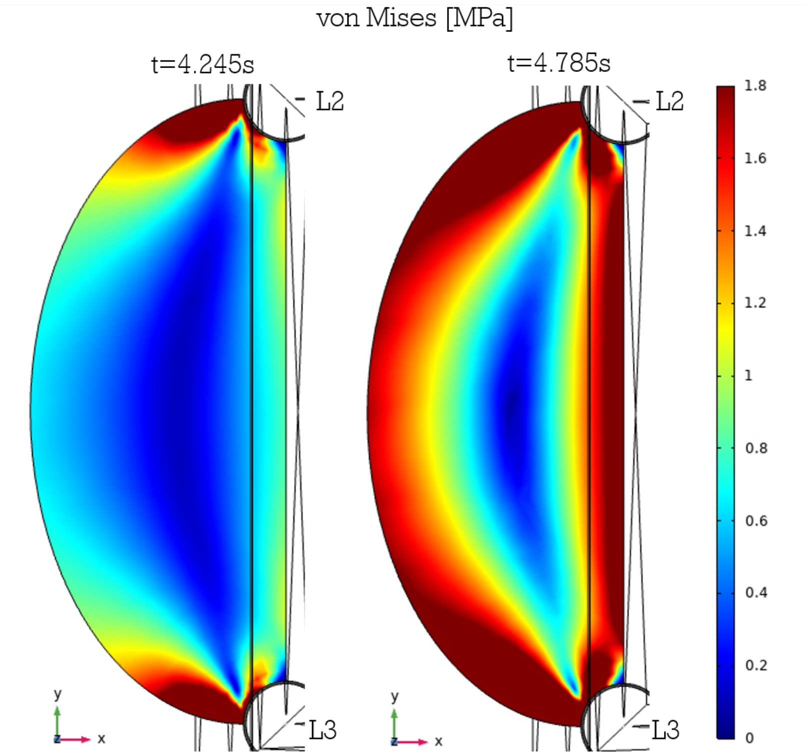

Figure 5.14: Stresses in the frontal jam scenario A at two time steps with v_{ice}=0.15 [ms^{-1}].

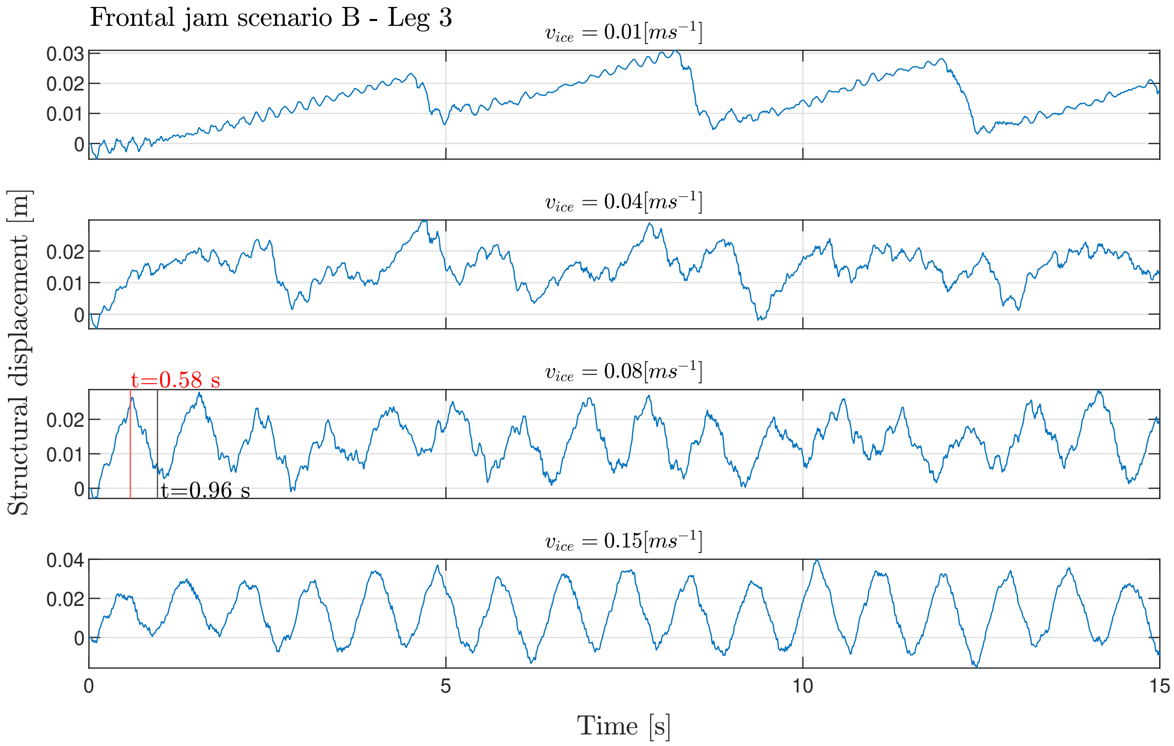

Figure 5.15: Frontal jam scenario B - structural displacement leg 3. The indicated time instances show the moment at which the snapshot is taken that can be seen in Figure 5.16.

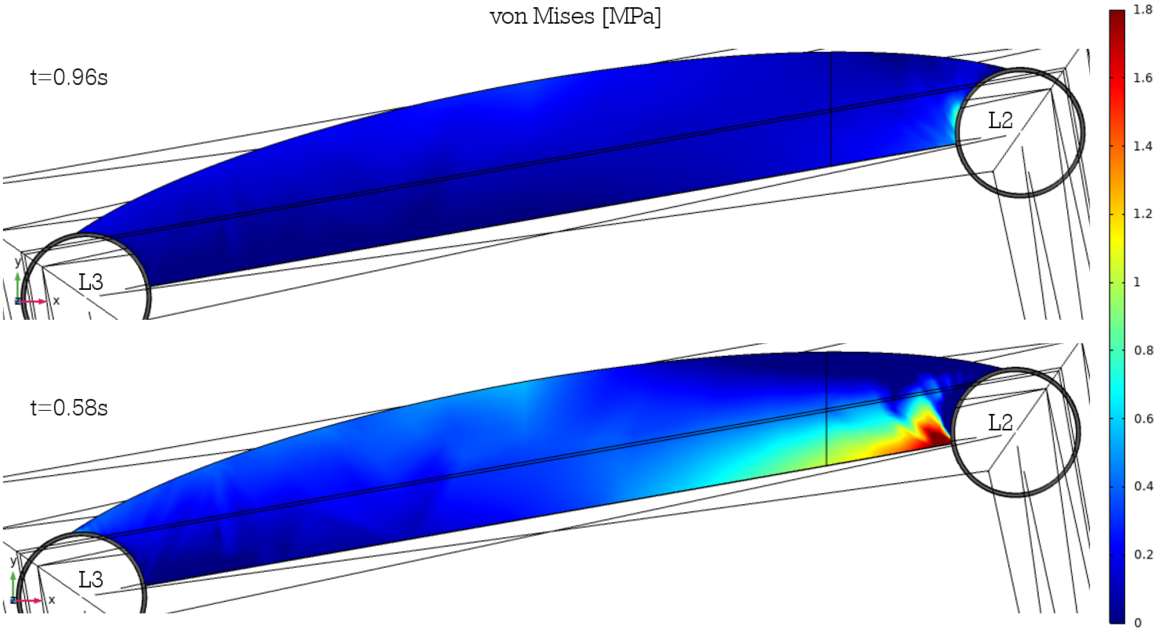

Figure 5.16: Stresses in the frontal jam scenario A at two time steps with v_{ice}=0.08 [ms^{-1}].

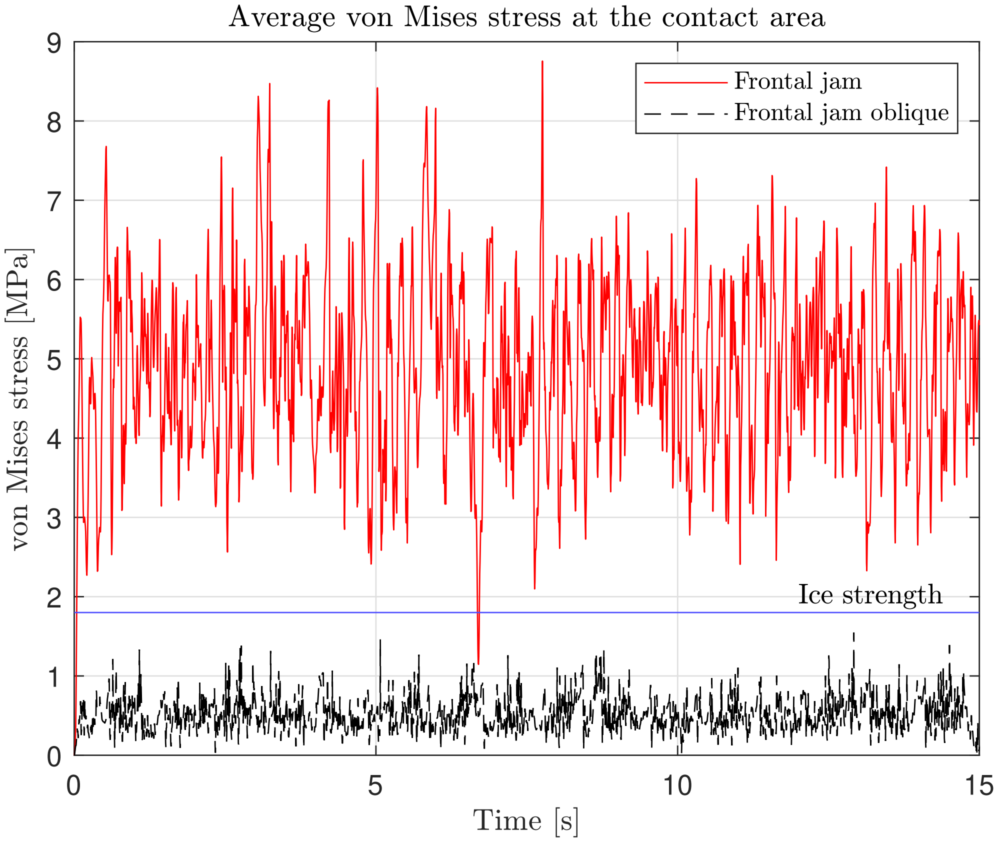

Figure 5.17: Average von Mises stress at the contact area of the ice jam at the jam-leg interface. In red the frontal jam and in black the oblique frontal jam.

6

Discussion

The obtained solution is not fully reliable before it is validated and performs well for different representations of the problem. However, in its current state, it might give some valuable insights for the modelled and simulated scenarios based upon the verification from the literature review. But these solutions should be taken into account with the assumptions and simplifications that were made. In this chapter, the model and the results for the different scenarios will be discussed and looked at from a broader perspective.

Ice Model

The phenomenological model from Hendrikse and Nord (2019) had to be adjusted in order to function with the LiveLink for MATLAB. Due to this connection, it was not possible to use the event detection from the integrated ODE solver in MATLAB. This means that a sufficient small time-step had to be chosen without increasing the computational time too much. Due to the lack of event detection, the ice loads will be underestimated. A time-step of 5E-3 s was found to work best with the simulation duration, solver settings and to remain close to the solution with solver detection.

Structural Model

The structural model was based upon the reference jacket sub-structure from Vorpahl et al. (2011). A few adjustments have been made, but those did not significantly change the eigenfrequency and modal analysis. Although the structure is well documented, some parts were unclear on how they were modelled or their reasoning behind decisions. Those things were the documentation about marine growth, the stiffener parts and the rotor-nacelle-assembly. For marine growth, the guidelines from DNV GL AS were followed. Between -2 and -40 m under MSL, everything was the same, but for further below -40 m under MSL, 50 mm thickness should be added, which in the reference document nothing was said about. The stiffer parts of the substructure, the transition piece and the grouted connection were modelled differently by the different participants from the workgroup. Furthermore, for the RNA assembly only the full model was described/referenced to. Due to limiting the computational power required, the RNA was modelled as a point mass with the mass moment of inertia. However, the exact mass moment of inertia was not specified. First, the RNA was modelled as a solid, and then an eigenfrequency study was performed to find this property. While it is a good approximation, the obtained result will differ from reality. Due to these things, there is a slight difference in the eigenfrequency and modal analysis but not significantly.

Ice jam

The ice jam was assumed to be a linear-elastic material. This was done to simplify the model and to keep the computational cost as low as possible. The contact nodes in COMSOL Multiphysics were extremely computationally expensive. 1s simulation took between 1/1.5 hours to compute. The assumption of a linear-elastic material can be justified because the main objective was the global ice-structure interaction and not the local pressure/stress distribution. Due to this extremely long simulation time, the simulation time of the jammed scenarios had to be cut back to 15 seconds.

6.1. Model Results

The current model shows the global ice-structure interaction for a four-legged jacket sub-structure. It indicates how such a structure would respond with and without an ice jam. The model is not validated. Thus its results have to be looked at in a critical manner, which will be done in this section.

Base cases

The results from the base case show the different aspects observed from the literature study. Intermittent crushing and frequency lock-in regimes are observed for both scenarios. Continuous brittle crushing is only observed for scenario A over the range of simulated ice velocities. Scenario B will experience continuous brittle crushing for higher ice velocities when the frequency of ice failure is not in the same range as its eigenfrequency. The displacement frequency spectrum shows that the structure is oscillating at its second eigenfrequency for the frequency lock-in region, resulting in large structural displacements. The structure stays in this regime for a significant range of ice drift velocities, 0.06 - 0.2 ms^{-1}, for scenario A. And until 0.3 ms^{-1} for scenario B. The angle between incoming ice and structure can explain this difference. In scenario B, all the legs are loaded, while only the front legs were loaded in scenario A. This results in a higher total global ice load on the structure. Due to this extra load, the structure will be longer in the frequency lock-in regime. The displacement of the structure in scenario B is higher for intermittent crushing, but the amplitudes are roughly the same for the frequency lock-in regime. This is visible in Figure 5.10. The maximum global ice load on a single leg increases for higher ice drift velocities because scenario A is no longer in the frequency lock-in regime. Thus there is no periodical amplification of the ice load ensuing the time when the relative velocity is low. The mean ice load stays roughly the same. The maximum structural velocity is higher at lower ice drift velocities and equal inside the frequency lock-in regime. When the structure from scenario A drops out of the frequency lock-in regime, the differences in structural velocity are substantial.

Base case vs. internal jam vs. frontal jam (scenario A)

The structural response from the jammed scenarios is significantly higher at lower ice velocities compared to the base case. This is because the total global ice load on the structure is higher for these jammed scenarios. The amplitude of the oscillations at 0.15ms^{-1} is roughly the same. However, the pressure inside the jam exceeds the ice strength at all times. Even at the beginning of the simulation, the peak stresses in the jam rapidly exceed the ice strength. The jam fails at the build-up phase of the force, and the total load is simply too high for such a small contact area with the legs. Thus the jam is not sustainable and will fail on crushing at the corners where it is in contact with the structure, resulting in clearance of the ice jam. The main difference between the frontal jam and the internal jam is that for the frontal jam only the frontal legs are loaded, while for the internal jam all four legs are loaded. This results in an increase in displacement for the frontal legs, for the intermittent crushing regime. But for the frequency lock-in regime the structural displacement oscillates with the same amplitude.

Frontal jams

Two different scenarios are tested with frontal jams. Scenario B shows that it is possible that an ice jam can hold. The increased thickness reduces the stresses around the contact point area with the leg and the angle lowers the global ice load on the jam. The maximum internal stresses do exceed the ice strength. However, the area is small and with the assumptions, hence it cannot be stated that the jam will fail. See Figure 5.17 for the difference in average von Mises stress at the contact area. Note that this is the average von Mises stress. Ice rubble or crushed ice that has been formed due to internal stresses exceeding ice strength will be between the jam and structure. Thus can contribute to a larger contact area, resulting in a decrease in local stresses. In the beginning there will be some failure and crushing of the ice at the jam-structure interface, but then the crushed ice might accumulates and possible distributes the force over a larger area, resulting in lower internal stresses. Increasing the likelihood that the ice jam will sustain.

Base case vs. frontal jam (scenario B)

The scenario B simulations show some interesting results. The structural response is different with jam than without, seeing Figures 6.1 and 6.2. The structural amplitude at intermittent crushing is lower for the ice jam than the base case, while being similar for the the frequency lock-in regime. Although the structural frequency seems to be higher for the base case than the jammed case in the frequency lock-in regime. The total global ice load, thus the ice load summed over the 4 legs or 3 legs and jam, is plotted over the simulation duration in Figure 6.3. For the jammed scenario a higher average global ice load is expected because the total contact width is increase by half the diameter of one leg. The effective width of the jam is roughly 1.5 times the width of one leg.

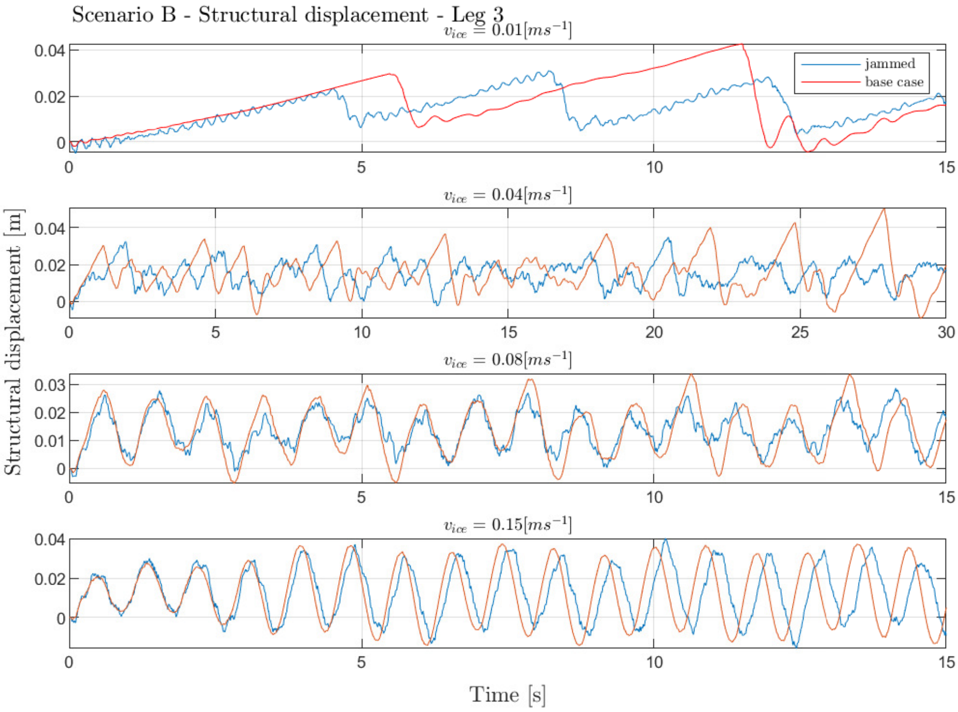

Figure 6.1: Scenario B - leg 3 structural displacement for both scenarios.

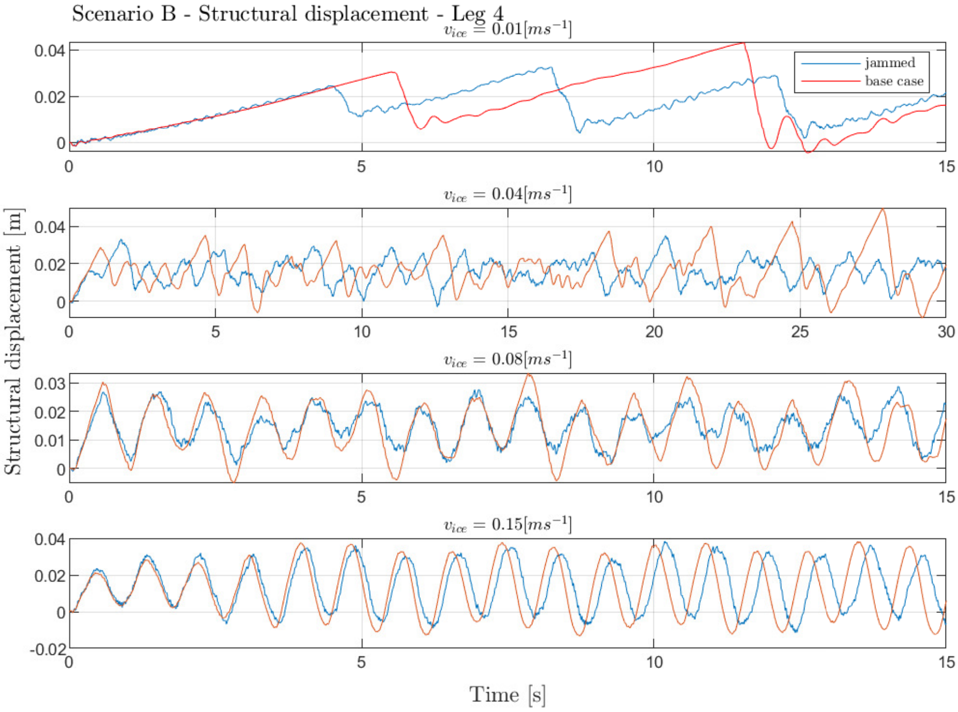

Figure 6.2: Scenario B - leg 4 structural displacement for both scenarios.

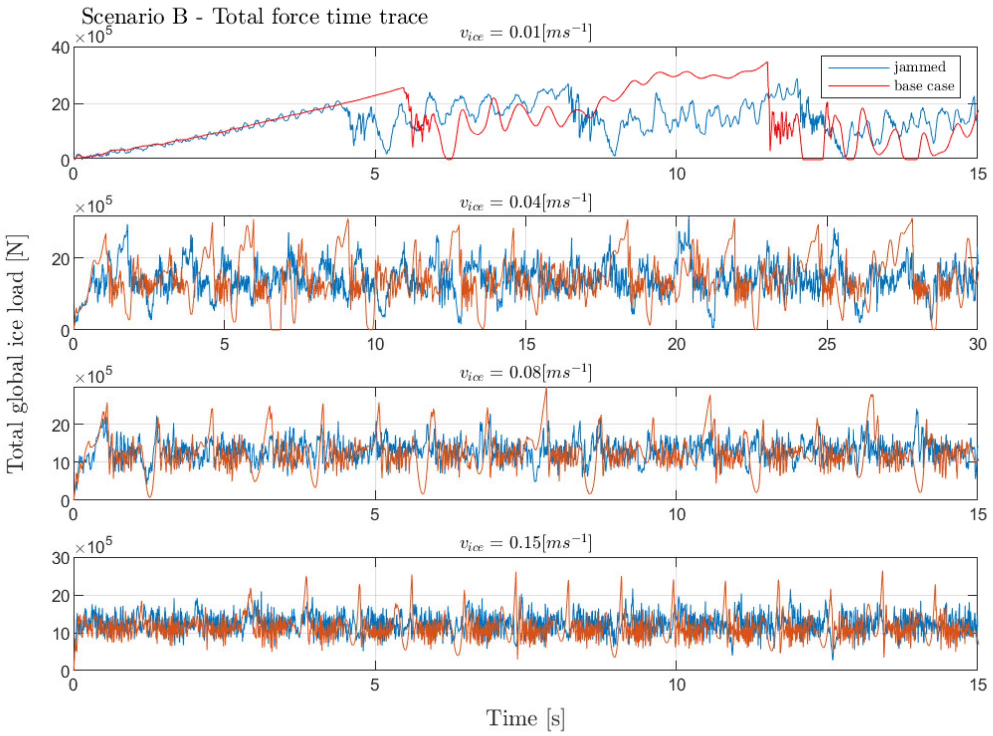

Figure 6.3: Total global ice load on the structure for scenario B. Red is the base case and blue is for the oblique jammed case.

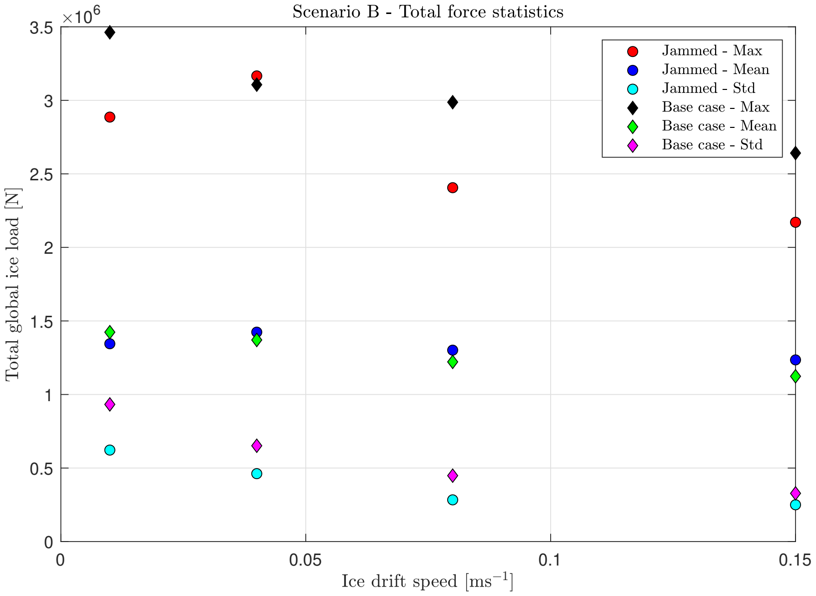

Figure 6.4: Statistics of the total global ice load on the structure for scenario B. Calculated using the data shown in Figure 6.3.

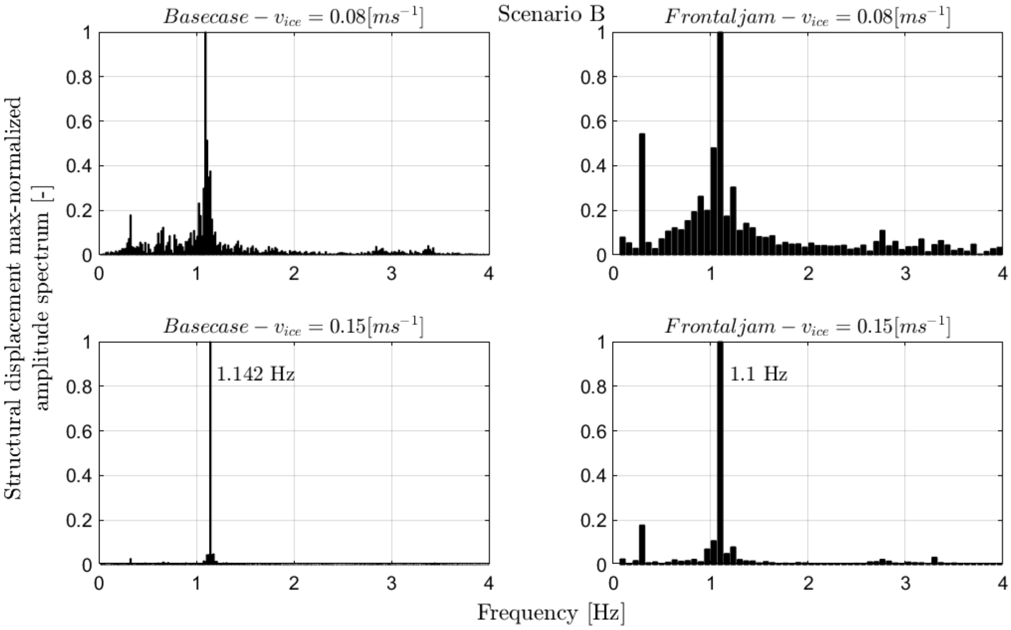

Figure 6.5: Base case scenario B vs frontal jam scenario B - max-normalized frequency spectrum structural displacement leg 3.

The statistics of Figure 6.3 are shown in Figure 6.4. The statistics for the first ice drift velocity, 0.01 ms^{-1} are only based on 2 to 3 oscillations. Thus these are not fully representative due to the impact of the initial excitation. The other drift velocities have more oscillations thus the statistics are less influenced by just one oscillation. Although it would be preferred to use 60s in the second half of an 120s simulation. As expected the mean global ice force is higher for the jammed situation than the base case, due to the wider effective width. Interestingly, the maximum global ice load is higher for the base case than the jammed case. When looking closer at the global ice load plotted over time, Figure 6.3, more 'higher spikes' are visible for the base case. These are periods where the velocity of the structure is near the ice drift velocity and the global force is amplified. This results in a higher maximum load on the structure. While the average ice force is thus lower. This can be explained due to the added stiffness of the ice jam. Resulting in a lower amplitude of the structural response and a slightly different frequency.

In Figure 6.5 the frequency spectrum of the structural displacement is shown for the base case and the frontal jam. It confirms that the frequency for the frontal jam is lower than the base base. Unfortunately, due to the small simulation time span the obtained data for the frontal jam is too little to be able to say something about it in a statistical way.

The ice jam seems to be adding extra stiffness to the structure. Since it is located in between leg 2 & 3, the question rises: how does this effect the relationship between leg 2 & 3? Figure 6.6 shows the structural displacement of leg 2 & 3 for the jammed scenario and base case. Figure 6.7 shows the difference between leg 2 & 3. The impact of the ice jam is noticeable. For the base case the difference in displacement is roughly constant while for the jammed case it is fluctuating a lot more. These fluctuations can be explained by that the jam is transferring loads from leg 3 into leg 2. Thus increasing the force on leg 2. Furthermore, leg 2 will 'push' back on the jam and thus leg 3 when leg 2 is bouncing back, resulting in a difference closer to zero.

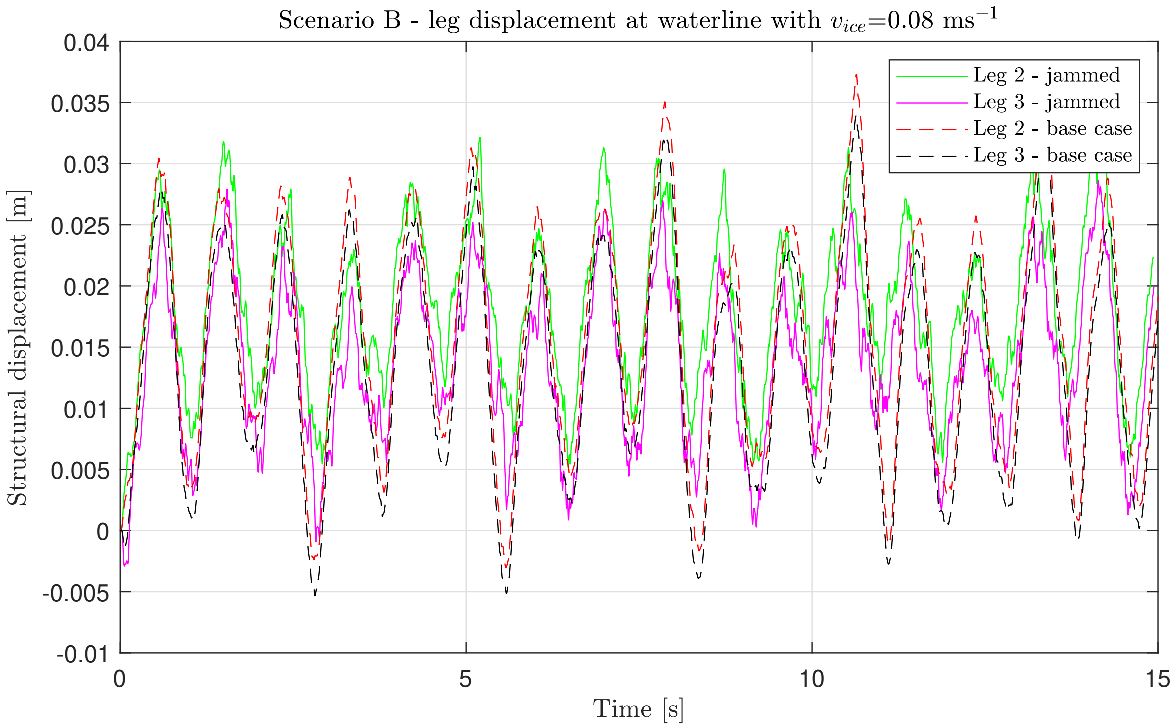

Figure 6.6: Scenario B - leg 2 and 3 structural displacement for both scenarios

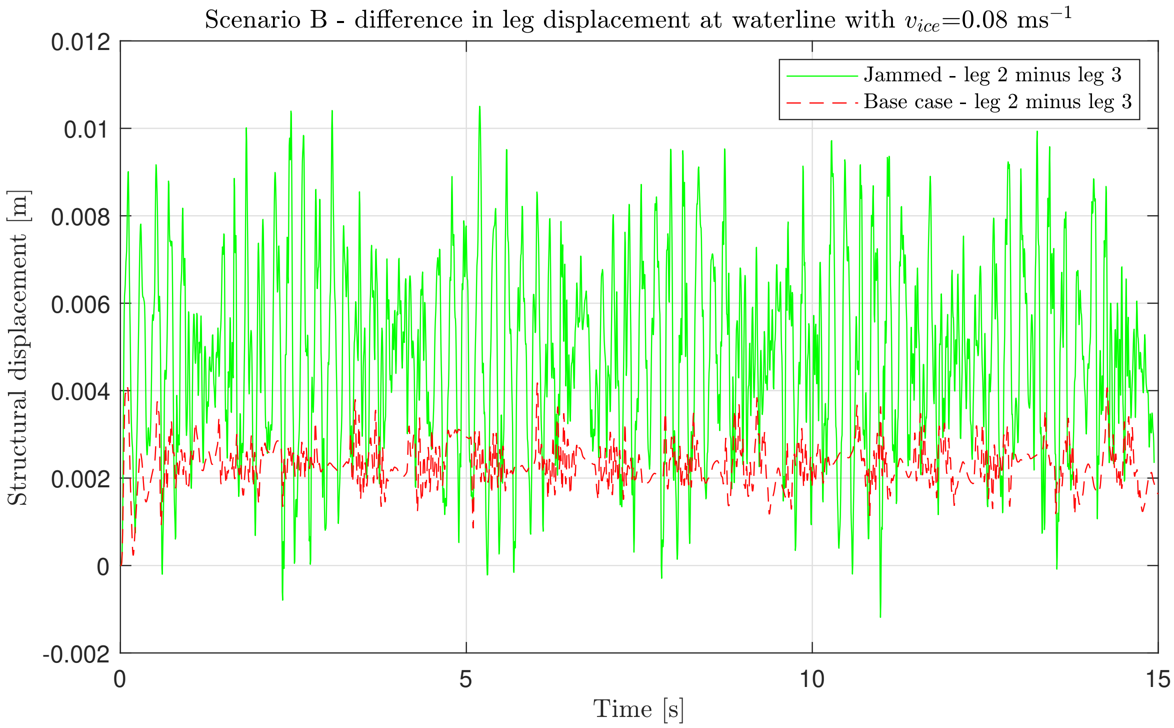

Figure 6.7: Scenario B - difference in structural displacement between leg 2 and 3 for both scenarios

6.2. Model observations

The first thing to point out about the solver/COMSOL Multiphysics is that the solver duration is extremely long to the contact nodes. Which resulted in a short simulation span of 15 seconds for the jammed cases. For such a short simulation time the initial disturbance and excitation is not fully damped yet. The influence of the transient phase is influencing the response of the structure which is shown. A simulation duration of at least 120 seconds would give better data for statistical analysis. Secondly the computation time makes it hard to do quick changes and check their influence. The simulations of 15s for the frontal ice jam scenario B took between 20 to 30 hours to compute. For the base case scenarios this was faster with 1.5 hours for the 120s simulation. This made it impossible to change a few things and run a quick simulation to see its effects. At last the contact nodes from COMSOL Multiphysics are susceptible to contact and solver settings. Without validation it is difficult to chose the right settings.

The Wikinger jacket has no braces around the MSL and the global ice load will act in the middle of a vertical member instead of one a node, as is the case with this model. In real design situations the MSL is not a single value, but rather a range due to low, high tide and storm surges. This will result in a range of the jacket which will be suspectible for ice loading. If the diagonal braces were to be close to the waterline as is the case for this model, then during low or high tide the contact area will be significant increase, leading to an increase in global ice load and perhaps ice will build up due to the lack of clearance as well.

The structure is rotated with angle α and all the four legs are in contact with the incoming ice floes. Currently splitting is not taken into account, however splitting can happen at the indicated lines in Figure 4.10b and 4.12b. This would reduce the load on the rear legs significantly and thus decreasing the maximum displacement. Because the total global ice load will be reduced the structure will transition sooner to the continuous brittle crushing regime.

An increase in total global ice load seems to only increase the structural displacement for the intermittent crushing, for scenario A. Once the structure is oscillating at its second eigenfrequency the amplitudes converge to the same value for the same ice drift velocity, even if the total global ice load is substantial more. This can be explained by the excitation force. The incoming ice floe is exciting the structure and this motion is limited by the velocity of the ice floe. For the oblique jam (scenario B), at higher ice drift velocities, the amplitudes stay the same but the frequency is slightly higher compared to the base case. Furthermore, the peak force is higher for the base case than the jam case. The force trace of the jammed case has less periods were the force is amplified and this amplitude is also smaller than the base case. Thus the jammed case transitions into the continuous brittle regime faster.

In the literature the only used ratio is the ratio between the center of the legs or clear distance between the legs and the diameter/width of the legs. However, as can be seen from the frontal jam under an angle, it is also important to take this into account. Also, the scale of the problem is important. Ice thickness will influence a lot of the ice properties and should thus be taken into account for ice jams. Different jams can be initiated, and it will be easier for a broken piece of rafted ice to jam a 3 m span versus a 10 m span, even if the Q/D ratio is the same.

7

Conclusion

In this study, research was conducted on the influence of an ice jam on the ice-induced vibrations of an multi-legged sub-structure. First a literature study was performed into ice-induced vibrations and ice jams, which was concluded in Chapter 3. Then a model was made based upon the phenomenological model developed by Hendrikse (2017) and the reference jacket for the NREL 5-MW turbine (Vorpahl et al., 2011). The structural response was modelled/simulated in COMSOL Multiphysics with the LiveLink for MATLAB extension to calculate the global ice load per leg and for the ice jam in MATLAB. The results in Chapter 5 show the global ice-structure interaction for the jacket sub-structure with an ice jam. The formulated research questions can now be answered:

"What is the pressure distribution of an ice jam on the legs of a multi-legged sub-structure?"

The main pressure and thus highest stresses will be parallel with the incoming ice drift on the frontal side of the legs (the point of initial contact), which are connected with the jam, as can be seen in Figures 5.12, 5.14 and 5.16. In other words, the area where the jam is pushed into the leg has the highest stresses compared to the sides of the leg, where the jam is sliding along the leg. Furthermore, the stress field develops mainly around the edges of the ice jam for the internal and frontal jam as can be seen in the figures. The oblique jam is in between leg 2 & 3, resulting in high stresses on both sides of the jam. Sometimes it is getting 'squeezed' in between both legs.

"How does an ice jam influence ice-induced vibrations of a multi-legged sub-structure?"

An ice jam can severely impact the ice-induced vibrations of a multi-legged sub-structure. For the internal and the frontal ice jam (scenario A), the structural displacements are significantly higher compared to the base case and the total global ice load on the legs is significant higher as well. However, the question should be whether or not the jam is sustainable. Figures 5.12 and 5.14 show that this is clearly not the case and that the jam will fail, even in the situations were the jam is the least stressed, the stresses are still above the ice strength. The frontal jam under an angle, which was thought of as a scenario were the ice jam was most likely to sustain. Shows in Figure 5.16 that it is indeed possible to sustain. There are small areas above the ice strength but this is not significantly enough to say that the whole jam will certainly fail. Ice rubble or crushed ice that has been formed due to internal stresses exceeding ice strength will be between the jam and structure. Thus can contribute to a larger contact area, resulting in a decrease in local stresses. In the beginning there will be some failure and crushing of the ice at the jam-structure interface, but then the crushed ice might accumulates and possible distributes the force over a larger area, resulting in lower internal stresses. Increasing the likelihood that the ice jam will sustain. The structural response from this jam, as shown in Figure 5.15, shows that the structural displacement en its oscillations are less severe compared to the base case, Figures 5.6 - 5.9. The displacement and force comparison is shown in Figures 6.1 - 6.4. Resulting in the main conclusion that an ice jam which would significantly impact the ice-induced vibrations cannot be sustained and for the ice jam which can be sustained, it will act as additional stiffness for the system and decreases the structure's displacement amplitude. In the frequency lock-in regime the displacement amplitude is roughly the same but the frequency is a bit higher for the oblique jam scenario.

8

Recommendations

As discussed in Chapter 6, there are many assumptions used throughout the study. Only three different jammed scenarios were taken into account. A longer simulation time would be desirable. Solver settings that could not be verified. Resulting in uncertainties within the results. These results have led to the conclusion written in Chapter 7. This chapter proposes areas to be further investigated with the newly obtained knowledge from this study:

- Adjust the support structure to a jacket used in icy waters, with no braces around mean sea level. Alternatively, check the impact of braces around the mean sea level.
- What happens when the size of the jacket decreases significantly? Is it possible that the frontal and internal jam is sustainable then, and does this impact the structural vibrations the same as the oblique frontal jam from this study?
- Use a hydrostatic material model such as Mohr-Coulumb or Drucker-Prager for the ice jam to simulate a more 'real' situation.
- Run the simulations for the oblique frontal ice jam a lot longer (120-200s) to get more statistical significance if indeed the oscillations are less severe and that the period decreases.
- Instead of assuming the jammed scenario, use a certain ice concentration and test the likelihood of jamming in between the legs.
- Validate the model through model testing in an ice basin. Jam a multi-legged structure and pull it through an ice sheet while measuring the reaction force and structural vibrations.

A

Leg displacement at waterline

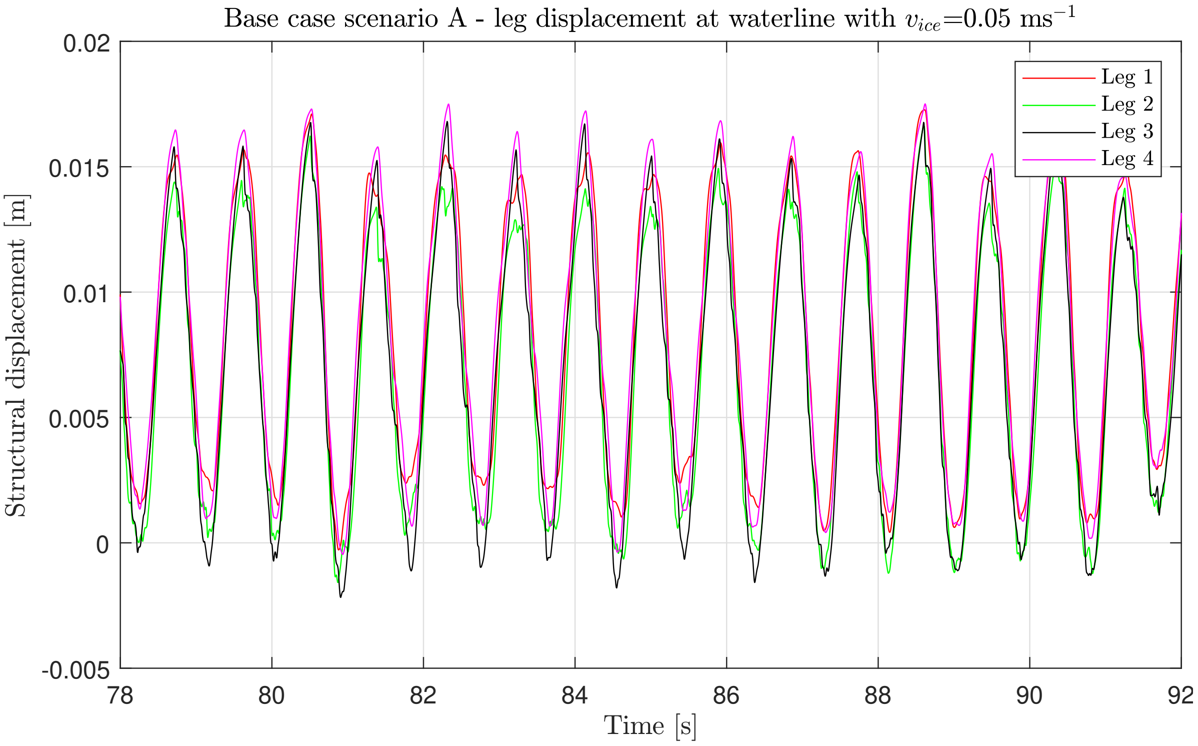

Figure A.1: Base case scenario A - structural displacement at waterline with v_{ice}=0.05 ms^{-1}.

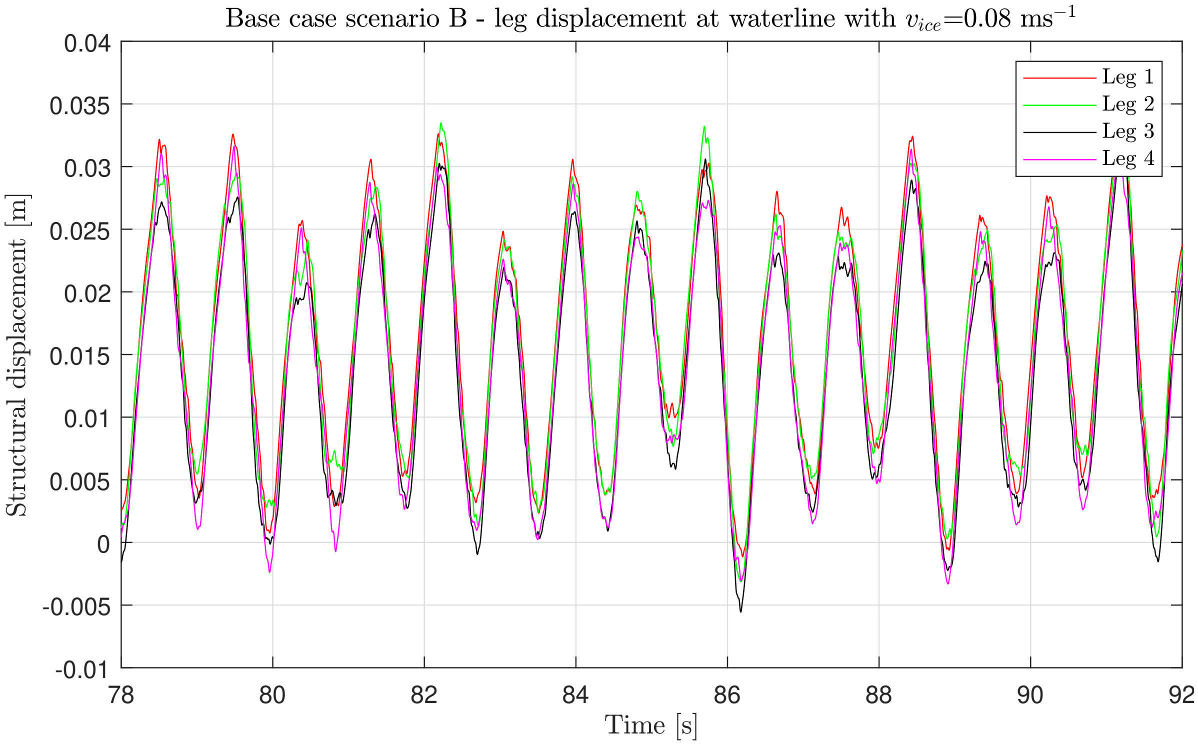

Figure A.2: Base case scenario B - structural displacement at waterline with v_{ice}=0.08 ms^{-1}.

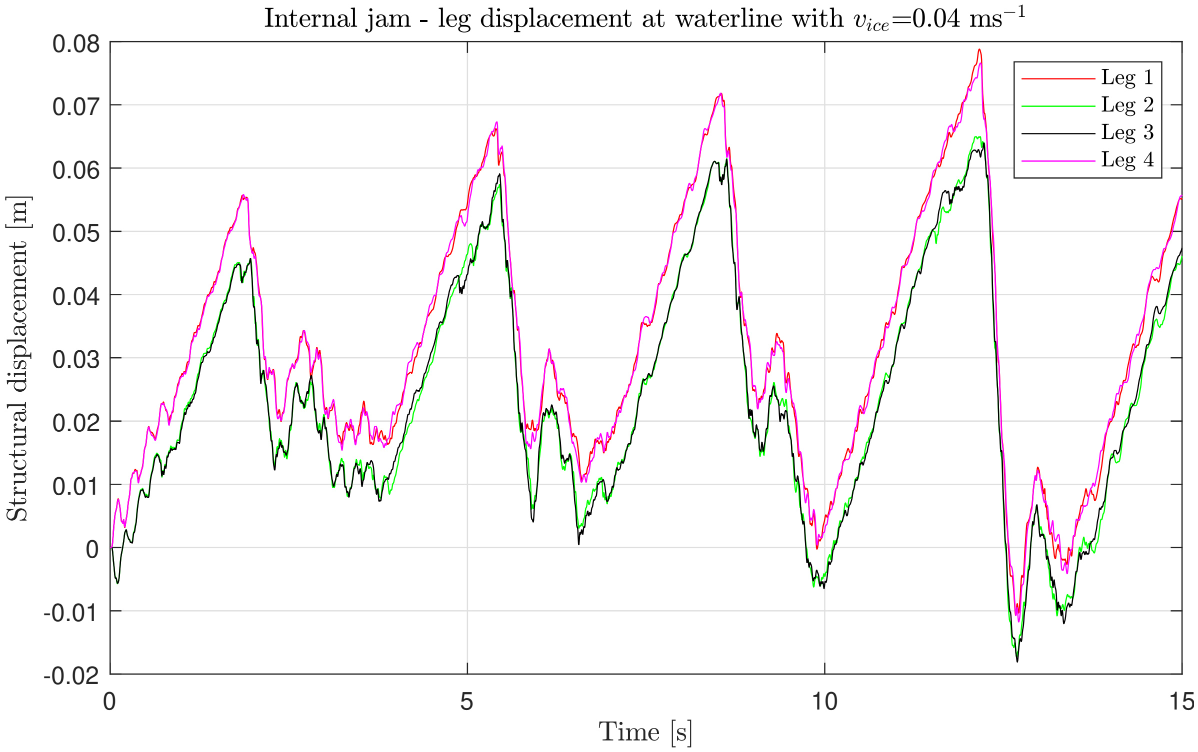

Figure A.3: Internal jam - structural displacement at waterline with v_{ice}=0.04 ms^{-1}.

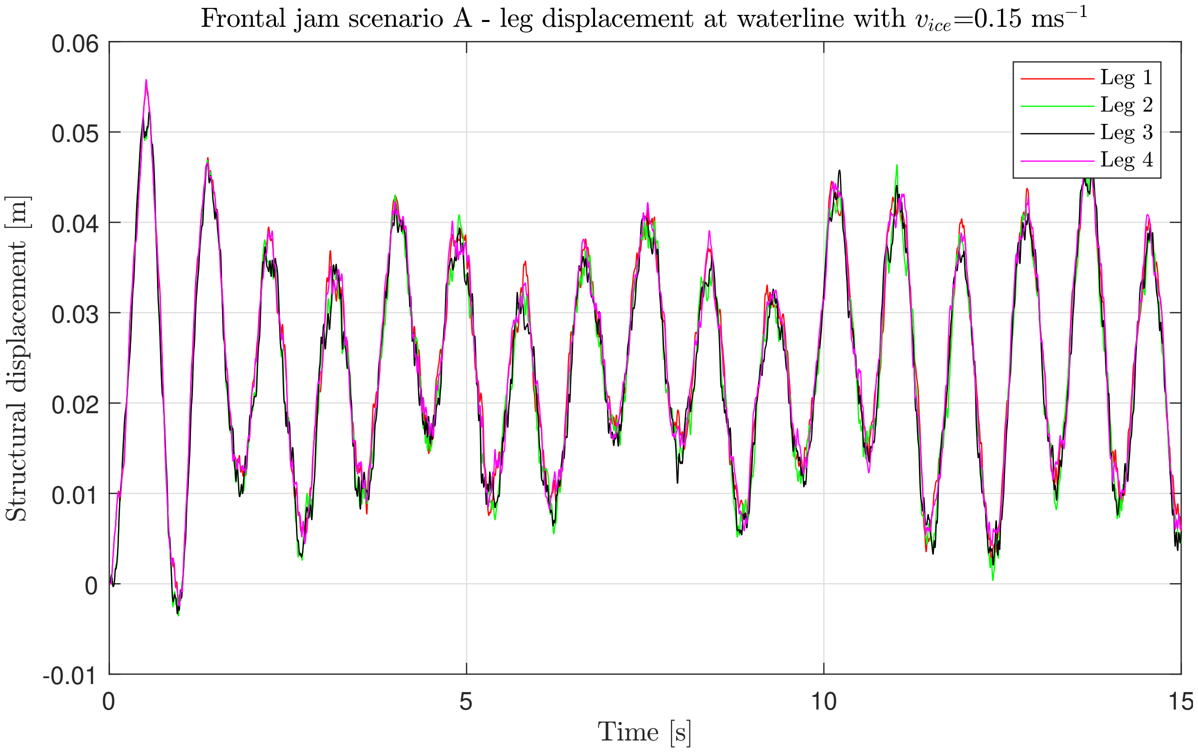

Figure A.4: Frontal jam scenario A - structural displacement at waterline with v_{ice}=0.15 ms^{-1}.

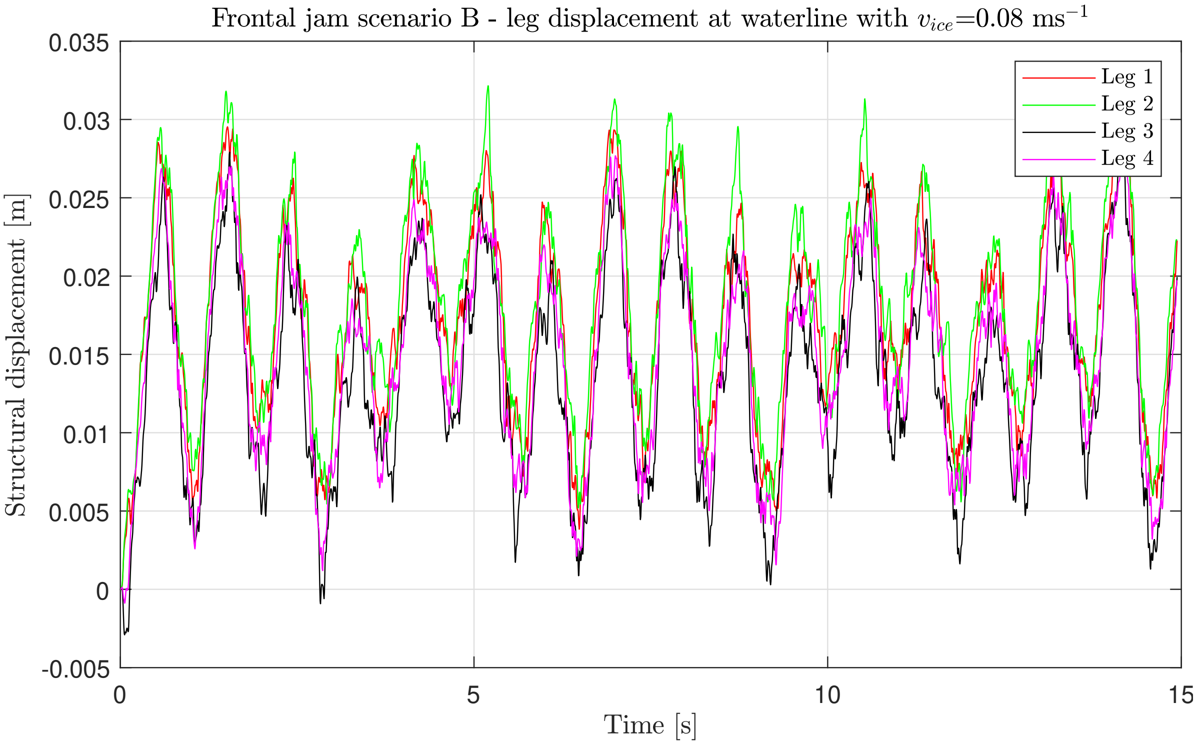

Figure A.5: Frontal jam scenario B - structural displacement at waterline with v_{ice}=0.08 ms^{-1}.

B

Force-time traces

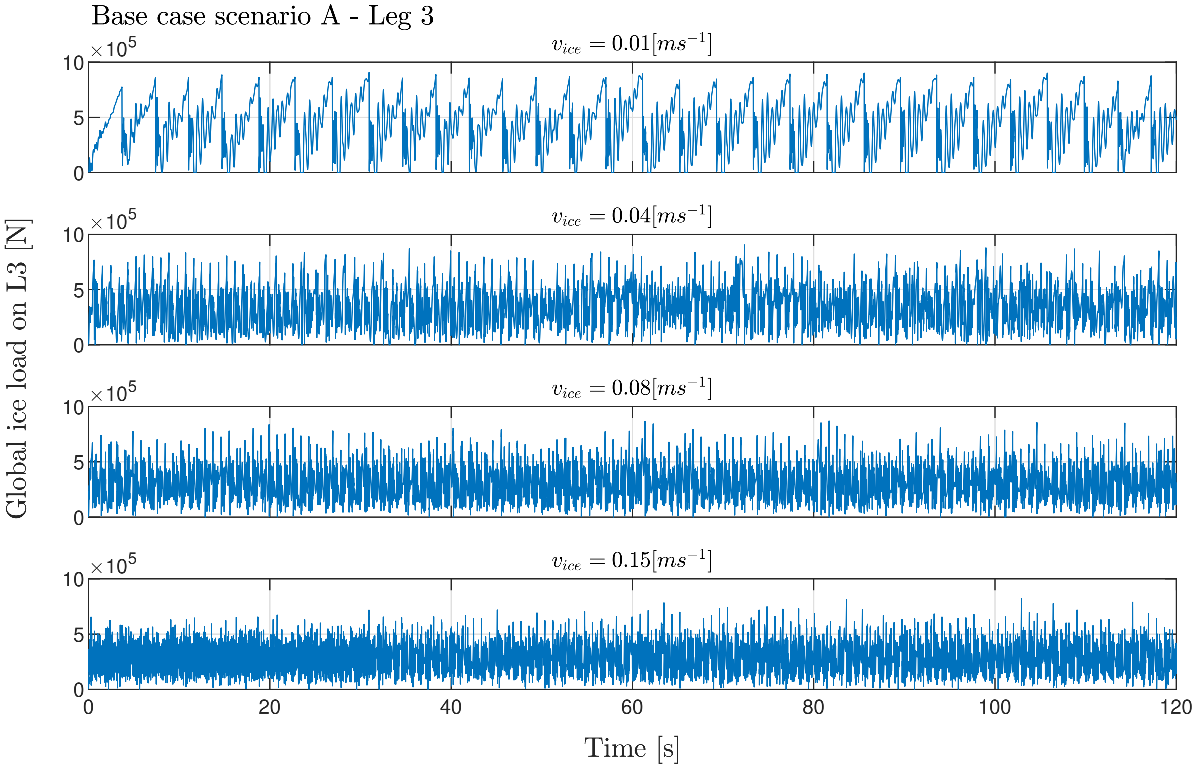

Figure B.1: Base case scenario A - force time traces.

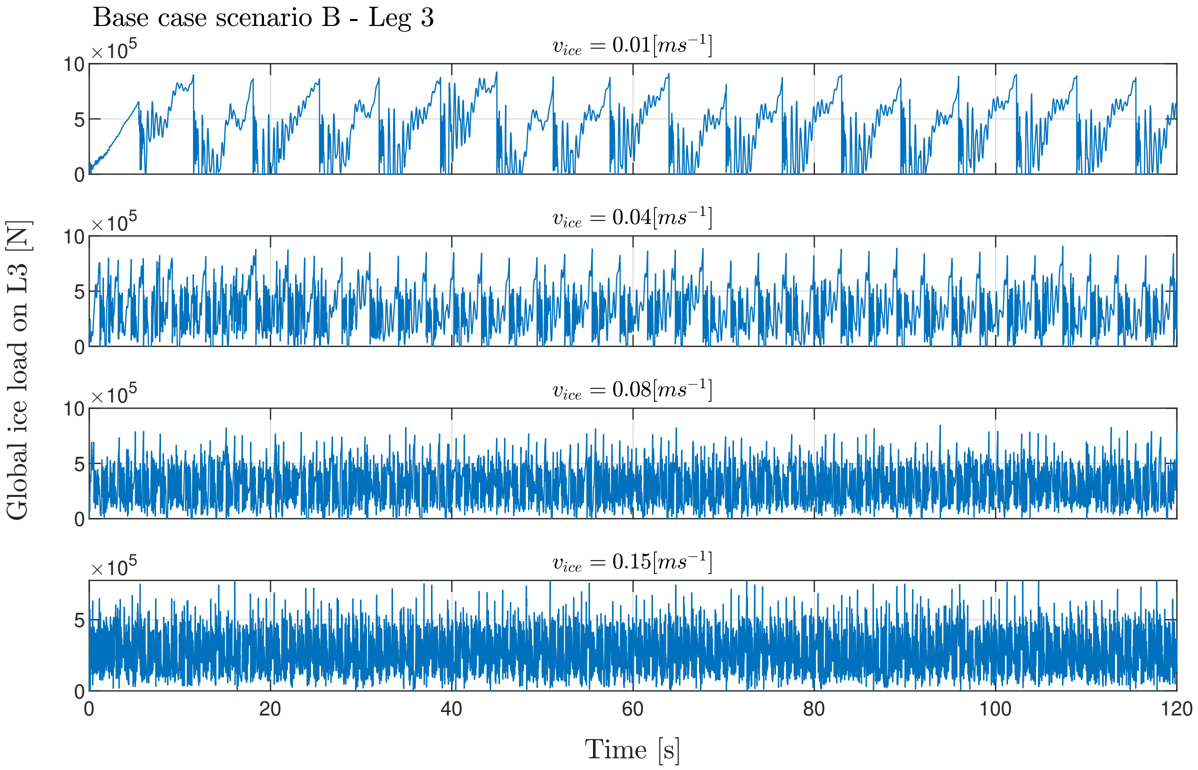

Figure B.2: Base case scenario B - force time traces.

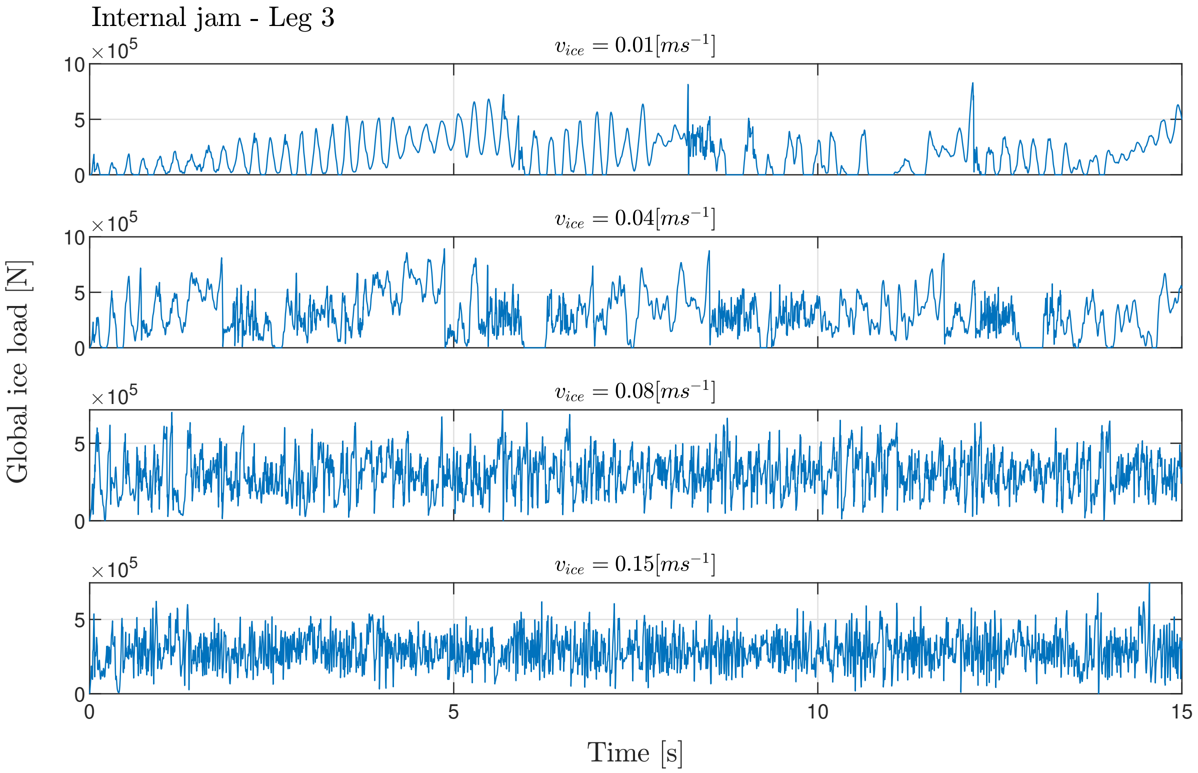

Figure B.3: Internal jam - force time traces.

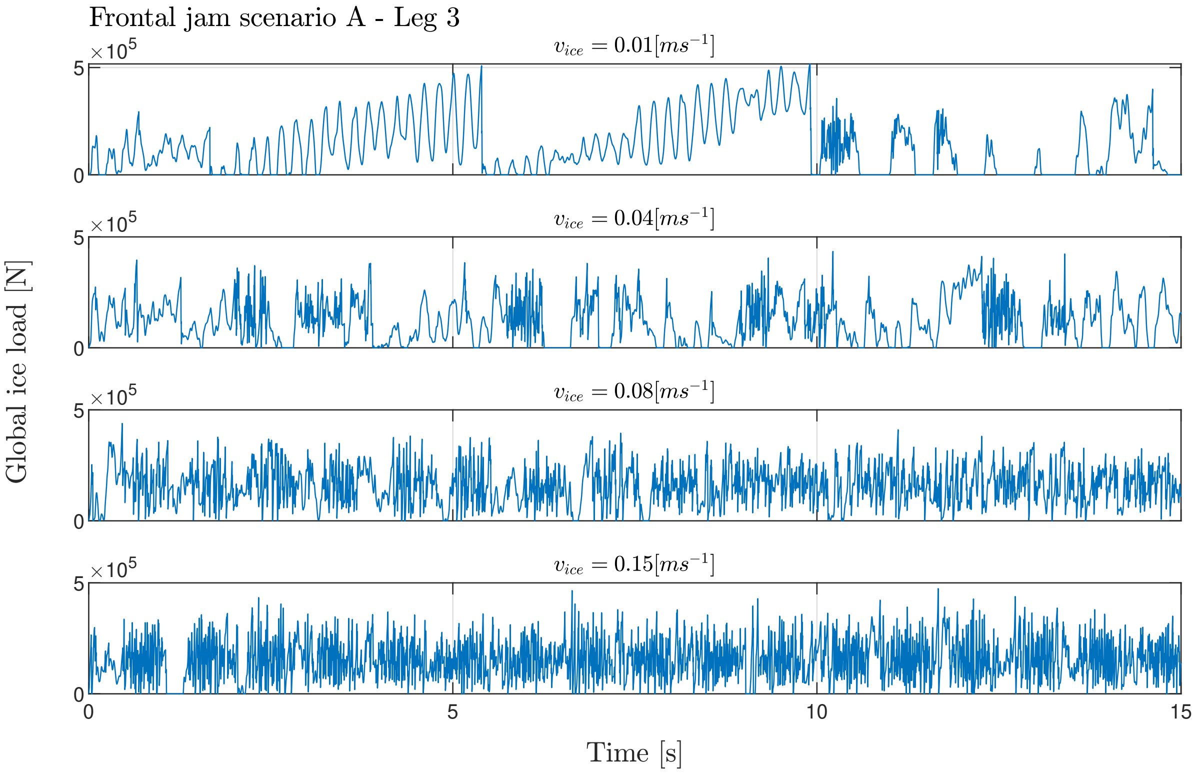

Figure B.4: Frontal jam scenario A - force time traces.

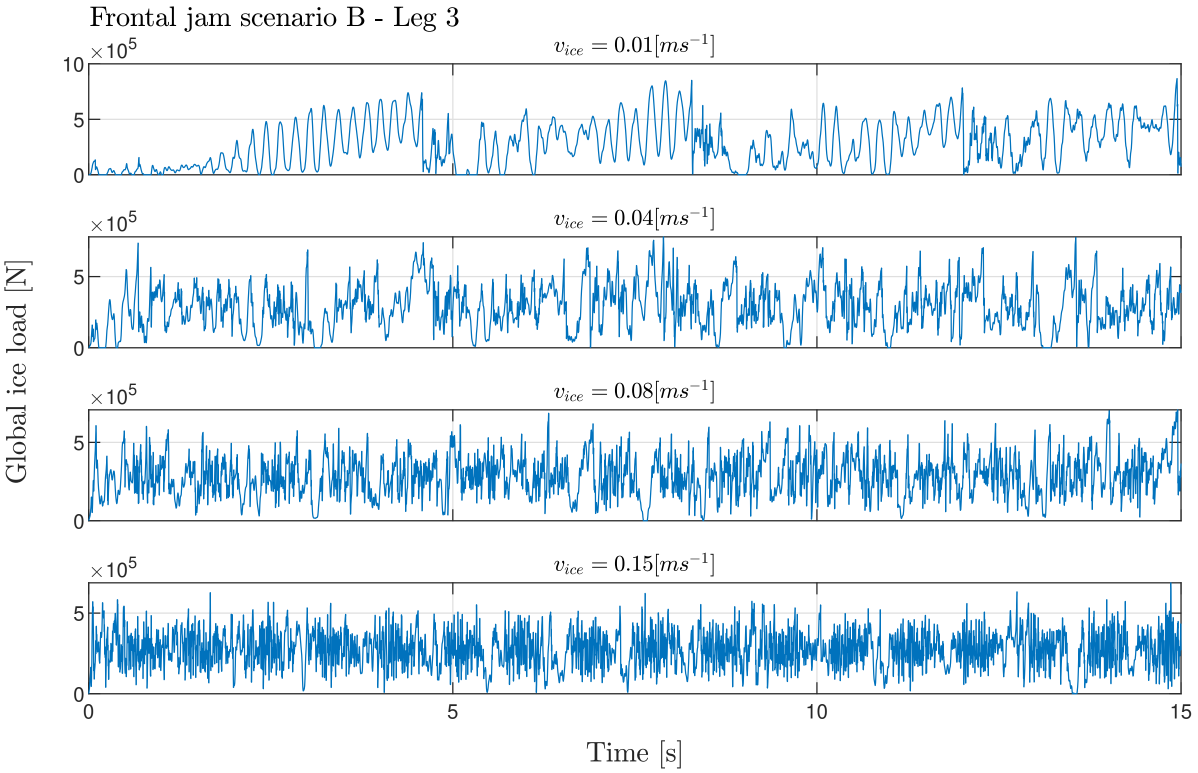

Figure B.5: Frontal jam scenario B - force time traces.

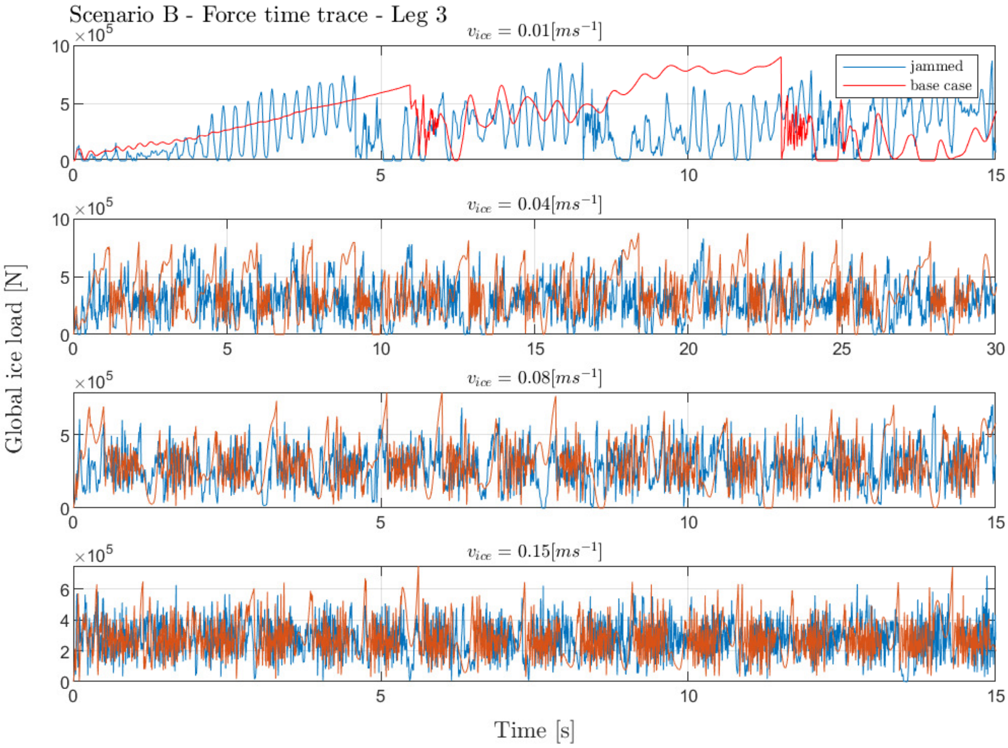

Figure B.6: Scenario B - leg 3 force time traces for base case and jammed case.

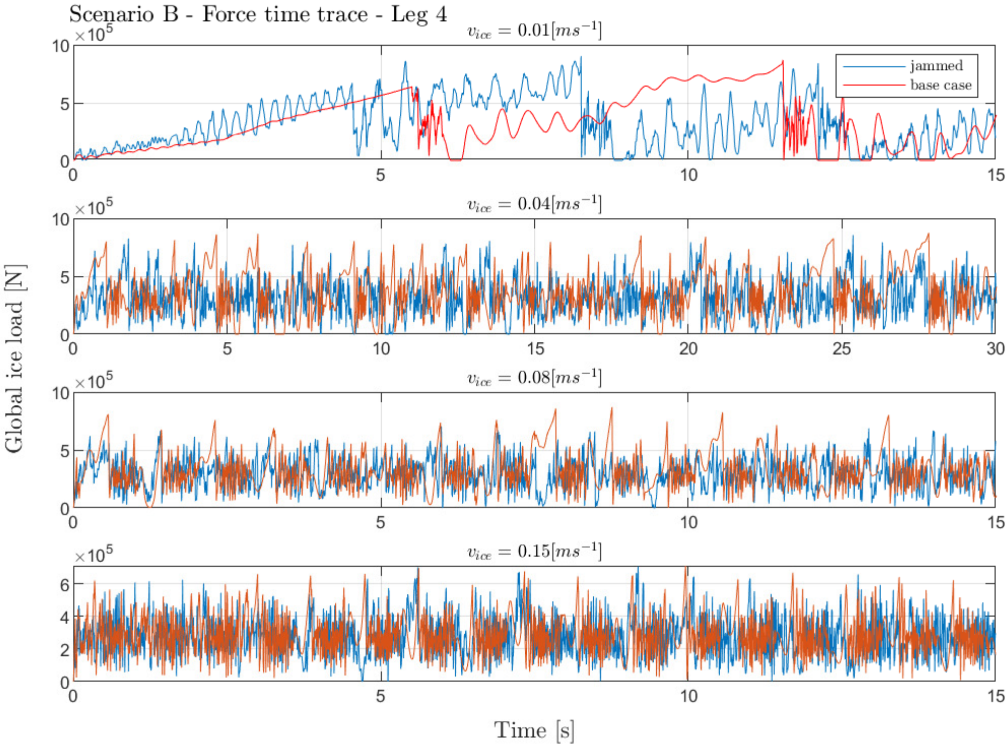

Figure B.7: Scenario B - leg 4 force time traces for base case and jammed case.

Bibliography

Arakawa, K. (1954). Studies on the freezing of water (ii): Formation of disc crystals. , 4(5):311–340.

Ashton, G. D. (1986). River and lake ice engineering. Water Resources Publication.

Beltaos, S. (1995). River ice jams. Water Resources Publication.

Bilgili, M., Yasar, A., and Simsek, E. (2011). Offshore wind power development in europe and its comparison with onshore counterpart. Renewable and Sustainable Energy Reviews, 15(2):905–915.

Caduff, M., Huijbregts, M. A., Althaus, H.-J., Koehler, A., and Hellweg, S. (2012). Wind power electricity: the bigger the turbine, the greener the electricity? Environmental science & technology, 46(9):4725–4733.

Calkins, D. J. and Ashton, G. D. (1975). Arching of fragmented ice covers. Canadian Journal of Civil Engineering, 2(4):392–399.

COMSOL (2018a). LiveLink for MATLAB User's Guide. Retrieved from https://doc.comsol.com/5.4/doc/com.comsol.help.llmatlab/LiveLinkForMATLABUsersGuide.pdf.

COMSOL (2018b). Structural Mechanics Module User's Guide. Retrieved from https://doc.comsol.com/5.4/doc/com.comsol.help.sme/StructuralMechanicsModuleUsersGuide.pdf.

COMSOL (2019). COMSOL Multiphysics Reference Manual. Retrieved from https://doc.comsol.com/5.5/doc/com.comsol.help.comsol/COMSOL_ReferenceManual.pdf.

de Vries, W., Vemula, N. K., Passon, P., Fischer, T., Kaufer, D., Matha, D., Schmidt, B., and Vorpahl, F. (2011). Final report wp4. 2: Support structure concepts for deep water sites. UpWind D4, 2.

Deville, S. (2008). Freeze-casting of porous ceramics: a review of current achievements and issues. Advanced Engineering Materials, 10(3):155–169.

DNV (2014). Design of offshore wind turbine structures. Technical report, Det Norske Veritas GL AS.

European Commission (2019). The European Green Deal. European Commission Report No. COM/2019/640 final. Retrieved from https://eur-lex.europa.eu/legal-content/EN/TXT/?uri=CELEX:52019DC0640.

European Commission (2020). An EU Strategy to harness the potential of offshore renewable energy for a climate neutral future. European Commission Report No. COM/2020/741 final. Retrieved from https://eur-lex.europa.eu/legal-content/EN/TXT/?uri=CELEX%3A52020DC0741&qid=1616581762709.

European Environmental Agency (2020). Total greenhouse gas emission trends and projections in Europe. CLIM 050/CSI 010. Published 18 Dec 2020. Retrieved from https://www.eea.europa.eu/data-and-maps/indicators/greenhouse-gas-emission-trends-7/assessment.

Eurostat (2020). Renewable energy statistics. Retrieved from https://ec.europa.eu/eurostat/statistics-explained/index.php?title=Renewable_energy_statistics#Share_of_renewable_energy_more_than_doubled_between_2004_and_2019.

Fan, L. and Jin, Y. (1990). Ice survey in liao dong bay and ice force measurement on jz20-2-1 platform.

Frederking, R. M. and Timco, G. W. (1986). Field measurements of the shear strength of columnar-grained sea ice. National Research Council Canada, Institute for Research in Construction.

Gaertner, E., Rinker, J., Sethuraman, L., Zahle, F., Anderson, B., Barter, G. E., Abbas, N. J., Meng, F., Bortolotti, P., Skrzypinski, W., Scott, G. N., Feil, R., Bredmose, H., Dykes, K., Shields, M., Allen, C., and Viselli, A. (2020). IEA Wind TCP Task 37: Definition of the IEA 15-Megawatt Offshore Reference Wind Turbine.

Global Wind Energy Council (2009). Global Wind Report 2008. Retrieved from https://gwec.net/wp-content/uploads/2012/06/Global-Wind-2008-Report.pdf.

Global Wind Energy Council (2020). Global Offshore Wind Report 2020. Brussels. Retrieved from https://gwec.net/global-offshore-wind-report-2020/.

Global Wind Energy Council (2021). Global Wind Turbine Supplier Ranking for 2020. Brussels. Retrieved from https://gwec.net/gwec-releases-global-wind-turbine-supplier-ranking-for-2020/.

Gürtner, A. and Berger, J. (2006). Results from model testing of ice protection piles in shallow water. In International Conference on Offshore Mechanics and Arctic Engineering, volume 47470, pages 693–698.

Hendrikse, H. (2017). Ice-induced vibrations of vertically sided offshore structures. PhD thesis. Delft University of Technology.

Hendrikse, H. and Nord, T. S. (2019). Dynamic response of an offshore structure interacting with an ice floe failing in crushing. Marine Structures, 65:271–290.

Hendrikse, H., Ziemer, G., and Owen, C. (2018). Experimental validation of a model for prediction of dynamic ice-structure interaction. Cold Regions Science and Technology, 151:345–358.

Hoving, J., Vermeulen, R., Mesu, A., and Cammaert, A. (2013). Experiment-based relations between level ice loads and managed ice loads on an artic jack-up structure. In Proceedings of the 22nd International Conference on Port and Ocean Engineering under Arctic Conditions POAC, Espoo (Finland), 9-13 June, 2013. Citeseer.

Huang, Y., Ma, J., and Tian, Y. (2013a). Model tests of four-legged jacket platforms in ice: Part 1. model tests and results. Cold regions science and technology, 95:74–85.

Huang, Y., Yu, M., and Tian, Y. (2013b). Model tests of four-legged jacket platforms in ice: Part 2. analyses and discussions. Cold regions science and technology, 95:86–101.

ISO (2019). Petroleum and natural gas industries — Arctic offshore structures (ISO 19906:2019). Retrieved from https://www.iso.org/standard/65477.html.

Johnston, M., Timco, G., Frederking, R., and Jochnmann, P. (2000). Simultaneity of measured ice load on two legs of a multi-leg platform. In Proceedings of the 19 th International Conference on Offshore Mechanics and Arctic Engineering, OMAE'00.

Jonkman, J., Butterfield, S., Musial, W., and Scott, G. (2009). Definition of a 5-mw reference wind turbine for offshore system development. Technical report, National Renewable Energy Lab.(NREL), Golden, CO (United States).

Karulin, E. and Karulina, M. (2014). Peculiarities of multi-legged platform operation in ice condition. In ASME 2014 33rd International Conference on Ocean, Offshore and Arctic Engineering. American Society of Mechanical Engineers Digital Collection.

Kato, K., Adachi, M., Kishimoto, H., Hayashiguchi, S., et al. (1994). Model experiments for ice forces on multi conical legged structures. In The Fourth International Offshore and Polar Engineering Conference. International Society of Offshore and Polar Engineers.

Lever, J., Gooch, G., Tuthill, A., and Clark, C. (1997). Low-cost ice-control structure. Journal of cold regions Engineering, 11(3):198–220.

Liferov, P. (2005). First-year ice ridge scour and some aspects of ice rubble behaviour.

Løset, S., Shkhinek, K. N., Gudmestad, O. T., and Høyland, K. V. (2006). Actions from ice on arctic offshore and coastal structures. LAN St. Petersburg, Russia.

Maatanen, M., Loset, S., Metrikine, A., Evers, K., Hendrikse, H., Lonoy, C., Metrikin, I., Nord, T., and Sukhorukov, S. (2012). Novel ice induced vibration testing in a large-scale facility: Deciphering ice induced vibrations, part 1. In Proceedings of 21st IAHR international symposium on ice: Ice research for a sustainable enviroment, Dalian, China, 11–15 June 2012. Dalian University of Technology Press.

Markard, J. and Petersen, R. (2009). The offshore trend: Structural changes in the wind power sector. Energy Policy, 37(9):3545–3556.

Martin, S. and Kauffman, P. (1981). A field and laboratory study of wave damping by grease ice. Journal of Glaciology, 27(96):283–313.

Nawata, T., Kawasaki, T., Yano, S., and Ishikawa, S. (1986). Model tests of jacket structure in ice tank. In International offshore mechanics and arctic engineering. Symposium. 5, pages 436–443.

Oest, J., Sørensen, R., Overgaard, L. C. T., and Lund, E. (2017). Structural optimization with fatigue and ultimate limit constraints of jacket structures for large offshore wind turbines. Structural and Multidisciplinary Optimization, 55(3):779–793.

Oh, K.-Y., Nam, W., Ryu, M. S., Kim, J.-Y., and Epureanu, B. I. (2018). A review of foundations of offshore wind energy convertors: Current status and future perspectives. Renewable and Sustainable Energy Reviews, 88:16–36.

Owen, C. (2017). Ice-induced vibrations of vertically sided model structures: Comparison of structures with circular and rectangular cross-section subjected to the frequency lock-in regime.

Owen, C. C. and Hendrikse, H. (2019). A study of the transition ice speed from intermittent crushing to frequency lock-in vibrations based on model-scale experiments. In Proceedings of the 25th International Conference on Port and Ocean Engineering under Arctic Conditions. Delft. Retrieved June, volume 1, page 2020.

Paige, R. A. and Lee, C. W. (1967). Preliminary studies on sea ice in mcmurdo sound, antarctica, during "deep freeze 65". Journal of Glaciology, 6(46):515–528.

Palmer, A., Wei, B., Hien, P. L., and Thow, Y. K. (2015). Ice jamming between the legs of multi-leg platform. In Proceedings of the International Conference on Port and Ocean Engineering Under Arctic Conditions.

Petrich, C. and Eicken, H. (2010). Growth, structure and properties of sea ice. Sea ice, 2:23–77.

Politko, V. and Kantardgi, I. (2017). Level ice interactions with multi-legged offshore structures. - , (6):43–52.

Polojärvi, A. and Tuhkuri, J. (2009). 3d discrete numerical modelling of ridge keel punch through tests. Cold Regions Science and Technology, 56(1):18–29.

Polojärvi, A. and Tuhkuri, J. (2013). On modeling cohesive ridge keel punch through tests with a combined finite-discrete element method. Cold regions science and technology, 85:191–205.

Popko, W., Vorpahl, F., Zuga, A., Kohlmeier, M., Jonkman, J., Robertson, A., Larsen, T. J., Yde, A., Sætertrø, K., Okstad, K. M., et al. (2012). Offshore code comparison collaboration continuation (oc4), phase 1-results of coupled simulations of an offshore wind turbine with jacket support structure. In The twenty-second international offshore and polar engineering conference. OnePetro.

Roelfsema, M., van Soest, H. L., Harmsen, M., van Vuuren, D. P., Bertram, C., den Elzen, M., Höhne, N., Iacobuta, G., Krey, V., Kriegler, E., et al. (2020). Taking stock of national climate policies to evaluate implementation of the paris agreement. Nature Communications, 11(1):1–12.

Rogelj, J., Den Elzen, M., Höhne, N., Fransen, T., Fekete, H., Winkler, H., Schaeffer, R., Sha, F., Riahi, K., and Meinshausen, M. (2016). Paris agreement climate proposals need a boost to keep warming well below 2 c. Nature, 534(7609):631–639.

Sánchez, S., López-Gutiérrez, J.-S., Negro, V., and Esteban, M. D. (2019). Foundations in offshore wind farms: Evolution, characteristics and range of use. analysis of main dimensional parameters in monopile foundations. Journal of Marine Science and Engineering, 7(12):441.

Sanderson, T. J. (1988). Ice mechanics and risks to offshore structures.

Schulson, E. M. (1997). The brittle failure of ice under compression. The Journal of Physical Chemistry B, 101(32):6254–6258.

Schulson, E. M. and Duval, P. (2009). Creep and fracture of ice. Cambridge university press.

Serré, N. (2011a). Mechanical properties of model ice ridge keels. Cold regions science and technology, 67(3):89–106.

Serré, N. (2011b). Numerical modelling of ice ridge keel action on subsea structures. Cold regions science and technology, 67(3):107–119.

Shkhinek, K. N., Jilenkov, A. G., Blanchet, D., and Thomas, G. A. (2009). Ice loads on a four leg structure. In Proceedings of the International Conference on Port and Ocean Engineering Under Arctic Conditions, number POAC09-43.

Sinha, N. K. (1983). Creep model of ice for monotonically increasing stress. Cold Regions Science and Technology, 8(1):25–33.

Takeuchi, T., Saeki, H., Yamashita, T., et al. (1993). Total ice forces on multi-legged offshore structures. In The Third International Offshore and Polar Engineering Conference. International Society of Offshore and Polar Engineers.

Timco, G. (1986). Ice forces on multi-legged structures. In Proceedings of the IAHR Ice Symposium, Iowa City, Iowa, USA, volume 2, pages 321–337.

Timco, G. (1991). Laboratory observations of macroscopic failure modes in freshwater ice. In Cold Regions Engineering, pages 605–614. ASCE.

Timco, G. and Frederking, R. (1990). Compressive strength of sea ice sheets. Cold Regions Science and Technology, 17(3):227–240.

Timco, G. and O'Brien, S. (1994). Flexural strength equation for sea ice. Cold Regions Science and Technology, 22(3):285–298.

Timco, G. and Pratte, B. (1985). The force of a moving ice cover on a pair of vertical piles. In Proceedings Canadian Coastal Conference, St. John's, Newfoundland, Canada, pages 349–362.

Timco, G. and Weeks, W. (2010). A review of the engineering properties of sea ice. Cold regions science and technology, 60(2):107–129.

Timco, G. W. and Frederking, R. M. (1986). Confined compression tests: outlining the failure envelope of columnar sea ice. Cold Regions Science and Technology, 12(1):13–28.

Tuthill, A. M. and Lever, J. H. (2006). Design of breakup ice control structures. Technical report, ENGINEERING RESEARCH AND DEVELOPMENT CENTER HANOVER NH COLD REGIONS RESEARCH ....

UNFCCC (2015). Adoption of the Paris Agreement. United Nations Report No. FCCC/CP/2015/10/Add.1. Retrieved from `https://undocs.org/en/FCCC/CP/2015/10/Add.1`.

United Nations Environmental Programme (2020). Emissions Gap Report 2020. Nairobi. Retrieved from `https://www.unep.org/emissions-gap-report-2020`.

U.S. Department of Energy (2008). Historic Wind Development in New England. Retrieved from `https://web.archive.org/web/20100527173013/http://www.windpoweringamerica.gov/ne_history_windfarms.asp`.

van den Berg, M. (2013). Ice-induced virbrations of jack-up structures.

van den Berg, M., Lubbad, R., and Løset, S. (2018). An implicit time-stepping scheme and an improved contact model for ice-structure interaction simulations. Cold Regions Science and Technology, 155:193–213.

Vemula, N. K., DeVries, W., Fischer, T., Cordle, A., and Schmidt, B. (2010). Design solution for the upwind reference offshore support structure. Upwind deliverable D, 4. (to be published).

Vorpahl, F., Popko, W., and Kaufer, D. (2011). Description of a basic model of the" upwind reference jacket" for code comparison in the oc4 project under iea wind annex xxx. Fraunhofer Institute for Wind Energy and Energy System Technology (IWES), Germany, 450.

Weeks, W. F. and Ackley, S. F. (1986). The growth, structure, and properties of sea ice. In The geophysics of sea ice, pages 9–164. Springer.

Wessels, E. and Jochmann, P. (1990). Determination of ice forces on jacket jz 20-2-1 by model and full scale tests.

Willems, T. (2016). Coupled modeling of dynamic ice-structure interaction on offshore wind turbines. Delft University of Technology.

WindEurope (2017). The European offshore wind industry - key trends and statistics 2017. Retrieved from https://windeurope.org/intelligence-platform/product/the-european-offshore-wind-industry-key-trends-and-statistics-2017/.

WindEurope (2018). Offshore wind in Europe - key trends and statistics 2018. Retrieved from https://windeurope.org/intelligence-platform/product/offshore-wind-in-europe-key-trends-and-statistics-2018/.

WindEurope (2019a). Boosting offshore wind energy in the Baltic Sea. Retrieved from https://windeurope.org/wp-content/uploads/files/about-wind/reports/WindEurope-Boosting-offshore-wind.pdf.

WindEurope (2019b). History of Europe's wind industry. Retrieved from https://windeurope.org/about-wind/history/.

WindEurope (2020a). Offshore Wind in Europe. Key trends and statistics 2020. Retrieved from https://windeurope.org/data-and-analysis/product/offshore-wind-in-europe-key-trends-and-statistics-2020/.

WindEurope (2020b). Wind energy in Europe. 2020 Statistics and the outlook for 2021-2025. Retrieved from https://windeurope.org/data-and-analysis/product/wind-energy-in-europe-in-2020-trends-and-statistics/.

World Wind Energy Association (2020). Global Wind Statistics. Retrieved from https://library.wwindea.org/global-statistics/.

Xu, N., Yue, Q., and Kärnä, T. (2009). The developing process and risk analysis of ice jams based on field test. In Proceedings of the International Conference on Port and Ocean Engineering Under Arctic Conditions, number POAC09-49.